**Inter and Intramolecular Aryl-Nitroso Copper-Mediated Redox Reactions**

A Thesis

In the Department

Of

Chemistry and Biochemistry

Presented in Partial Fulfillment of the Requirements

For the Degree of

Master of Science (Chemistry) at

Concordia University

Montreal, Quebec, Canada

November 2019

CONCORDIA UNIVERSITY
School of Graduate Studies

This is to certify that the thesis prepared

By: Farshid Effaty

Entitled: Inter and Intramolecular Aryl-Nitroso Copper-Mediated Redox Reactions

and submitted in partial fulfillment of the requirements for the degree of

Master of Science in Chemistry

complies with the regulations of the University and meets the accepted standards with respect to originality and quality.

Signed by the final examining committee:

Dr. Gilles Peslherbe Chair

Dr. Pat Forgione Examiner

Dr. Louis Cuccia Examiner

Dr. Xavier Ottenwaelder Supervisor

Approved by: _____
Dr. Yves Gélinas, Graduate Program Director

_____
Dr. André Roy, Dean, Faculty of Arts and Science

Date: November 28th, 2019

# Abstract

**Inter and Intramolecular Aryl-Nitroso Copper-Mediated Redox Reactions**

**Farshid Effaty, M.Sc.**

The redox conversions of hydroxylamine ($NH_2OH$) are biologically relevant because this molecule serves as a nitric oxide donor in mammals under certain conditions. The analogous arylhydroxylamine compounds (ArNHOH, where Ar is an aryl group) display similar chemistry, with the advantage of fewer side-reactions. Thus, there has recently been increased interest into investigations of the reactivity of arylhydroxylamines with metal complexes as mimics of the biologically relevant reactions of $NH_2OH$ with copper or iron. Oxidation of arylhydroxylamines yields nitrosoarenes (ArNO), which are structurally and electronically versatile redox-active molecules. Their corresponding metal complexes are stable mimics of $O_2$ and HNO complexes transiently found in nature and catalytic cycles. This stability allows for a systematic survey of the structure and redox state of ArNO metal complexes. The metal-mediated transformations between ArNHOH, ArNO and other relevant nitrogen-based groups, however, are not well understood. Herein, in two different reports, we address the reactivity of ArNHOH and ArNO groups with copper complexes.

In the first study, a series of complexes is prepared by self-assembly of copper(I) precursors and arylnitroso species. The nature of the copper(I) supporting ligand (bi-, tri- or tetradentate, as well as secondary vs. tertiary amine donors) and the electronic nature of the arylnitroso species (electron-donating or withdrawing substituents) are varied. The stoichiometry of the reaction, the topology, and the electronic properties of the adducts are characterized by UV-Vis spectroscopy, single crystal X-ray diffraction, and DFT methods. The more electron-rich ligands and the more electron-poor arylnitroso species lead to an inner-sphere electron transfer and formation of copper(II)-(arylnitrosyl radical) complexes bearing a linkage topology that depends on the denticity of the supporting ligand. These results provide a canvas by which to predict the products of similar self-assembled redox reactions.

In the second study, the synthesis of an unprecedented copper(I)-arylhydroxylamine complex is reported. The reactivity of the arylhydroxylamine is arrested by the presence of an intramolecular hydrogen bond that stabilizes the weakly bound hydroxylamine. Upon two-electron oxidation, a copper(II)-(arylnitrosyl radical) complex is formed, which crystallizes as a copper(I) species with an uncoordinated arylnitroso function. This validates that such ligands may enable ligand redox chemistry and hemilability in copper complexes. Such tethered arylnitroso complexes present new opportunities for two-electron chemistry in earth-abundant metal catalysis.

In a nutshell, this thesis highlights unique electron-transfer events and redox conversions about the N-O bond in copper complexes. The main finding is the characterization of an intermediate redox state in-between ArNHOH and ArNO, namely the arylnitrosyl radical anion, $ArNO^-$, which is stable only when coordinated.

# Acknowledgments

First and foremost, I would like to thank my research supervisor, Dr. Xavier Ottenwaelder, whose insightful use of Da-Man and You're Fired points has been my life for these past years.

I also would like to thank my committee members, Dr. Louis Cuccia and Dr. Pat Forgione for their insightful suggestions throughout my committee advisory meetings and on top of that because they have to read this hefty document and try to come up with good questions.

I thank all the XoRG members, past and present, who helped me survive the horror of graduate student life in the Lab. Significant portions of this research were only made possible because of collaborations: Joseph who worked as an undergrad on part of this project and later we continued to collaborate on with his supervisor Dr. Kennepohl (UBC), whom also provide great insight and contributions. Dr. Mohammad Askari for fruitful discussions and guidance during my research. Léon Escomel who was another undergrad helping me on some ligand synthesis optimizations.

Also, I would like to thank Alain Tessier for his kind help with Mass Spectrometry experiments.

I would also like to thank my cheerful friends and Concordia Chemistry Department staff who made my life as a grad student much more enjoyable. Many thanks to Jiang Tian (Peter) Liu and Jean-Louis Do who were always available for helping me. I am also indebted to all my friends who made me feel I have a second family here in Montreal: Sepehr and Zahra, as well as Mehrdad and Hadi in the US.

Last but not least, I want to thank my family for all their emotional supports, My mom Maryam, My dad Samad and my beautiful little sister Kimia. This would not happen without them. This thesis is dedicated to them.

# Contribution from Authors

## Chapter 2: Ligand and Electronic Effects on Copper-Arylnitroso Self-Assembly

| | |
|---|---|
| Farshid Effaty | Synthesis of complexes, data analysis, crystal structure and spectroscopic characterization, writing the SI, manuscript preparation |
| Joseph Zsombor-Pindera | Computational studies |
| Anastasia Kazakova | Synthesis and crystallization of one compound |
| Brigitte Girard | Synthesis and crystallization of one compound |
| Mohammad S. Askari | Undergraduate supervision, crystallography for a few compounds |
| Xavier Ottenwaelder | Research supervisor, crystallography, writing and editing |

## Chapter 3: A Stable Copper-Arylhydroxylamine Complex and its Conversion to a Hemilabile Arylnitroso

| | |
|---|---|
| Farshid Effaty | Synthesis of ligand and complexes, data analysis, solid-state and solution reactivity and characterization, mass spectrometry, crystal structure of compound **2**, writing and editing the SI and manuscript |
| Joseph Zsombor-Pindera | Synthesis of complexes, XAS experiments and analysis, computational studies, crystallization of compounds **1**, **2** and **4**, initial reactivity studies, VT-NMR, writing and editing the SI and manuscript |
| Leon Escomel | Initial ligand synthesis and mass spectrometry experiments |
| Pierre Kennepohl | Research supervisor, XAS data analysis, editing |
| Xavier Ottenwaelder | Research supervisor, project design, writing and editing |

# Table of Contents

## List of Figures

## List of Schemes

## List of Tables

## List of Abbreviations

| | |
|---|---|
| BDE | Bond Dissociation Energy |
| CHN | Carbon Hydrogen Nitrogen (elemental analysis) |
| COSY | Correlation Spectroscopy |
| $\Delta_o$ | Octahedral field splitting parameter |
| DFT | Density Functional Theory |
| ε | Molar Absorptivity |
| EDTA | Ethylenediaminetetraacetic acid |
| EPR | Electron Paramagnetic Resonance |
| ESI | Electrospray Ionization |
| ET | Electron Transfer |
| η | Hapticity |
| Equiv. | Equivalents |
| g | g-factor (EPR) |
| HAT | Hydrogen-atom transfer |
| hν | Photon energy |
| HS | High Spin |
| IR/NIR | Infrared/Near Infrared |
| $k_{obs}$ | Pseudo-ordered rate constant |
| k | Rate constant |
| K | Equilibrium constant |
| L | Ligand |
| LMCT | Ligand to metal charge transfer |
| LS | Low Spin |
| $m/z$ | Mass-to-charge ratio |
| MLCT | Metal-to-ligand charge-transfer |
| MS | Mass spectrometry |
| $\mu_B$ | Bohr magneton |
| NMR | Nuclear Magnetic Resonance |
| NOESY | Nuclear Overhauser effect spectroscopy |
| OAT | Oxygen-Atom Transfer |
| ORTEP | Oak Ridge Thermal Ellipsoid Plot |
| $r_{vdW}$ | Van der Waals radius |
| SC-XRD | Single-Crystal X-Ray Diffraction |
| TBP | Trigonal Bipyramidal |
| TLC | Thin-layer chromatography |
| UV-Vis | Ultraviolet/Visible |
| XAS | X-Ray Absorption Spectroscopy |

# Chapter 1: Introduction

## 1.1 Nitrosoarenes and Derivatives

Even though reactive nitrogen-containing functional groups such as hydroxylamines (R–NHOH, $NH_2OH$), nitroxyl (HNO), nitroxide ($NO^-$), nitric oxide (NO) and nitroso compounds (R–NO) are involved in physiological responses (neurotransmission, blood pressure regulation, immune response),[1] their redox conversion chemistry is not yet fully characterized. Due to the versatile redox capability of such species, studying their chemical behaviour and transformations in the vicinity of bio-active metal centers such as copper and iron is a fascinating area of research. In this thesis, we concentrate our efforts on studying the reactivity of nitrosoarenes (ArNO) and hydroxylamines (Ar-NHOH) (Scheme 1-1).

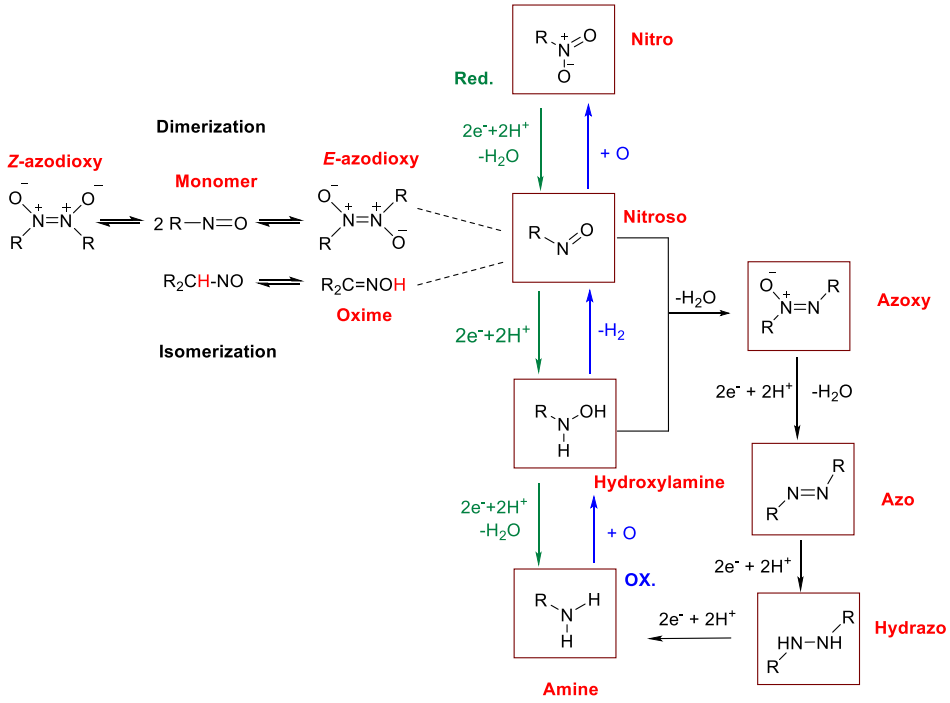


Scheme 1-1: Redox, dimerization and tautomerism profiles of non-coordinated organic nitrogen-containing functional groups.

Compounds containing the nitroso functional group (–N=O) are categorized as four different groups based on the adjacent atom to nitrogen: C-nitroso (R–N=O, R = alkyl, aryl), N-nitroso ($R_2N$–N=O), O–nitroso (RO–N=O), and S-nitroso (RS–N=O). Regarding the research presented in this thesis, only aromatic-carbon bonded nitrosos (ArNO) will be discussed. In the solid-state, depending on the nature of the substituent on the aromatic ring, nitrosoarenes exist as monomers or diazoxy dimers (Scheme

1-2). In the arylnitroso series, the presence of electron-donating group on the aromatic ring favours the formation of the monomeric arylnitroso owing to the stabilization caused by the resonance structure (Scheme 1-2). On the other hand, electron-withdrawing group on the aromatic ring favours the formation of diazoxy dimer. The dimers exist in either *cis*- or *trans*- configurations that depend on the substituents as well. In solution, however, the monomeric form is predominant.

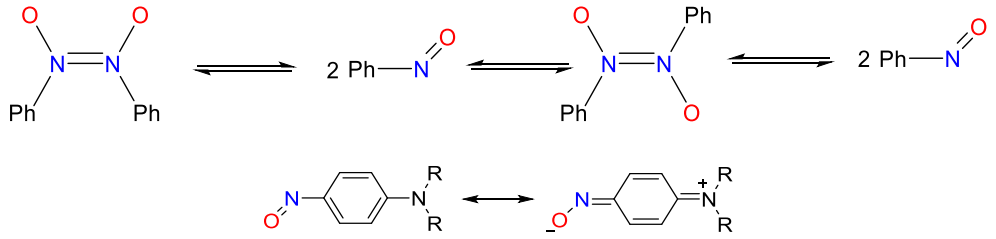


Scheme 1-2: Dimerization nitrosoarenes and resonance contribution to stabilizing monomeric arylnitroso.

The N=O bond length in structurally characterized nitrosoarene monomers reported in the range 1.13-1.29 Å and for the dimers 1.25-1.28 Å.[2] The UV-vis profile for nitrosoarenes typically shows two absorption bands corresponding to the n→π* transition around 270 nm (strong) and π → π* transition at 700 nm (weak).[2] Infrared (IR) spectroscopy is also often employed for characterization of ArNO, especially to probe the N=O stretch and hence the bond order. However, due to the fact the N=O stretch absorption band appears in the fingerprint region (1200-1600 $cm^{-1}$) of IR spectra, precise assignment requires isotope labeling on the nitroso function, mainly with $^{15}N$, to find out the corresponding band in the spectrum based on the shifts.[2] For monomeric nitrosoarenes, the N=O bond shows one band in the range 1488-1513 $cm^{-1,}$ while in the *trans*-dimers the value is shifted to 1253-1299 $cm^{-1}$; the *cis*-dimers display two bands in the range of 1389-1397 $cm^{-1}$ and ca. 1409 $cm^{-1}$.

Nitrosoarenes (ArNO) are aromatic compounds with an –N=O functional group that is isoelectronic to dioxygen. Recent reports have highlighted the diverse redox states of ArNO ligands in metal complexes.[3–10] In particular, the one-electron reduction series of nitrosoarene compounds ArNO (arylnitroso) to $ArNO^{\bullet-}$ (arylnitrosyl radical) to $ArNO^{2-}$ (doubly deprotonated hydroxylamine) is isovalent to the all important $O_2$, $O_2^{\bullet-}$, $O_2^{2-}$ series ($O_2$, superoxide, and peroxide). Therefore, understanding metal/ArNO interactions will provide insight into reactions involving reactive oxygen species (ROS).

In addition, the interaction of nitrosoarenes with metal complexes[2] is relevant to biological processes[11–14] and catalytic C–N bond formation reactions.[15–17] Thus, beside acting as $O_2$ analogues, ArNO species are important to study, especially how to control their inherent reactivity via interaction with metal complexes.

## 1.2 Interactions of Nitrosoarenes with Metal Centers

Like oxygen, organic nitroso ligands are known to have a highly diverse variety of binding modes, as well as an interesting range of electronic structures. Due to these unusual structural, redox, and electronic properties, organic nitrosos such as ArNO might have the potential to confer enhanced electronic and oxidative malleability on metal centers. Upon coordination with a metal ion M, this property is known as redox noninnocence, and it is desirable because it may lead to new reactivity through ligand cooperative redox catalysis.

The interaction of nitrosoarenes with metal centers has drawn much attention due to its relevance to biological pathways[11–14,18–20] and catalytic C–N bond formation processes.[15–17,21,22] Chemists now have a good understanding of the geometric structure of transition metal-arylnitroso complexes.[2,23] Also, ArNO species are redox non-innocent ligands,[5,6,24] which makes their interaction with redox-active metal ions portend an even larger landscape of electronic structures and reactivity types.

Since ArNO species are isovalent with $O_2$, reduction of ArNO by a transition metal is akin to the reduction of $O_2$ to the superoxide ion ($O_2^{\bullet-}$, 1e reduction) or the peroxide ion ($O_2^{2-}$, 2e reduction). Therefore, metal/ArNO adducts can be seen as surrogates for metal/$O_2$ adducts. In particular, and with relevance to the present thesis, the activation of $O_2$ by Cu(I) centers is paramount in the biological world. This process fuels enzymes such as dopamine-*β*-hydroxylase, tyrosinase, and particulate methane monooxygenase, to name but a few.[25,26] This has inspired numerous biomimetic studies in which an electron-rich Cu(I) species are reacted with $O_2$.[27–29] Without protection of the protein backbone, however, the ensuing Cu/$O_2$ complexes are formed by self-assembly and are usually too oxidative to be stable above –60°C. By contrast, Cu/ArNO adducts have been shown to have very similar geometric and electronic structures to those in Cu/$O_2$ adducts but were advantageously characterized at ambient temperature.[4,6–8]

Owing to the asymmetric structure of ArNO in comparison with $O_2$, the structural variety of metal/nitrosoarene complexes exceeds that of metal/$O_2$ compounds. Some of the main bonding modes of ArNO to metal ions are shown in Scheme 1-3,[2,23] the most common one being through the nitrogen atom (*κ*N). The other bonding modes are thought to be more prevalent when the ArNO moiety is reduced to the mono- or dianion. The NO bond length in metal/ArNO complexes depends on the bonding mode, the nature and oxidation state of the metal and the supporting ligands. (Scheme 1-3) However, bond-length analysis is not sufficient to characterize the degree of reduction of the ArNO moiety, as was already shown with metal/$O_2$ adducts.[9]

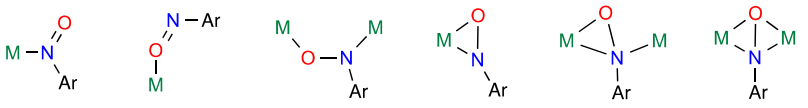


Scheme 1-3: Some bonding modes in metal/arylnitroso complexes, with typical NO bond lengths. * indicates disordered structures where the bond analysis may not be not relevant.

A few studies have scrutinized the electronic structure on metal/ArNO complexes, particularly the oxidation state of the ArNO moiety, utilizing techniques such as X-ray absorption spectroscopy or vibrational analysis with isotope labeling. Scheme 1-4 provides examples where the electronic structure of the complexes and the oxidation state of the ArNO moiety were well characterized. Below are the main conclusions of these studies.

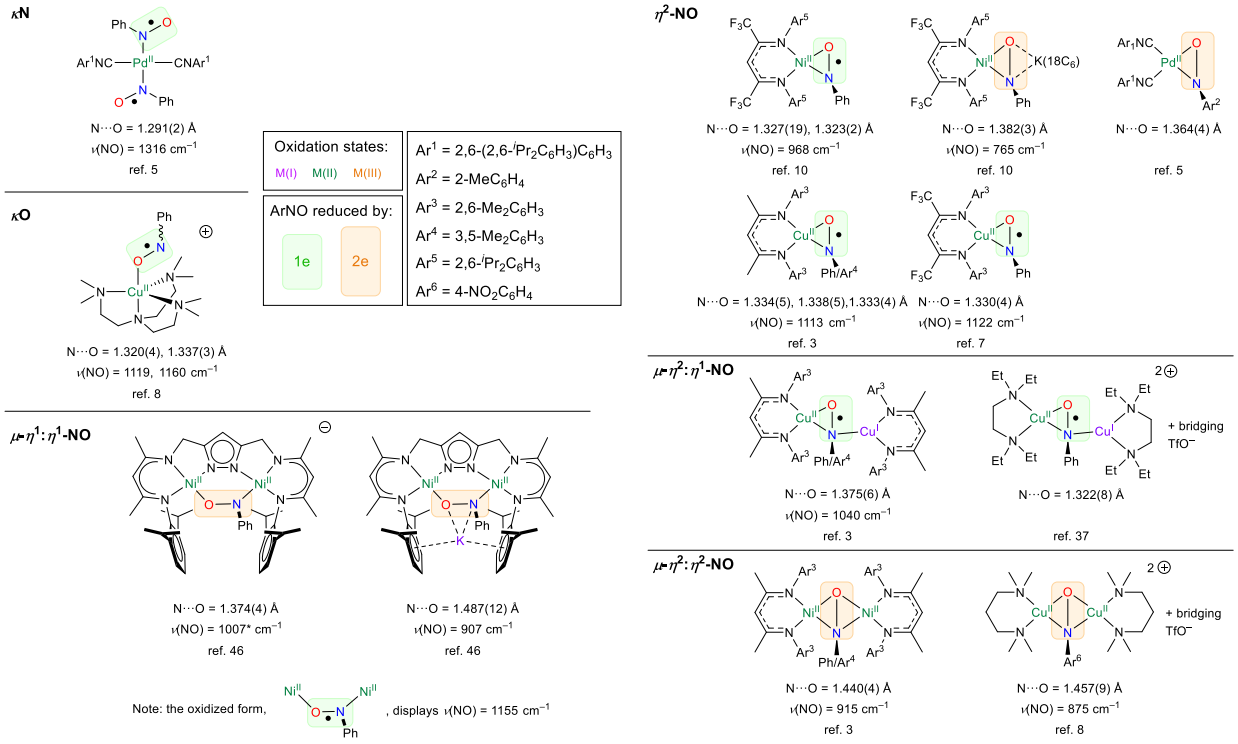


Scheme 1-4: Confirmed examples of group 10-11 complexes in which ArNO gets reduced by 1e or 2e upon reaction.

– In the majority of mononuclear *κ*N complexes of nitrosoarenes, the NO bond length, 1.209–1.31 Å shows little or no elongation compared with that in free nitrosoarenes (Scheme 1-5),[2,23] unless back

bonding from the metal becomes significant.[5] The radical character of the *κ*N-ArNO moiety and thus formally a 1.5 bond order has been confirmed or inferred in a few species (Scheme 1-4).[5,30,31]

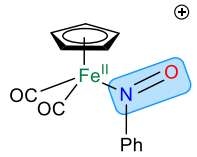


N···O = 1.226(1) Å
ref. 38

Scheme 1-5: Simple *κ*N coordination of arylnitroso to organometallic iron(II) center.

– In mononuclear *κ*O complexes, the NO bond length is reported in the range of 1.057–1.33 Å.[2,23] The unusually short bonds and the large variation is due to disordered X-ray structures frequently observed with O-bonded nitrosoarene complexes.[32–36] Thus, conclusive statements about the extent of back-donation and ArNO reduction cannot be made. By contrast, the well-ordered crystal structures of [(Me$_6$tren)Cu(*κ*O-PhNO)]X (X = TfO$^-$, SbF$_6^-$, Scheme 1-6) show significant NO bond elongation. The radical character of the PhNO moiety (to an arylnitrosyl radical anion) was confirmed by magnetic measurements, vibrational and computational studies.[6,37]

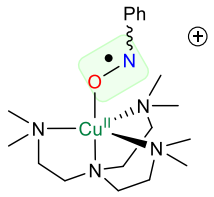


N···O = 1.320(4), 1.337(3) Å
$\nu$(NO) = 1119, 1160 cm$^{-1}$
ref. 6

Scheme 1-6: Mononuclear O-bonded copper arylnitroxyl radical.

– Dinuclear $\mu$-$\eta^1$:$\eta^1$ (end-on) complexes present varying degrees of ArNO reduction: by 0e (NO = 1.257-1.32),[38–43] 1e (1.33-1.35)[44] and 2e (1.37-1.49, Scheme 1-7).[45,46]

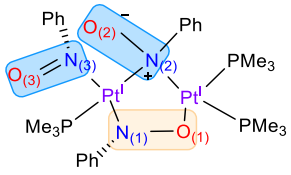


N$_{(1)}$···O$_{(1)}$ = 1.433(15) Å
N$_{(2)}$····O$_{(2)}$ = 1.428(27) Å
N$_{(3)}$····O$_{(3)}$ = 1.296(14) Å
ref. 45

Scheme 1-7: Dinuclear platinum complex with zero and two electron reduced nitroso ligand.

– The NO bond length in $\eta^2$-NO complexes, 1.323–1.432 Å[4,5,53,10,31,47–52] (Scheme 1-8), is significantly longer than in free nitrosoarenes. One-electron reduction of the ArNO moiety has been confirmed in Cu and Ni complexes (Scheme 1-4).[4,10] Further reduction of the Ni complex led to a doubly reduced $PhNO^{2-}$ moiety.[10] Two-electron reduction of the ArNO moiety was also confirmed in a square-planar Pd(II) species upon the reaction of a $Pd^0$ species with TolNO.[5]

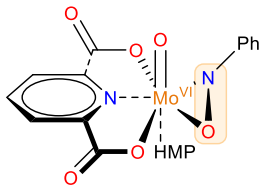


N....O = 1.416(7) Å
ref. 48

Scheme 1-8: $\eta^2$:$\eta^2$ Molybdenum complex with two electron reduction of nitroso ligand.

– Beside examples with other transition metals (NO bond lengths of 1.40–1.53 Å, Scheme 1-9),[31,54–59] dinuclear $\mu$-$\eta^2$:$\eta^1$ complexes have been found in the solid-state structures of Cu complexes with shorter NO bond lengths (1.322–1.375 Å).[4,9] Typically, the 1e-reduced $ArNO^{\bullet-}$ moiety binds $\eta^2$ to a Cu(II) center and $\eta^1$ to a Cu(I) center. These species are thought to be in equilibrium with the mononuclear form, [$Cu^{II}$($\eta^2$-$ArNO^{\bullet-}$)], in solution.

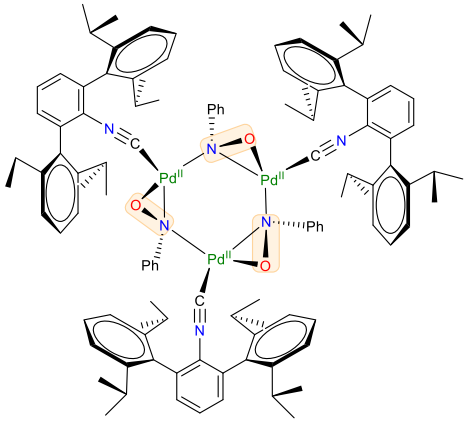


Avg. N···O = 1.414(3) Å
ref. 31

Scheme 1-9: Multinuclear $\mu$-$\eta^2$:$\eta^1$ complex in organometallic palladium cluster.

– Dinuclear $\mu$-$\eta^2$:$\eta^2$ complexes are quite rare and only few examples with Rh,[58] Zr,[60] Hf (Scheme 1-10),[60] Ni,[4] and Cu (Scheme 1-10)[8] are reported in the literature. With an NO bond length, 1.422–1.500 Å, in the range of single bonds, these complexes possess a doubly reduced $ArNO^{2-}$ moiety. In the

case of the Cu complex,[8] this 2e reduction was made possible by using a very electron-poor nitrosoarene bearing a *para* $NO_2$ substituent.

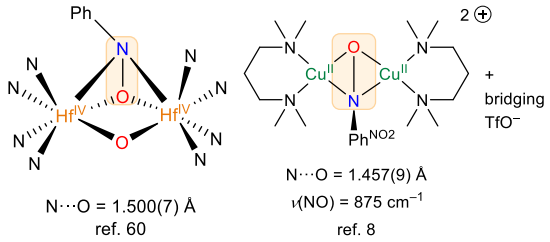


Scheme 1-10: Dinuclear $\mu$-$\eta^2$:$\eta^2$ complexes with hafnium and copper.

To summarize, 1e reduction of the ArNO moiety is usually indicated by NO bond length in the range 1.29–1.37 Å and NO stretching frequencies in the range 1000-1300 $cm^{-1}$ (Scheme 1-4). Reduction by 2e is revealed by NO bond lengths of 1.36–1.46 Å and NO stretching frequencies below 950 $cm^{-1}$. When no reduction occurs, the NO bonds are short (1.261(4) and 1.268(4) Å for free PhNO) and the NO stretching frequency is high (1506 $cm^{-1}$ for free PhNO), although these values can be modified significantly when back bonding is present.[5] Last, 4e reduction of PhNO, with complete NO bond cleavage, is possible with very electron-rich metal complexes such as β-diketiminate Co(I) species (Scheme 1-11).[3]

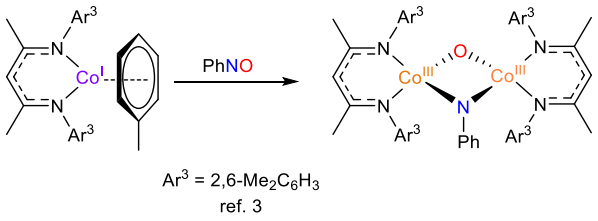


Scheme 1-11: Four electron reduction of nitroso function with β-diketiminate Co(I).

Noting that these examples comprise different supporting ligands and metal ions, our lab has recently carried out a systematic study of the degree of inner-sphere ArNO reduction by using a single Cu(I) precursor. In this study, adducts $\mathbf{3^R}$ (R = $NMe_2$, H, Cl, Br, $NO_2$) formed upon intermolecular reaction of *para*-substituted nitrosobenzenes $\mathbf{2^R}$ with the Cu(I) complex of *N,N,N',N'*-tetramethyl-1,3-propanediamine (TMPD), **1** (Scheme 1-12), for which analogous $Cu/O_2$ chemistry is known.[61–63]

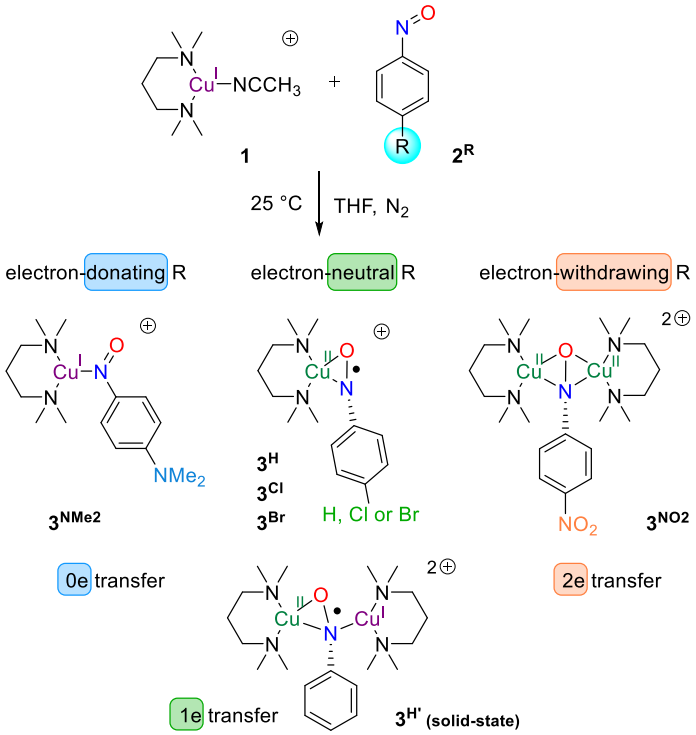


Scheme 1-12: Inner-sphere electron transfers in the TMPD-Cu-ArNO series.

## 1.3 Arylnitrosos in Organic C–O and C–N Bond Formations

In organic synthesis, nitrosoarenes are often used to transfer nitrogen-containing functional groups to organic substrates, an important transformation in pharmaceuticals and natural product synthesis. Examples are shown in Scheme 1-13, where nucleophiles such as enolates[64–66] and Grignard reagents[67,68] readily add to the -N=O functional group of the electrophilic nitrosoarene. Nitrosoarenes also participate in pericyclic reactions such as nitroso-Diels-Alder[64,65] and nitroso-ene[22] reactions. All these reactions can be employed to transfer nitrogen, oxygen or both into organic compounds.

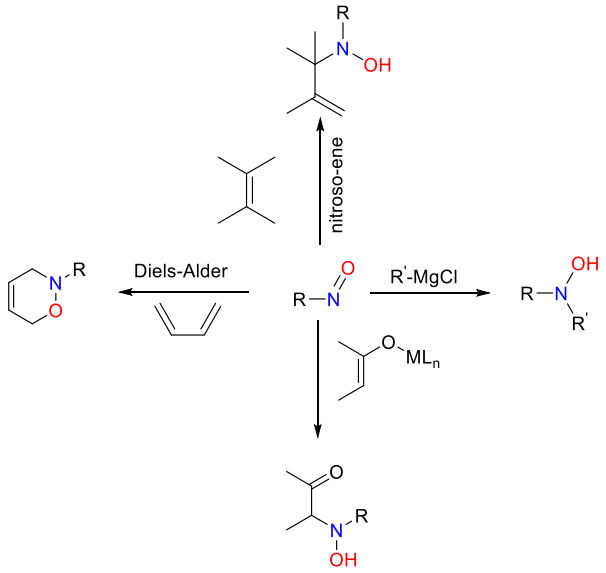


Scheme 1-13: Examples highlighting some reactions of nitroso compounds, adapted from [22].

Since the 1899 Ehrlich-Sachs condensation (Scheme 1-14 a),[69] methods have been developed for the functionalization of preformed or in situ-generated enolates and enamines with nitrosoarene at the α-carbon. The chemoselectivity between C–O or C–N bond formation can be tuned by careful choice of enolate, solvent, catalyst and additive (Scheme 1-14 b).[64] Beside α-functionalization of ketone derivatives, nitrosoarenes were used for the synthesis of nitrones from ketones in good yields (Scheme 1-14 c).[70] The nitroso-Diels-Alder reaction provides a convenient route for the incorporation of both nitrogen and oxygen atoms in organic substrates. However, the difficulty to remove the N-aromatic group makes this reaction less synthetically attractive. Instead, in situ-generated acylnitroso compounds and nitrosoalkanes have proven more useful in nitroso-Diels-Alder reactions.[64,65,71]

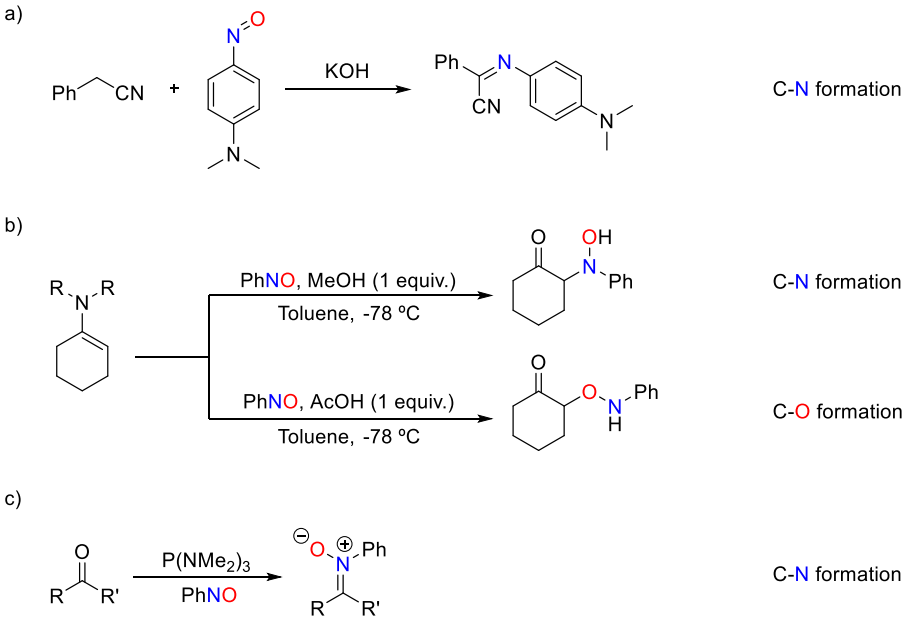


Scheme 1-14: Reaction of nitrosoarenes with enolates and ketones: a) the Ehrlich-Sachs reaction, b) C–N vs. C–O bond formation between enamines and nitrosoarenes, and c) Synthesis of nitrones from ketones and nitrosoarenes.

The nitroso-ene reaction (Scheme 1-13) is analogous to the standard "ene" reaction, whereby allylic positions react with nitrosoarenes to give the ene product.[22] However, the inherent reactivity of the nitrosoarene is one of the drawbacks of this reaction. Thus, nitrosoarenes react with difficulty with monosubstituted alkenes and nitrosoarene decomposition prevails.[22] The difficulty to remove the aromatic ring from arylamines also limits the utility of nitroso-ene reactions to cases where the aromatic ring is present in the final product, as in the recent example of the total synthesis of asmarine analogues (Scheme 1-15).[72] When the free amine is desired, acyl-nitroso compounds offer a better alternative since the amine can be liberated via hydrolysis. Mechanistically, concerted pericyclic pathway and stepwise mechanism with the intermediacy of amine oxides or diradicals were proposed.[73] In the case of a metal-catalyzed nitroso-ene reaction, metal-nitrosoarene complexes are invoked, which are described in the next section.

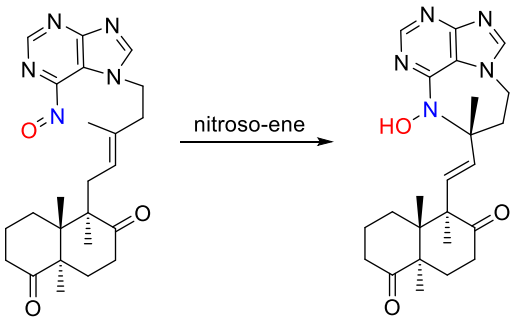


Scheme 1-15: Example of a nitroso-ene reaction in total synthesis.

## 1.4 Metal Arylnitrosos in Organic Transformations

Upon interaction with a metal center, nitrosoarenes can act as simple ligands with N-donation and backdonation into the NO π* system, but also can undergo reduction to the amine, oxygen-atom transfer, and nitrogen-group transfer. The latter is the most synthetically useful reaction and proceeds through metal/nitrosoarene complexes.[16,17,74–76] Of the reactions described in section 1.3, the nitroso-aldol and nitroso-Diels-Alder reactions are usually performed without metal catalysts unless direct amination at α-carbon[77] or an enantioselective version is required.[64,65] The metal-catalyzed nitroso-ene reaction has been studied in more detail. The initial stoichiometric report using a molybdenum arylnitroso complex[47] was later developed into a catalytic variant employing phenylhydroxylamine (Ph-NHOH) as the substrate.[74,75] These findings later developed into iron[76] and copper[16,17]-catalyzed allylic amination versions (Scheme 1-16).

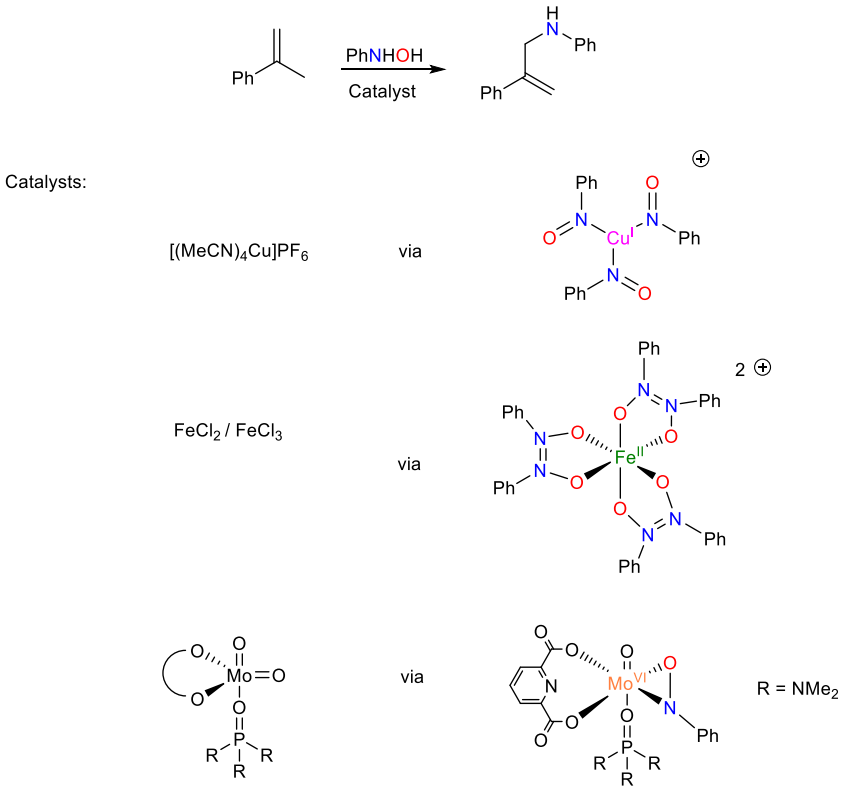


Scheme 1-16: Metal-catalyzed nitroso-ene reaction and the structure of suggested active catalyst.[16,17,74–76]

In addition to the above examples, the copper-mediated coupling of nitrosoarenes with arylboronic acids was reported (Scheme 1-17).[78] In this reaction, a $\eta^2$-NO copper(III) intermediate was speculated, which would undergo a reductive elimination mechanism.

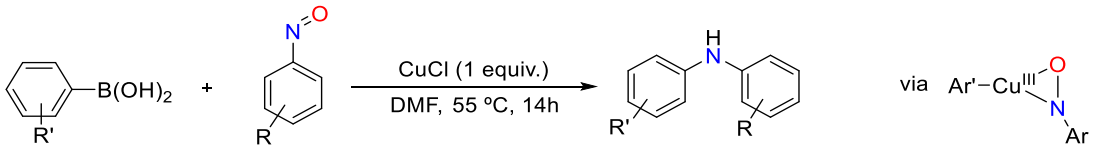


Scheme 1-17: Coupling of aromatic boronic acids with nitrosoarenes mediated by CuCl.[78]

In our group, we have recently established that stoichiometic *ortho*-amination of phenolates was possible from a $\mu$-$\eta^2$:$\eta^2$-NO complex, demonstrating the similar reactivity of $Cu/O_2$ and Cu/ArNO species (Scheme 1-18).[8]

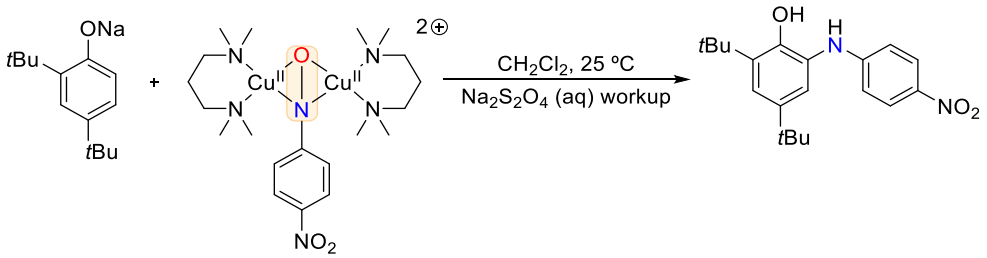


Scheme 1-18: *Ortho*-amination of phenolate by $Cu_2(\mu\text{-}\eta^2\text{:}\eta^2\text{-ArNO})$ complex.[8]

## 1.5 Objectives and Approach

In order to better understand the interaction of nitrosoarenes with copper centers we have delineated two different objectives with different designs:

- Objective 1: performing intermolecular Cu/ArNO reactions to understand factors governing binding modes and redox state.
- Objective 2: studying intramolecular Cu/ArNO reactions using a NHOH-bearing ligand as precursor.

In the first study, we carry out intermolecular reactions between a copper(I) precursor complexes and nitrosoarene derivatives. We employed four copper(I) precursor complexes with four different aliphatic amine supporting ligands from bidentate secondary amine to tetradentate tertiary aliphatic amines. Four nitrosoarenes were chosen for their different electronic properties by varying the *para* position with electron-donating, neutral or withdrawing substituents. The reactions yield oxygen-sensitive complexes that were isolated as solid forms (as powders or in single-crystal form) or prepared in-situ in solution for study by means of UV-Vis titrations.

In the second study, we synthesized a new arylhydroxylamine-containing tridentate chelating ligand, $L^{NHOH}$. The reaction of this $L^{NHOH}$ ligand with copper(I) chloride yielded a very interesting and unique $L^{NHOH}CuCl$ that was crystallized and isolated in solid form. This complex is unique due to its intact hydroxylamine ligand, which goes against the common belief that hydroxylamines readiliy disproportionate in the present of copper ions. Reaction of $L^{NHOH}CuCl$ with organic oxidants yielding a hemilabile arylnitroso complex, $L^{NO}CuCl$. The structural and electronic properties of these complexes were thoroughly investigated with variety of techniques including X-ray crystallography, X-ray Absorption Spectroscopy, EPR, UV-Vis, Mass Spectroscopy, and further supported by DFT calculations.

## 1.6 Organization of the Thesis

As seen above, Chapter 1 of this thesis introduced the arylhydroxylamine & arylnitroso chemistry in the vicinity of metal complexes. This chapter also provided a more detailed background than can be found in the subsequent manuscripts.

Chapter 2 describes the systematic study of supporting-ligand and electronic effects on self-assembly of copper(I) precursors with arylnitrosos. The author performed all the experimental work. At the time of thesis submission, the manuscript was published in *New Journal of Chemistry* as a full article.[37]

Chapter 3 presents collaborative work with Prof. Kennepohl (UBC) on a stable copper/arylhydroxylamine complex and its transformation to a hemilabile arylnitroso ligand. In this work, we suggest an unusual stabilization of the hydroxylamine moiety via intramolecular hydrogen bonding to the chloride ligand. All the DFT and XAS work and data analysis was performed by our collaborators and the author has done majority of other synthetic, experimental and data analysis work. By the time of thesis submission, this manuscript was submitted in communication format.

Chapter 4 presents some concluding remarks encompassing the research presented in the previous sections and suggestions for future research work.

# Chapter 2: Ligand and Electronic Effect on Copper(I)-Arylnitroso Self-Assembly

Farshid Effaty,[a] Joseph Zsombor-Pindera,[a] Anastasia Kazakova,[a] Brigitte Girard,[a] Mohammad S. Askari[a], Xavier Ottenwaelder*[a]

[a] Department of Chemistry and Biochemistry, Concordia University, 7141 Sherbrooke W, Montreal, QC, H4B 1R6, Canada
DOI: 10.1039/c8nj00894a

## 2.1 Abstract

A series of complexes was prepared by self-assembly of copper(I) precursors and arylnitroso species. The nature of the copper(I) supporting ligand (bi-, tri- or tetradentate as well as secondary vs. tertiary amine donors) and the electronic nature of the arylnitroso species (electron-donating or withdrawing substituents) were varied. The stoichiometry of the reaction, the topology and the electronic properties of the adducts were characterized by means of UV-vis spectroscopy, X-ray diffraction and DFT methods. The more electron-rich ligands and the more electron-poor arylnitroso species lead to an inner-sphere electron-transfer and formation of copper(II)-(arylnitrosyl radical) complexes, with a linkage topology that depends on the denticity of the supporting ligand. These results provide a canvas by which to predict the products of similar self-assembled redox reactions.

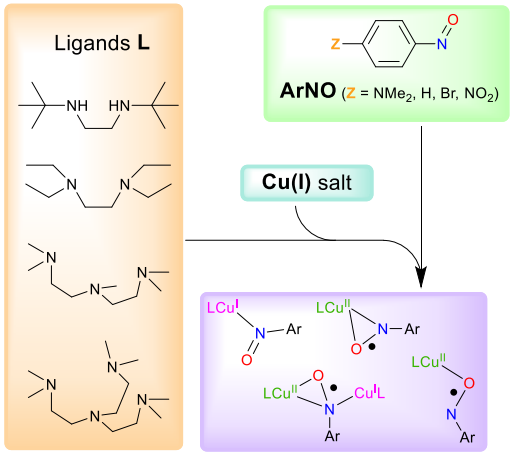


Scheme 2-1: Graphical Abstract

## 2.2 Introduction

Since the early reports of redox non-innocence of aryl C-nitroso species (ArNO),[24] the interaction of nitrosoarenes with metal complexes[2] has generated considerable interest due to their implication in biological[11–14] and catalytic C–N bond formation processes.[15–17] Recent reports have highlighted the

diverse redox states of ArNO ligands in metal complexes,[3–10] from ArN=O (arylnitroso) to $ArNO^{\bullet-}$ (arylnitrosyl radical) to $ArNO_2^-$ (doubly deprotonated hydroxylamine). This series, where partners differ by $1e^-$, is isoelectronic to the all-important $O_2$, $O_2^{\bullet-}$ $O_2^{2-}$ series ($O_2$, superoxide and peroxide). Understanding metal-ArNO interactions shall therefore inform on reactions involving $O_2$, reactive oxygen species (ROS) or on the similar HNO and NO nitric oxide chemistry.[14]

In metal-ArNO complexes, the steric and electronic requirements of the metal and auxiliary ligand determine the binding mode and oxidation state of the ArNO moiety. Since ArNO compounds are isoelectronic with singlet $O_2$, albeit less oxidizing, we have been using $Cu^I$ precursor complexes bearing alkylamine ligands that are commonly used in $Cu/O_2$ chemistry.[27,79] We have previously reported the $1e^-$ and $2e^-$ reduction of nitrosoarenes by such $Cu^I$ complexes and evidenced a controlled nitrene transfer in C–N bond forming reaction.[6,8] These results prompted us to study the effect of systematic variation of ligand and nitrosoarene on the bonding geometry and the electronic state of the nitroso moiety.

In this study, we selected four ligands that differ in their denticity and/or donor atoms: a secondary diamine (DBED), a tertiary diamine (TEED), a tertiary triamine ($Me_5$DIEN), and a tertiary tetraamine ($Me_6$TREN), all of which ensuring 5-chelation (Scheme 2-2). These ligands are known to support $Cu^I$ complexes that react with $O_2$ at low temperature to generate $Cu_nO_2$ adducts.[27,29] In addition, the reaction between $Me_6TRENCu^I$ and PhNO undergoes inner-sphere electron transfer to form a $PhNO^{\bullet-}$ radical anion that is O-bonded to a trigonal bipyramidal (TBP) $Cu^{II}$.[6] This species is a structural and electronic model of the biologically relevant $Me_6TRENCu^{II}(O_2^{\bullet-})$ superoxide species that is only observed transiently.[80]

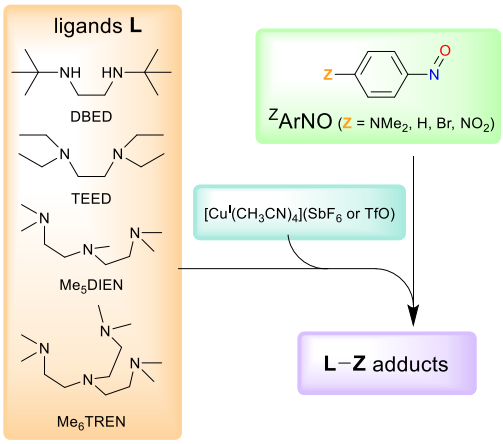


Scheme 2-2: General scheme for the formation of the L-Z adducts.

While being isoelectronic to $O_2$, ArNO species have the advantage of possessing a synthetic handle: the aromatic ring by which to vary their electronic properties. Thus, we selected four nitrosoarene species: *p*-(dimethylamino)nitrosobenzene, nitrosobenzene, p-bromonitrosobenzene and *p*-nitrosonitrobenzene, herein noted $^{Z}$ArNO (Z = $NMe_2$, H, Br and $NO_2$, Scheme 2-2).

The adducts formed between the $Cu^{I}$ complex of ligand L and a $^{Z}$ArNO species are herein noted **L-Z** for simplicity. These adducts were characterized in solution by their UV-vis spectra obtained by titration a solution of $LCu^{I}$ with $^{Z}$ArNO. Subsequent multivariate fitting of the spectral growth was performed against various stoichiometry models, but most obeyed a 1:1 binding law with low residuals (Figure S1-1: Screenshots of the fitting process with ReactLab$^{TM}$ Equilibria for **TEED-H**: (top) 1:1 Cu:ArNO model (bottom) 2:1 Cu:ArNO model. and Figure S1- 2). The fitting yielded the spectra of the pure adduct as well as the binding constant K (Equation 1, Table 2-1). In the solid state, the **L-Z** adducts were characterized by X-ray crystallography whenever possible. In this case, acetonitrile from the starting $Cu^{I}$ material, $[Cu(CH_3CN)_4](X)$ ($X^-$ = $SbF6^-$ or $TfO^-$) had to be removed by precipitating the complex in pentane, lest decomplexation occurred upon crystallizing, leading to the starting $LCu^{I}$ complex, the $^{Z}$ArNO species and/or $^{Z}$ArNO decomposition products.

$$n\ LCu^{I} + {}^{Z}ArNO \underset{}{\overset{K}{\rightleftharpoons}} \mathbf{L{-}Z} \qquad \text{Equation 1}$$

In what follows, it will be apparent that more donating ligands and more electron poor $^{Z}$ArNO lead to more unstable and reactive adducts, some of which could not be characterized. Notwithstanding, the comprehensive ligand and electronic variation in this family of adducts enabled us to establish binding and electronic trends, which are summarized in Scheme 2-3.

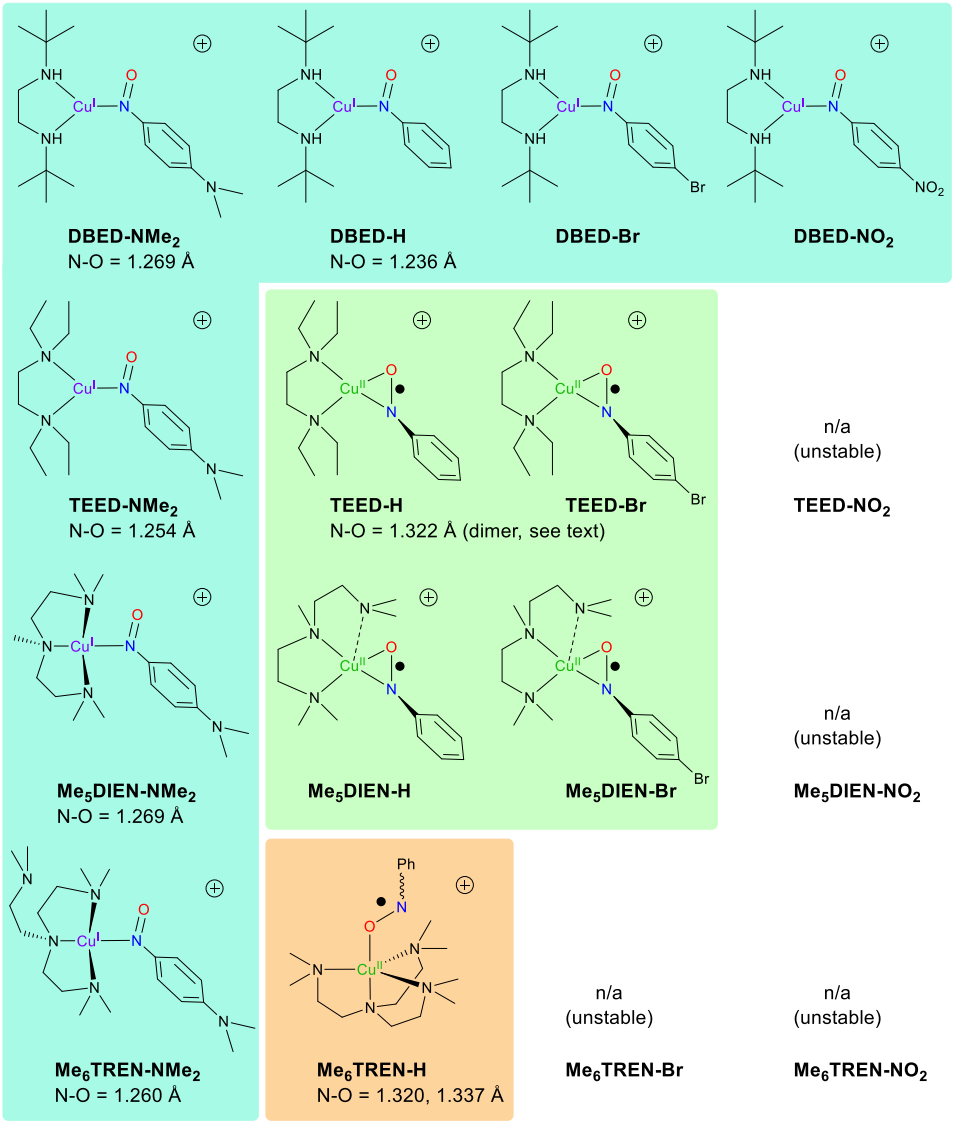


Scheme 2-3: Structure of the L-Z adducts, together with the N–O bond length in those characterized by crystallography (ref. 5 for **Me$_6$TREN**).

## 2.3 Results and discussion

### 2.3.1 Adducts with the secondary diamine ligand: DBED-Z

Reaction of [DBEDCu$^{I}$](X) (X$^{-}$ = $SbF_6^-$ or $TfO^-$) with $^{Z}$ArNO (Z = $NMe_2$, H, Br, $NO_2$) in THF led to the immediate formation of a deeply coloured purple (or red-purple for $NMe_2$) solution of **DBED-Z**. Titration of [DBEDCu$^{I}$]+ with $^{Z}$ArNO shows the rise of an intense absorption band around 540-590 nm with a shoulder at lower energy. Fitting the titration data with a 1:1 binding model led to excellent fits, wherefrom the spectra of the adducts can be extracted (Figure 2-1). Binding constants are within 3.6–

4.7 $\log_{10}$ units, with a net decrease on going to the more electron-poor Br and $NO_2$ arylnitroso species (Table 2-1). The Job plot for Z = $NO_2$ is consistent with a 1:1 stoichiometry (Figure 2-1 inset), an important aspect to check given that similar bidentate ligand N,N,N',N'-tetramethylpropylenediamine (TMPD) supports a 2:1 adduct with $^{NO2}$ArNO, [TMPDCu$^{II}$($\mu$-$\eta^2$:$\eta^2$-$^{NO2}$ArNO$^{2-}$)Cu$^{II}$TMPD]$^{2+}$, in which $^{NO2}$ArNO is reduced by 2e$^-$.[8]

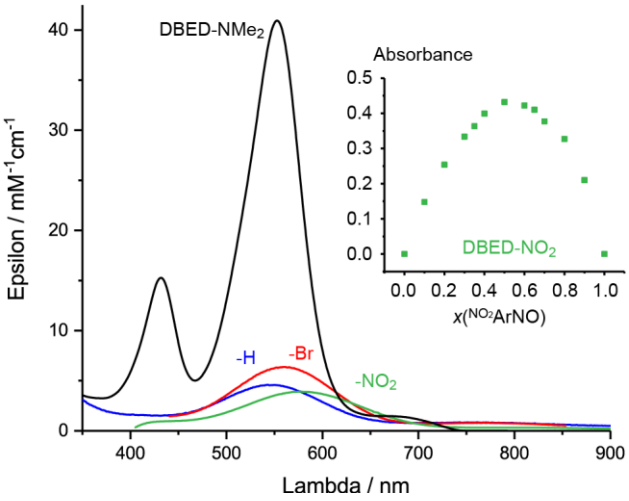


Figure 2-1: UV-vis spectra of **DBED-Z** species with Job plot for **DBED-NO$_2$**, in THF at 25°C.

Table 2-1: Stoichiometric and spectroscopic data of the **LCu-Z** adducts.[a]

| ↓L | Z → | NMe$_2$ | H | Br | NO$_2$ |
|---|---|---|---|---|---|
| **DBED** | model[b] | 1:1 | 1:1 | 1:1 | 1:1 |
| | $\log_{10}K$ | 4.03 | 4.65 | 4.10 | 3.61 |
| | λ / nm | 552 | 549 | 562 | 575 |
| **TEED** | model[b] | 1:1 | 1:1 / 2:1 | 1:1 | 1:1 |
| | $\log_{10}K$ | 4.06 | 3.94 / 6.03 | 4.07 | 3.72 |
| | λ / nm | 553 | 562 | 592 | 647 |
| **Me$_5$DIEN** | model[b] | 1:1 | 1:1 | 1:1 | 1:1 |
| | $\log_{10}K$ | 4.50 | 3.64 | 3.68 | 3.91 |
| | λ / nm | 545 | 454, 584 | 454,590 | 654 |
| **Me$_6$TREN** | model[b] | 1:1 | 1:1 | | |
| | $\log_{10}K$ | 3.25 | 4.17 | n/a | n/a |
| | λ / nm | 551 | 510, 598, 942 | | |

[a] Data obtained by fitting titration data. [b] LCu:$^Z$ArNO stoichiometry for the binding model leading to lowest residuals.

The adducts were isolated as solids by precipitation in pentane of a 1:1 [DBEDCu$^I$]$^+$:$^Z$ArNO mixture. $^1$H-NMR spectra of these adducts are diamagnetic (e.g. Figure S1- 3). Crystals suitable for X-ray diffraction were obtained for **DBED-NMe$_2$** and **DBED-H** with $SbF_6^-$ counterions (Figure 2-2, Table S1- 1). Both indicate a 1:1 complex with an N-bonded ArNO moiety where the N–O bond lengths (1.236 and 1.269 Å)

are consistent with a N=O double bond character as in similar complexes.[2,7,16,17] Trigonal Y-shape coordination about the Cu atom, as well as Cu–$N_{DBED}$ bonds of 2.004-2.074 Å are consistent with a $Cu^{I}$ oxidation state. These adducts can therefore be assigned as being $Cu^{I}$-*κ*N-(ArN=O) species ensuing straightforward ligand exchange. The crystal structures of the more electron-poor **DBED-Br** and **DBED-$NO_2$** could not be obtained, in part because of the lower formation constants for these species and because they are less stable over long periods of time (see below). Notwithstanding, the similarity of their UV-vis spectra with that of **DBED-H** suggests the same assignment as $Cu^{I}$-*κ*N-(ArN=O) species. Therefore, no electron transfer to the $^{Z}$ArNO moiety is observed with the secondary diamine DBED ligand.

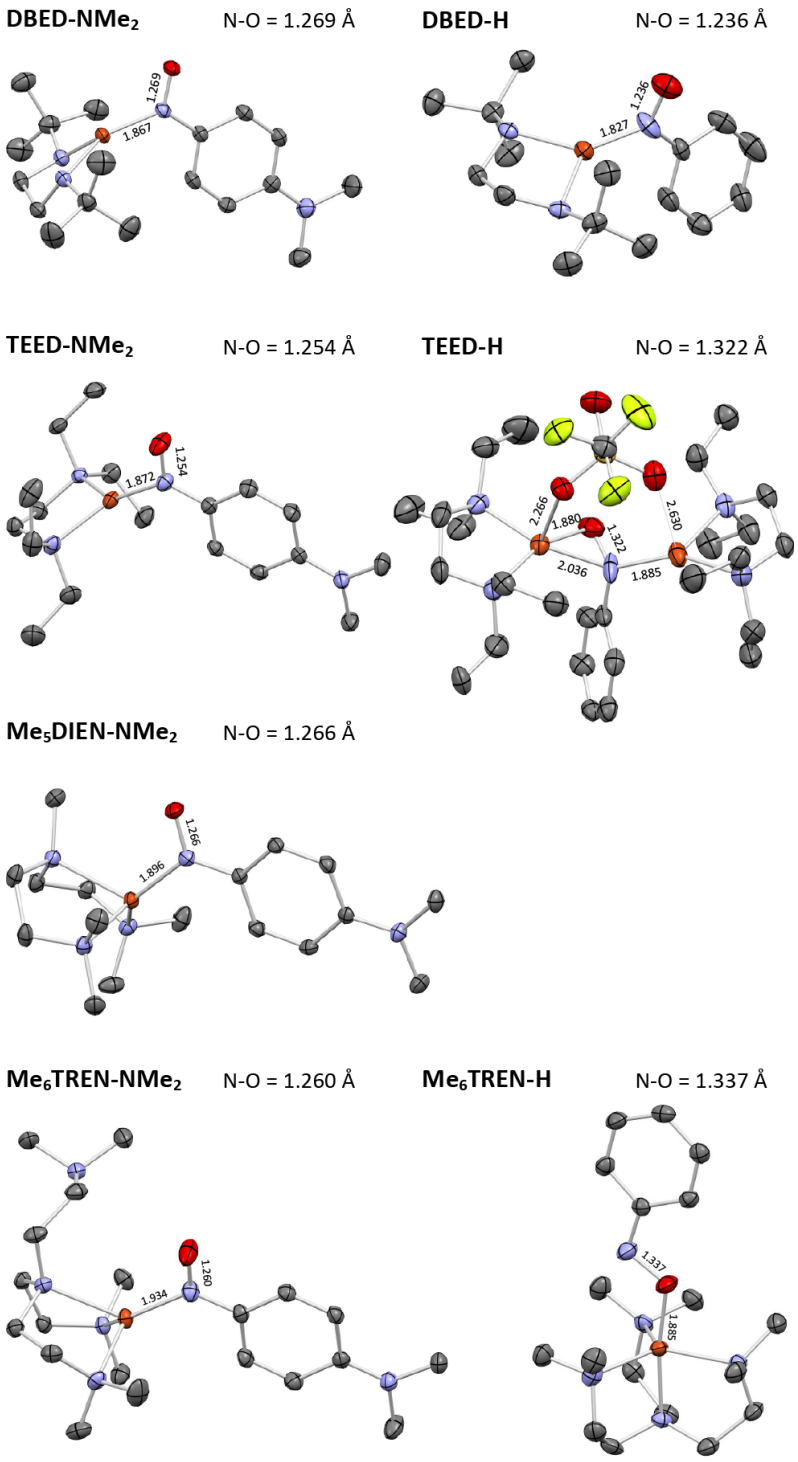


Figure 2-2: ORTEP at 50% ellipsoid probability of the **L-NMe$_2$** and **L-H** adducts with main bond lengths in Å. The hydrogen atoms, counteranions and solvent molecules were removed for clarity. Structure for **Me$_6$TREN-H** (with TfO) was redrawn from ref 6.

DFT calculations in the **DBED-Z** series were conducted to validate the assignment as $Cu^{I}$-*κ*N-(ArN=O) species. In the optimized structures, the N–O bonds refine to 1.25-1.27 Å, consistent with a genuine N=O character. TD-DFT calculations reveal the presence of one major visible electronic transition systematically red-shifted from the experimental values of 549-575 nm by 44-58 nm. Orbital analysis of this transition confirms a strong metal-to ligand charge transfer (MLCT) character that is consistent with Cu-to-ArNO backdonation. Thus, significant covalent character of the Cu–N bond and delocalization over the aromatic system explain the large intensity of these transitions. In-line with the theory, increasing the electron-withdrawing character of the para substituent of the ArNO fragment from $NMe_2$ to $NO_2$ enhances the completeness of the MLCT (Figure 2-3).

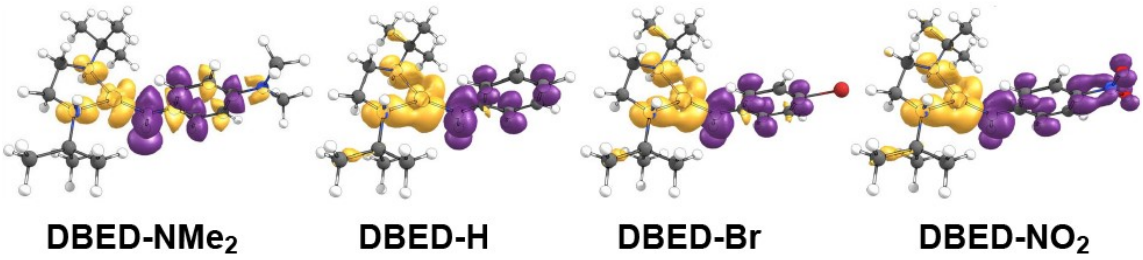


Figure 2-3: TD-DFT-calculated transitions of the main component of the ≈560 nm band as difference electron densities (EDD, yellow = negative, purple = positive). Theoretical computations are in-line with chemical intuition: more complete MLCT on excitation with more electron-withdrawing *para* substitution.[1]

### 2.3.2 Varying the ligand in the L-$NMe_2$ series

Since electron impoverishment of the $^{Z}$ArNO moiety did not induce $Cu^{I}$-to-$^{Z}$ArNO electron transfer in the DBED series, a second strategy to promote this electron transfer is to increase electron donation from the ligand. This justifies the choice of three ligands based on tertiary aliphatic amine donors: a diamine (TEED), a triamine ($Me_5$DIEN) and a tetraamine ($Me_6$TREN). In a first series of experiments, the adducts with $^{NMe2}$ArNO were characterized. Similarly to the above section, all L-$NMe_2$ adducts have very similar UV-vis spectra and are assigned as diamagnetic 1:1 complexes with genuine $Cu^{I}$ and ArN=O oxidation states (Figure 2-4). X-ray structures were obtained for **TEED-$NMe_2$** and **$Me_5$DIEN-$NMe_2$** with $SbF6^{-}$ counterions and for **$Me_6$TREN-$NMe_2$** with $TfO^{-}$ counterion (Figure 2-2). The N–O bond lengths in these complexes are within 1.254-1.269 Å, fully consistent with a N=O double bond character.[2,17] Akin to the structure of DBED-$NMe_2$, that of **TEED-$NMe_2$** displays a trigonal Y-shaped $Cu^{I}$ geometry. The structures of **$Me_5$DIEN-$NMe_2$** and **$Me_6$TREN-$NMe_2$** are very similar, with a tetrahedral $Cu^{I}$ geometry, meaning that

[1] All component transitions are MLCT, except for **DBED-Br** that has a significant LMCT contribution. See SI for details.

$Me_6$TREN effectively acts as a tridentate ligand in this case, with one of its $CH_2CH_2NMe_2$ arms not coordinated. This descent in denticity is confirmed in solution, as the NMR spectrum of $Me_6$TREN-$NMe_2$ is fluxional (Figure S1- 8). The ligand signals appear as one broad signal at 23°C, a sign that the arms of the ligand are competing with one another for coordination.

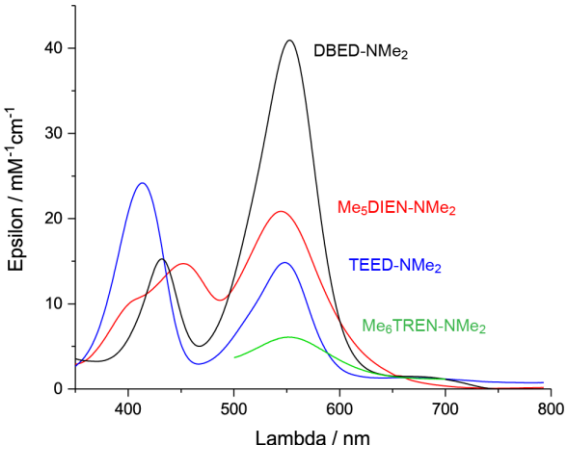


Figure 2-4: UV-vis spectra of **L-NMe$_2$** species in THF at 25°C.

### 2.3.3 L-H adducts with tertiary donors and electron-neutral $^{H}$ArNO

The reaction of TEED-Cu$^{I}$ with $^{H}$ArNO triggers a 1e electron-transfer from the Cu$^{I}$ to the arylnitroso moiety, generating a Cu$^{II}$-(arylnitrosyl radical anion) species. The crystal structure of **TEED-H**, reveals a 2:1 complex, [TEEDCu$^{II}$($\mu$-$\eta^2$:$\eta^1$-$^{H}$ArNO$^{\bullet-}$)Cu$^{I}$TEED](TfO)$_2$, with a side-on NO moiety and a N–O bond length of 1.322 Å, consistent with a bond order of 1.5 (Figure 2-2). This species is similar to the one characterized by Warren et al (N–O = 1.375 Å) using monoanionic β-diketiminate ligands.[4] One of the Cu centers is a square-pyramidal Cu$^{II}$ with shorter Cu–N distances to the ligand, coordination to both N and O of the $^{H}$ArNO moiety, and a weak axial interaction with the TfO$^-$ anion (Table S1- 1). The other Cu center is a trigonal Cu$^{I}$, as attested by Cu-NTEED distances of 2.048-2,130 Å and a negligible interaction with the $O_{PhNO}$ atom (2.666 Å) and the TfO$^-$ anion (2.630 Å).

Although **TEED-H** is dinuclear in the solid state, the Job plot suggests the formation of a 1:1 adduct in solution (Figure 2-5 inset). Warren showed that the LCu$^{I}$ moiety in such dinuclear species is labile and that mononuclear [LCu$^{II}$($\eta^2$-ArNO$^{\bullet-}$)] complexes are frequent (N–O = 1.330-1.338 Å).[4,7,81] In the case of **TEED-H**, titration data is better fitted as a 2:1 model, although the 1:1 fit is not invalidated by exceptionally large residuals (Figure S1- 1). We construe that both 1:1 and 2:1 species can coexist in solution (Scheme 2-4). On-going from solution to solid-state, the prevalent [TEEDCu$^{II}$($\eta^2$-$^{H}$ArNO$^{\bullet-}$)]$^+$

species associates an equivalent of $[TEEDCu^{I}]^{+}$ to lead to a more stable dinuclear complex, perhaps because the $TfO^{-}$ anion is poised to act as a bridging ligand.[2]

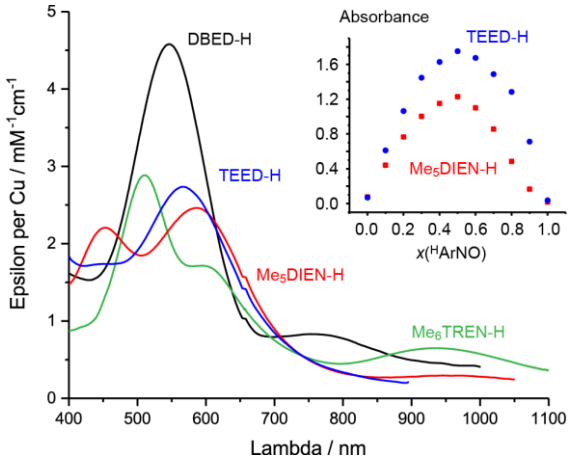


Figure 2-5: UV-vis spectra of **L-H** species with Job plots for **TEED-H** and **$Me_5$DIEN-H**, in THF at 25°C.

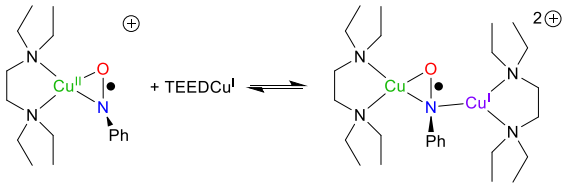


Scheme 2-4: Mono/dinuclear equilibrium for **TEED-H**.

The **$Me_5$DIEN-H** adduct has the same UV-Vis signature as **TEED-H**, which leads us to conclude that it too has the $Cu^{II}$-($\eta^2$-$^{H}ArNO^{\bullet-}$) formulation (Figure 2-5). In solution, titration data is better fitted as a 1:1 model (Figure S1- 2), suggesting that dimerization does not occur, perhaps because the third amine prevents $TfO^{-}$ binding and bridging to another Cu center. The Job plot is, however, slightly asymmetric, suggesting the possibility that the 2:1 adducts can exist in solution when [$Me_5$DIENCu] > [$^{H}$ArNO] and that other species could form at other ratios far from 1:1. We were unable, to crystallize this air-sensitive species despite using several anions, solvents and crystallization techniques.

Electron transfer occurs too in **$Me_6$TREN-H**, but the adducts adopt a very different geometry compared with bi and tridentate ligands, which translates in very different UV-vis spectra (Figure 2-5).[6] In this case, $Me_6$TREN remains tetradentate, leaving only one position open for $^{H}$ArNO coordination. Thus, the $^{H}ArNO^{\bullet-}$ anion bind via its O atom to the trigonal-bipyramidal $Me_6TRENCu^{II}$ center. X-ray structures of

[2] Anecdotally, we have a case where both crystals of the mononuclear and dinuclear species are found within the same sample crystallized from a 1:1 ratio of $LCu^{I}$ and a nitrosoarene. This will be reported at a later date.

this adduct depend on the anion used. With $SbF6^-$, a bent Cu–N–O–Ph linkage is observed in the solid-state and the solid is completely diamagnetic.[3] With $TfO^-$, a coplanar Cu–N–O–Ph linkage is observed in the solid-state, and the solid exhibits strong ferromagnetic coupling (fits to the SQUID data suggest a triplet-singlet gap in excess of 200 $cm^{-1}$).[6] In solution, however, both [$Me_6$TRENCu($^{H}$ArNO)](X) adducts ($X^-$ = $SbF_6^-$ or $TfO^-$) are paramagnetic, as indicated by wide $^1$H-NMR spectra extending from –33 to 20 ppm (Figure S1- 9). This is consistent with a "floppy" Cu–N–O–Ph linkage in solution with an average position near Cu–N–O–Ph coplanarity. This situation would minimize the overlap between the magnetic orbitals ($dz^2$ of $Cu^{II}$ and π of radical) and ensure a small singlet-triplet gap leading to a paramagnetic NMR spectrum.[82] The discrepancy between solid-state and solution structures is a testament that self-assembled structures are very sensitive to external parameters and that their geometry and electronic structure are fully subjected to thermodynamic control.

### 2.3.4 Adducts with tertiary donors and electron poor $^{Z}$ArNO

Adducts with electron-poor $^{Br}$ArNO and $^{NO2}$ArNO are much more reactive and unstable than **L-H** adducts, and we were unable to obtain crystal structures with any of the four ligand used here. Solution studies, however, reveal a strong similarity between the UV-Vis spectra of **TEED-Br** and **$Me_5$DIEN-Br** with that of **TEED-H** and **$Me_5$DIEN-H** (Figure 2-6), leading us to conclude that these adducts are side-on $Cu^{II}$-($^{Br}ArNO^{\bullet-}$) species. The **TEED-$NO_2$** and **$Me_5$DIEN-$NO_2$** adducts appear to be different and could perhaps have the 2:1 structure similar to that of [TMPDCu$^{II}$($\mu$-$\eta^2$:$\eta^2$-$^{NO2}$ArNO$^{2-}$)Cu$^{II}$TMPD]$^{2+}$, with a 2e$^-$-reduced ArNO moiety.[8] Further characterization of these $NO_2$ adducts was, however, inconclusive due to their instability.

[3] We also obtained the X-ray structure with $BPh_4^-$, where the Cu–N–O–Ph linkage is bent, but positional disorder of the Ph, N and O atoms prevents a sound structural analysis.

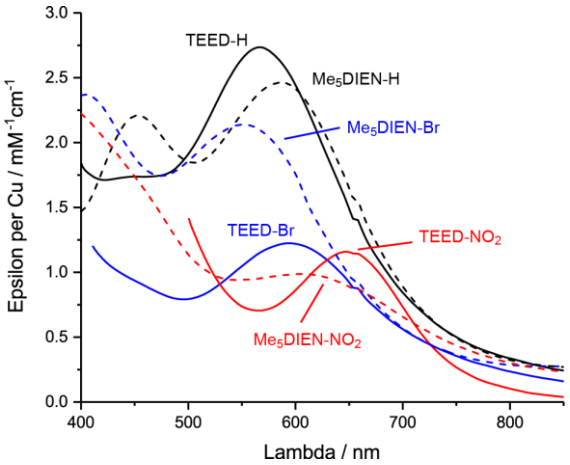


Figure 2-6: UV-vis spectra of **L-Br** and **L-NO$_2$** species (L = DBED, Me$_5$DIEN) in comparison with that of **L-H** species, obtained from titrations and multivariate fitting, in THF at 25°C. Note that the epsilons of the Br and especially the NO$_2$ adducts are approximate due to the instability of the adducts.

The reactivity of the **L-NO$_2$** adducts, and to a lesser extent **L-Br** adducts, stems from the stronger oxidizing properties of these ArNO species. When trying to crystallize **DBED-NO$_2$**, we obtained crystals of a light-red dinuclear Cu species, [DBEDCu$^{I}$($\mu$-$\eta^1$:$\eta^1$-DBDI)Cu$^{I}$DBED](SbF$_6$)$_2$, in which the bridging DBDI ligand is the di-imine obtained by doubly oxidation of DBED, *N,N'*-di-*tert*-butylethane-1,2-diimine (Figure 2-7a). The concomitant reduction of $^{NO2}$ArNO to the hydroxylamine inevitably yields the azoxy species, $^{NO2}$Ar–N$^+$(O$^-$)=N–Ar$^{NO2}$ by condensation.[24] These azoxy species are visible in the NMR spectra of the more electron-poor adducts, in quantities that increase on going from H to Br to NO$_2$ substitution (Figure S1- 7: $^1$H-NMR (500 MHz) spectra of (top to bottom) **Me$_5$DIEN-H**, **-Br** and **-NO$_2$** formed in situ in *d*$^6$-acetone at 23°C, showing the increasing amount of azoxy decomposition product (red *) on going to more electron-poor ArNO moieties. Whether they stem from this ligand oxidation/ArNO reduction mechanism or by Cu-catalyzed decomposition of the ArNO species is yet unknown. In some **DBED-NO$_2$** and **TEED-NO$_2$** samples, we also obtained crystals of the bis-hydroxido [L$_2$Cu$^{II}_2$($\mu$-OH)$_2$]$^{2+}$ species (L = DBED or TEED, Figure 2-7b).[4] These complexes are normally obtained when LCu$^{I}$ reacts with O$_2$ at room temperature.[79,83] However, because the crystallizations of the **L-Z** adducts were performed under inert atmosphere, we conclude that, like most self-assembled Cu/O$_2$ species,[27,28] **L-Z** species can become sufficiently oxidizing to abstract H atoms from solvent, adventitious water or the ligand over several days.

[4] The complete X-ray data of these adducts is not reported here due to low quality of the crystals, but there is no doubt as to the nature of these species in comparison with literature examples. Their presence is also seen as weak, broad paramagnetic signals in the NMR spectra of the adducts.

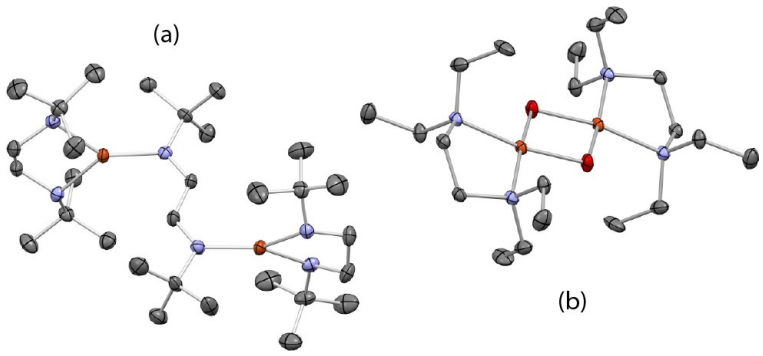


Figure 2-7: ORTEP at 50% ellipsoid probability of (a) the dication in [DBEDCu$^{I}$(μ-η$^{1}$:η$^{1}$-DBDI)Cu$^{I}$DBED](SbF$_6$)$_2$·THF and (b) the dication in [TEEDCu$^{II}$(μ-OH)$_2$Cu$^{II}$TEED](SbF$_6$)$_2$·THF. The hydrogen atoms, counteranions and THF molecules were removed for clarity.

## 2.4 Conclusion

The self-assembly of arylnitroso species with Cu$^{I}$ complexes is highly sensitive to the ligand denticity and electron-donating ability. Inner-sphere electron transfer is (so far) only observed with tertiary amine[6,8] or monoanionic[4,7,81] donors and requires sufficient donation from the ligand and/or electron-impoverishment of the arylnitroso moiety. The non-reduced ArNO moieties bind to Cu$^{I}$ via their N atom exclusively, with strong back bonding into the π system of the nitroso. When inner-sphere electron transfer occurs, the d$^9$ ligand-field preferences of the Cu$^{II}$ center seem to dictate the overall geometry of the adduct: square-pyramidal with bi- and tridentate ligands and trigonal-bipyramidal with $C_3$-symmetric tetradentate ligands. The ArNO$^{\bullet-}$ moiety adapts to these coordination requirements and adopts a side-on N,O-bonding mode with bi- and tridentate ligands versus an end-on O-bonding mode with tetradentate ligands. This is proof again that the ligand is paramount in controlling the self-assembly process. We also note that the weakly coordinating TfO$^-$ anion seems better poised to stabilize the Cu$^{II}$ oxidation state than the virtually non-coordinating SbF$_6^-$ anion. The coordinating ability of anions was investigated in Cu/O$_2$ chemistry[84] and could also be a deciding factor, albeit secondary to the ligand, in the structure of the adducts. In conclusion, the present study provides a systematic canvas by which to anticipate the geometric and electronic structure of other metal complexes with redox-noninnocent ArNO, O$_2$ or HNO moieties.

## 2.5 Experimental

### 2.5.1 Materials and Instrumentation

Chemicals and solvents were purchased from commercial sources. Inhibitor-free solvents were dried using a MBraun SPS 800, transferred to an inert-atmosphere glovebox (MBraun Labmaster, <1 ppm of $O_2$ and $H_2O$, filled with a dry $N_2$ atmosphere), further degassed under vacuum, and stored over activated molecular sieves (4 Å). The ligands were distilled over $CaH_2$ under $N_2$ and stored in the glovebox. The $Cu^I$ salts $[Cu(CH3CN)_4](OTf)$ and $[Cu(CH3CN)_4](SbF_6)$ were prepared by adapting the Kubas method,[85] recrystallized twice and stored in the glovebox. $^H$ArNO was used as purchased and all the other $^Z$ArNO derivatives were synthesized via literature procedures.[86–89] All experiments were carried out under $N_2$ atmosphere, either in the glovebox or in air-tight glassware.

$^1$H-NMR spectra were recorded at 23 °C in a 5 mm air-tight tube prepared under $N_2$ atmosphere on a Varian VNMRS 500 MHz or Inova 300 MHz and referenced to internal tetramethylsilane. UV-visible spectra were recorded on a B&W Tek iTrometer equipped with fiber-optic cables or an Agilent 8453 spectrophotometer. X-ray crystallographic analysis was performed using the Cu-Kα microfocus or Mo-Kα source of a Bruker APEX-DUO diffractometer or, for **TEED-H**, the Cu-Kα enhanced source of an Oxford Diffraction Gemini A Ultra. Details regarding the crystallographic procedures are provided in the ESI and CIFs.

### 2.5.2 Synthesis

The **L-Z** complexes were synthesized by slow addition of relevant equivalents of a $^Z$ArNO solution to a stirring 1:1 solution of $Cu^I$ salt and ligand L in THF inside the glovebox. Crystals suitable for X-ray diffraction were grown by vapour diffusion or slow layered diffusion of pentane or diethyl ether into a THF solution of the complex at −30 °C in the glovebox. The $^1$H-NMR spectra of the **L-Z** adducts were recorded on redissolved solids (when these were stable, e.g. **TEED-NMe$_2$**) or on in-situ prepared L:$Cu^I$:$^Z$ArNO 1:1:1 mixtures in $CDCl_3$ or $d^6$-acetone. 1H-NMR spectra of the more stable diamagnetic species: **DBED-NMe$_2$** (500 MHz, $CDCl_3$): δ 6.8-6.5 (m, 4H), 3.22 (s, 6H), 2.99 (s, 4H), 1.18 (s, 18H). **DBED-H** (500 MHz, $CDCl_3$): δ 8.14 (d, 2H), 7.77 (t, 1H), 7.66 (t, 2H), 2.93 (s, 4H), 2.72 (s, 2H), 1.20 (s, 18H). **DBED-Br** (500 MHz, $CDCl_3$): δ 7.99 (d, 2H), 7.80 (d, 2H), 2.90 (s, 4H), 2.67 (s, 2H), 1.20 (s, 18H). **DBED-NO$_2$** (500 MHz, $CDCl_3$): δ 8.48 (d, 2H), 8.22 (d, 2H), 2.87 (s, 4H), 2.57 (s, 2H), 1.23 (s, 18H). **TEED-H** (300 MHz, $CDCl_3$): δ 8.03 (d, 2H), 7.75 (t, 1H), 7.62 (t, 2H), 2.85 (q, 8H), 2.75 (s, 4H), 1.19 (t, 12H) **TEED-NMe$_2$** (500 MHz, $CDCl_3$): δ 8.51 (s, 1H), 7.46 (s, 1H), 7.16 (s, 1H), 6.70 (s, 1H), 3.29 (s, 6H), 2.91 (s, 8H), 2.83 (s, 4H),

1.20 (s, 12H). **Me5DIEN-NMe$_2$** (500 MHz, d$^6$-acetone): δ 7.98 (m, 2H), 6.96 (m, 2H), 3.29 (s, 6H), 2.84-2.72 (d, 8H), 2.51 (s, 12H), 2.10 (s, 3H). **Me$_5$DIEN-H** (500 MHz, d$^6$-acetone): δ 8.05 (d, 2H), 7.87 (t, 1H), 7.73 (t, 2H), 2.89-2.80 (d, 8H), 2.59 (s, 12H), 2.10 (s, 3H). **Me$_6$TREN-NMe$_2$** (500 MHz, d$^6$-acetone): δ 7.95 (broad, 2H), 6.95 (broad, 2H), 3.85 (very broad, 30H), 3.28 (s, broad, 6H).

### 2.5.3 Titration and multivariate data fitting

UV-visible titrations were performed under stirring inside the glovebox or in an air-tight quartz cell prepared in the glovebox. The cell was loaded with THF, then a solution of LCu$^{I}$ was syringed in. The titrant, $^{Z}$ArNO in THF, was added by aliquots and the spectra recorded 30s after each injection to allow for homogeneity. Datasets were fitted with different reasonable models by the ReactLab$^{TM}$ Equilibria software (Jplus Consulting) to obtain the best matching fit with minimum amount of residuals. The stoichiometry of the complexations was evaluated by the continuous variation method, better known as the Job plot.[90]

### 2.5.4 DFT calculation methods

The theoretical electronic spectra of the 4 analogous **DBED-Z** adducts were predicted using TD-DFT calculations. All calculations were performed on Gaussian 09[91] using the GGA pure DFT functional BP86 with the triple-zeta polarized Ahlrich basis set Def2TZVP. Geometry optimizations were carried out from X-Ray crystal structures using an ultrafine integration grid, tight SCF convergence criteria, and Polarized Continuum Model (PCM) solvent corrections for tetrahydrofuran (ε = 7.6). Using the single point geometries optimized under implicit solvation as input, 40 singlet excited states were calculated for each compound using TD-DFT at the same level of theory. The resulting theoretical fits of the UV-Vis spectra were plotted using GaussView, with the UV-Vis peak half width at the half height of 0.333 eV. Using ChemCraft, Electron Density Difference (EDD) plots were generated for each transition associated with the most intense predicted excited state in the visible range, not including de-excitations or excitations with small or negative CI expansion coefficients.

## 2.6 Acknowledgements

This work was funded by a Discovery Grant from NSERC (Canada), with support from the FRQNT Centre for Green Chemistry and Catalysis (Québec). We are grateful to Dr. Christopher Ceccarelli from Oxford Diffraction (Varian Inc.) for data collection on **TEED-H**.

# Chapter 3: A Stable Copper-Arylhydroxylamine Complex and its Conversion to a Hemilabile Arylnitroso

Joseph Zsombor-Pindera,† [a,b] Farshid Effaty,† [a] Leon Escomel, [a] Pierre Kennepohl*[b], Xavier Ottenwaelder*[a]

† Authors contributed equally to this work

[a] Department of Chemistry and Biochemistry, Concordia University, 7141 Sherbrooke W, Montreal, QC, H4B 1R6, Canada
[b] Department of Chemistry, University of British Columbia, 2036 Main Mall, Vancouver, BC V6T 1Z1, Canada

## 3.1 Abstract

We report the synthesis of a unprecedented copper(I)-arylhydroxylamine complex. The reactivity of the arylhydroxylamine complex is arrested by the presence of an intramolecular hydrogen bond that stabilizes the very weakly bound hydroxylamine. Upon two-electron oxidation, a copper(II)-(arylnitrosyl radical) complex is formed, which crystallizes as a copper(I) species with an uncoordinated arylnitroso function. This validates that such ligands may enable ligand redox chemistry and hemilability in copper complexes. Such tethered arylnitroso complexes present new opportunities for two-electron chemistry in earth-abundant metal catalysis.

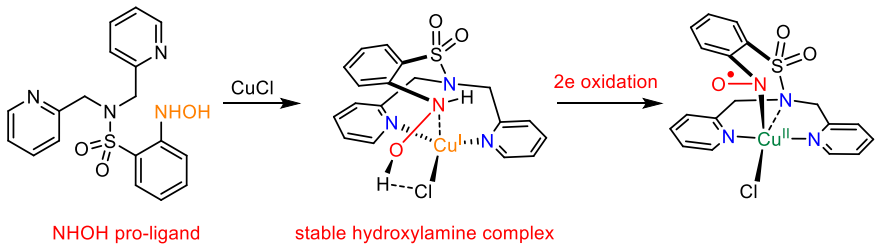


Scheme 3-1: Graphical Abstract

## 3.2 Introduction

Scarce noble metals like palladium and platinum are commonly used in contemporary fine-chemical synthesis because they favor two-electron redox processes necessary for catalysis of reactions such as cross-coupling and aerobic oxidation. Earth-abundant base metals, by contrast, tend to favor one-electron redox processes, which can be deleterious if they lead to the generation of free radicals. In order to get around this limitation, nature tends to pair metal ions with redox-active ligands. A prototypical example is galactose oxidase, the active form of which is a $Cu^{II}$ center coordinated to a

tyrosyl radical, allowing it to act like a noble metal by performing two-electron redox cycles between $Cu^{I}$-tyrosine and $Cu^{II}$-tyrosyl states.[25]

To mimic this biological strategy,[92] efforts have been made to find redox non-innocent synthetic ligands[93] capable of stabilizing radicals to enhance the oxidative malleability of 3d metals.[94] In recent years, nitrosoarenes (ArNO) have been recognized as a unique class of such ligands, potentially providing access to three charges while occupying only one or two coordination sites (Scheme 2a).[2,4,6,8,10,31,37,39,46,95] The possibility of hemilability[96,97] in these weak ligands further expands the range of possible chemical states available for complexes with ArNO ligands. These characteristics make them attractive candidates for ligand-participatory catalysis, in which ArNOs could act as electron reservoirs, enhancing the oxidative malleability of the metal center.

Until now, metal-ArNOs complexes have been notoriously difficult to stabilize,[31] particularly when forming intermolecular adducts of untethered ArNO ligands (Scheme 2b). In such cases, the entropic penalty for coordinative self-assembly leads to poor structural control.[37]

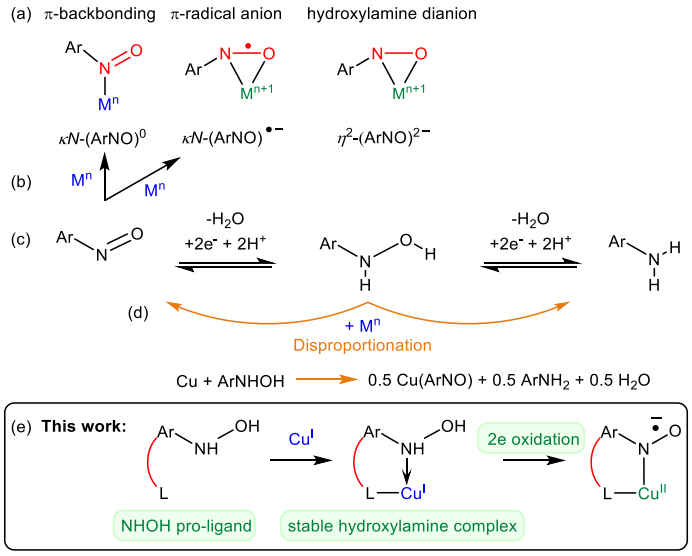


Scheme 3-2: (a) Common coordination modes of $ArNO^{0/-/2-}$. (b) Common reactions of low-valent metal complexes with ArNO. (c) Organic nitrogen group redox series (nitro excluded). (d) Disproportionation of ArNHOH with metal ions (e.g. Cu). (e) Strategy used in this work.

## 3.3 Results and Discussion

To overcome these limitations, we designed multidentate ligands containing a primary arylhydroxylamine (ArNHOH) function as pro-ligands for metal-ArNO species (Scheme 3-2e). These chelated metal-ArNO complexes are an especially interesting target because they could not only

stabilize M-NO bonds by the chelate effect but also control potential ArNO hemilability to enhance their reactivity. The reactivity of hydroxylamines with metal ions is also relevant due to their involvement in catalysis,[17,21,76] where the lack of mechanistic understanding is manifest. While disproportionation[7,98,99] or decomposition[100] of ArNHOH on complexation is common with 3d transition metals (Scheme 2-2b), we show herein that ligand design enables control of both reactivity and redox interconversions.

The hydroxylamine-containing ligand $L^{NHOH}$ (Scheme 3-3) was synthesized by carefully monitored activated zinc-catalyzed partial reduction of $L^{NO2}$ (see 0). Varying the reaction times and the number of equivalents of reductant allowed us to obtain pure samples of all three stable oxidation states, $L^{NO2}$, $L^{NHOH}$ and $L^{NH2}$.

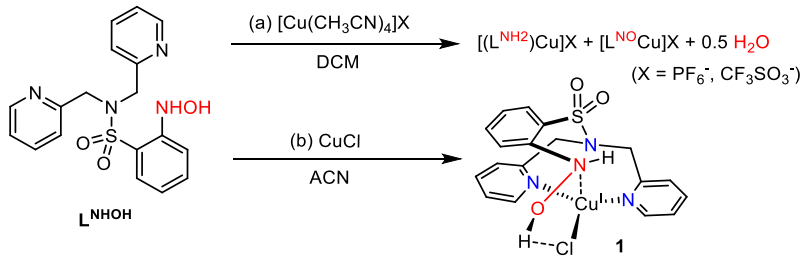


Scheme 3-3: (a) Disproportionation of $L^{NHOH}$ with $[Cu(CH_3CN)_4]PF_6$ (b) Capture of $L^{NHOH}$ by CuCl leading to $[L^{NHOH}CuCl]$ (**1**).

Reaction of $L^{NHOH}$ with $[Cu^{I}(CH3CN)_4](X)$ ($X^- = PF_6^-$ or $CF_3SO_3^-$) in DCM led to a purple solution ($\lambda_{max}$ = 508 nm with a shoulder at 650 nm) that contained products of the disproportionation of $L^{NHOH}$, $[L^{NO}Cu]^+$ and $[L^{NH2}Cu]^+$ as shown by ESI-MS (Scheme 3-3a, Figure S2- 6). Reaction of $L^{NHOH}$ with $Cu^{I}Cl$, however, led to a single well-defined species, namely $[L^{NHOH}CuCl]$ (**1**) in 75% yield, which precipitates as a yellow powder upon addition of a solution of $L^{NHOH}$ in ACN to a slurry of $Cu^{I}Cl$ in ACN (Scheme 3-3b). X-ray diffraction analysis of **1** shows a $Cu^{I}$ center in a T-shape geometry with two additional longer-distance interactions with the sulfonamide nitrogen ($N_{SO2}$), at 2.67 Å, and the ArNHOH nitrogen ($N_{NHOH}$) at 2.66 Å (Figure 3-1). **1** constitutes a very rare case of a complex with an intact primary hydroxylamine ligand[101,102] (some examples also exist with a ligated ArNHO– moiety[10,46] or secondary aminoxyl[103] groups). Upon closer inspection, it appears that the OH group is involved in a hydrogen bond with the Cl atom (O···Cl = 3.09 Å), possibly explaining the presence of the typically-unobserved intact ArNHOH moiety.

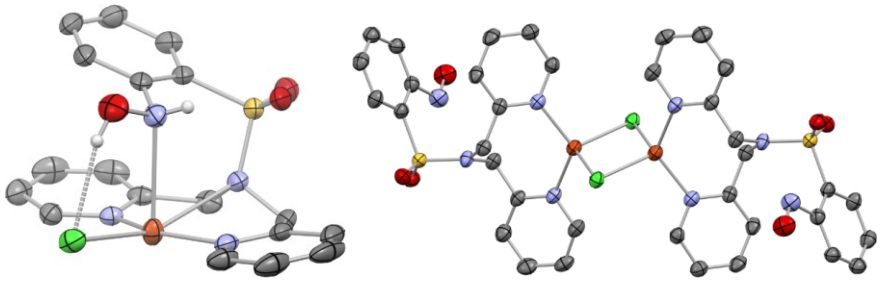

Figure 3-1: ORTEP view at 50% probability ellipsoids of **1** (left) and **3** (right). Crystallization solvent molecules and H atoms were omitted for clarity, except those on the NHOH function of **1**.

Oxidation of **1** by diethyl azodicarboxylate (DEAD) or diisopropyl azodicarboxylate (DIAD) leads to the formation a deep purple complex ($\lambda_{max}$ = 508 nm, $\varepsilon_{508}$ = 2450 $M^{-1}$ $cm^{-1}$), [$L^{NO}CuCl$], **2** Scheme 3-4a). Titration of **1** with DEAD in DCM reaches maximum absorbance at 2.0 equiv., suggesting that DEAD acts as a single hydrogen-atom abstractor (Figure 3-2).[104] Species **2** was characterized in solution by ESI-MS (m/z = 431.1 for $L^{NO}Cu^{+}$, Figure S2- 6), displays broadened $^{1}$H-NMR peaks in $CDCl_3$ (Figure S2- 14), and a frozen solution of **2** in DCM at 77 K is EPR-silent. Diffusion of pentane into a –30°C DCM solution of **2** produced by oxidation with DEAD yielded light red crystals after several days. X-ray diffraction of these crystals reveals that **2** dimerizes as a ($\mu$-Cl)$_2$Cu$_2$ complex, namely [$L^{NO}CuCl$]$_2$, **3**, in which the ArNO moiety is not coordinated (Figure 3-1). In this dimer, the NO bond of 1.236 Å is consistent with a double-bonded $(ArNO)^0$.[105]

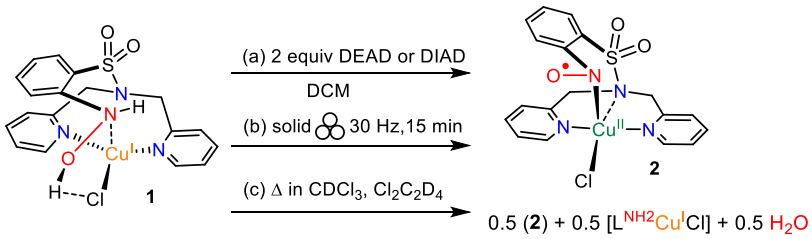


Scheme 3-4: (a) Oxidation of **1** by DEAD or DIAD to form **2**. (b) Mechanochemical disproportionation of **1** in plastic jars with a zirconia ball. (c) Heat-induced solution disproportionation of **1**.

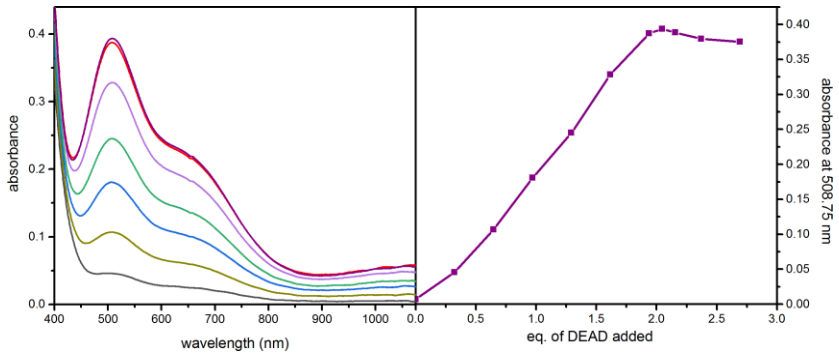


Figure 3-2: Titration of a 2.69 mM solution of **1** with 0-2.5 equiv. DEAD in DCM (pathlength 1.0 mm, 25°C), showing *in situ* formation of **2**. Inset: absorbance profile at 508 nm.

Interestingly, **1** also reacts without any additional reagent. When a microcrystalline sample of **1** was ground at 30 Hz for 15 min in a mechanochemical ball miller, a purple, amorphous powder was produced. Upon dissolution in DCM, this product had an absorbance spectrum similar to that of **2** ($\lambda_{max}$ = 508 nm). ESI-MS analysis (Figure S2- 13), however, revealed peaks for $[L^{NO}Cu]^+$ and $[L^{NH2}Cu]^+$, suggesting that milling **1** induced disproportionation to $[L^{NO}CuCl]$ and $[L^{NH2}CuCl]$ (Scheme 3-4b). Moreover, $^1$H-NMR monitoring of a solution of **1** in dry $CDCl_3$ sealed in a J-Young tube at 50°C (Figure S2- 14) showed formation of a $H_2O$ peak at 1.49 ppm, alongside loss of intensity of the methylene backbone peak at 1.52 ppm and formation of a new peak at 4.72 ppm after only 7.5 min. After 1 hour, the two methylene backbone peaks eventually equilibrated to a very broad peak at 4.67 ppm, suggesting formation of a mixture of complexes. As the solution was purple after the experiment, this is consistent with disproportionation of **1** into **2** + $[L^{NH2}CuCl]$ + 0.5 $H_2O$ (Scheme 3-4c). This suggests that input of energy, either by mechanical force or external heating, is capable of triggering decomposition of metastable **1** to its thermodynamic disproportionation products.

Given the redox-noninnocence of ArNO, two formulations of **2** are possible: $[(LNO)^0Cu^ICl]$ with an N=O double bond and $[(L^{NO\bullet-})Cu^{II}Cl]$, an arylnitrosyl π-radical with an N–O bond order of 1.5. Thus, three spin states are possible: a closed-shell $Cu^I$ singlet, $^1$**2**, a ferromagnetically-coupled $Cu^{II}$ triplet, $^3$**2**, or an antiferromagnetically-coupled $Cu^{II}$ singlet, $^1$**2**$_{AFC}$. To explore the electronic structure of **2**, Cu K-edge X-ray Absorption Spectroscopy (XAS) measurements were performed (Figure 3-3, 0). The XAS of **1** (15 mM in frozen DCM or in the solid state) is consistent with $Cu^I$, with an prominent edge feature at 8985.8 eV ascribed to the characteristic Cu 4p←1s shakedown peak typically observed in $Cu^I$ XAS.[106] The XAS of **2** (made with 3 eq DIAD, 15 mM in frozen DCM solution), on the other hand, exhibits features characteristic of a $Cu^{II}$ species, with an edge at 8985.0 eV, shifted 2.2 eV with respect to that of **1**, and a weak Cu 3d←1s pre-edge feature at 8977.6 eV.[106] The XAS spectrum of the product of

mechanochemically-induced disproportionation of **1** supports the formation of an amorphous solid-state mixture of $Cu^{I}$ and $Cu^{II}$ species. The data are consistent with ESI-MS data, which indicate formation of **2** + [$L^{NH2}$CuCl] upon milling.

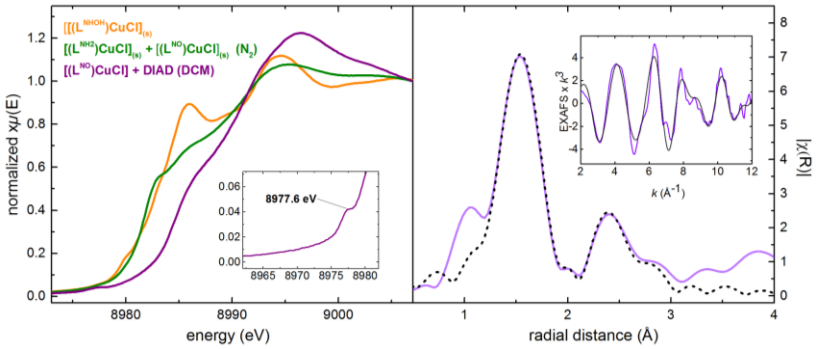


Figure 3-3: (left) Cu K-edge X-ray absorbance spectra of **1** (yellow), **2** (purple), and the product of mechanochemically-induced disproportionation of **1** in the solid state, under $N_2$ (green), (right) Fourier transform and $k^3$-space (inset) of the Cu K-edge EXAFS of a frozen solution of **2** in DCM, showing the best fit, performed using a *k*-range of 2-12 $Å^{-1}$ and an R-range of 1.1 to 3.1 Å.

DFT calculations at the CAM-B3LYP/Def2-TZVP level of theory predict the ferromagnetically-coupled triplet state $^{3}$**2** and the broken symmetry (BS) state $^{1}$**2**$_{AFC}$ to be very similar in energy, with the $^{3}$**2** being slightly favored by 5.0 kJ $mol^{-1}$ (1.2 kcal $mol^{-1}$) at this level of theory. Both the $^{3}$**2** and $^{1}$**2**$_{AFC}$ models are predicted to be κ*N*-(ArNO)$^{\bullet-}$ complexes, as expected from our Cu K-edge XAS data, with very similar distorted square-pyramidal geometries (see Figure 3-4). By contrast, the calculated closed-shell $^{1}$**2** state results in an $\eta^2$-N,O-(ArNO)$^0$ formulation at significantly higher energy (+42.2 kJ $mol^{-1}$, +10.10 kcal $mol^{-1}$).

TD-DFT calculations were also performed for **1**, $^{1}$**2**$_{AFC}$, yielding good agreement with the experimental XAS (Figure S2- 21, Figure S2- 22, Figure S2- 23) and qualitative agreement with the experimental UV-Vis (Figure S2- 24). Based on the latter calculations the visible maximum seen in the experimental UV-Vis spectrum of **2** at 508 nm can be tentatively assigned as a ligand to metal charge transfer (LMCT) from the ArNO π system to the unoccupied $Cu^{II}$ d-hole based on difference density plots (Figure S2- 25) The same MO assigned as the $Cu^{II}$ d-hole is the acceptor orbital in the Cu 3d←1s pre-edge transition state of the TD-DFT-calculated XAS of **2** (Figure S2- 22 and Figure S2- 23). These assignments suggest that the solution-phase spectra of **2** are consistent with the mononuclear $Cu^{II}$ model of **2** in which the ArNO moiety is coordinated as a κ*N*-(ArNO)$^{\bullet-}$.

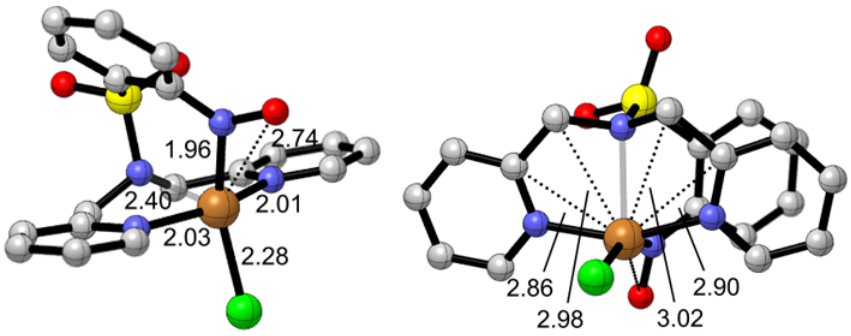


Figure 3-4: DFT model of $^{3}$**2**, optimized at the CAM-B3LYP/Def2-TZVP level of theory, showing distances relevant to EXAFS fit.

The Extended X-ray Absorbance Fine Structure (EXAFS) from the Cu K-edge XAS of **2** was fitted to scattering predictions based on the DFT-optimized $^{3}$**2** geometry (Figure 3-4). The resulting fit (Figure 3-3) is consistent with a nitrogen shell with a degeneracy of **3** at 1.98 Å, accounting for the $N_{Py}$ and $N_{NO}$, a Cu–Cl distance of 2.28 Å, a Cu–$N_{SO2}$ distance of 2.42 Å, a Cu–$O_{NO}$ distance of 2.61 Å, and a carbon shell with a degeneracy of 4 at 2.91 Å. Of these distances, the greatest variation from the DFT model is the Cu–ONO distance, which is 0.10 Å shorter in the EXAFS fit than in the DFT model, all other distances being within 0.03 Å of those predicted by DFT (Table S2- 4). Taken alongside DFT-supported spectral assignment and ESI-MS, these data strongly support the κ*N*-(ArNO)$^{\bullet-}$ model of **2**.[31]

Dehalogenation of the mixture of **2** and [$L^{NH2}$CuCl] produced by mechanochemically-induced disproportionation of **1** with NaBAr$^{F}_{4}$ in DCM (in absence of DIAD) leads to a dark purple solution, from which dark purple crystals can be obtained by diffusion of pentane and subsequent evaporation. X-ray diffraction reveals this complex to be a dinuclear $Cu^{II}$ complex, [($\mu$-$\eta^1$:$\eta^1$-$L^{NO\bullet-}$)($\mu$-$L^{NH-}$)$Cu^{II}_2$](BAr$^{F}_{4}$)$_2$ (**4**) in which $L^{NH2}$ has been deprotonated to $L^{NH-}$ and the Cu-$N_{NO}$ bond from the second $Cu^{II}$ center to $L^{NO}$ remains intact (Figure 3-5). In this case, the N–O bond length of 1.322 Å is consistent with an (ArNO)$^{\bullet-}$ oxidation state.

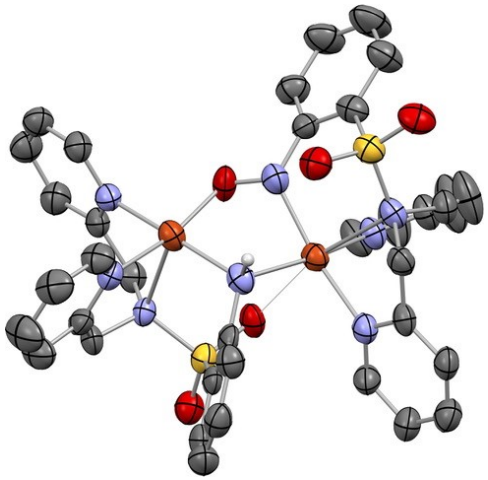

Figure 3-5: ORTEP view at 50% probability ellipsoids of **4**. Counter-ions and hydrogen atoms were omitted for clarity, except the H on the $NH^{-}$ function.

The crystal structure of **4** confirms that $L^{NO}$ can bind to $Cu^{II}$ as a κ*N*-$(ArNO)^{\bullet-}$ and the crystal structures of **3** shows that $L^{NO}$ can easily dissociate, forming a pendant $(ArNO)^{0}$ and reducing $Cu^{II}$ back to $Cu^{I}$. These data show that $L^{NO}$ behaves as a hemilabile redox non-innocent ligand. The hydroxylamine complex **1** is relatively inert at room temperature but decomposes readily at 50°C in $CDCl_3$. We note that the Cu-$N_{NHOH}$ bond in **1** is particularly long and that the structures indicates the presence of a short Cl…$H_{NHOH}$ distance consistent with the stabilizing influence of a hydrogen bond.

## 3.4 Conclusion

We therefore propose that **1** represents a trapped intermediate of the disproportionation reaction stabilized through intramolecular hydrogen bonding to the halide ligand. We have shown that **1** can be converted selectively, either to the typical disproportionation products, 0.5 **2** + 0.5 $[(L^{NH2})CuCl]$ + 0.5 $H_2O$, or purely to **2**. We submit that trapping of $L_nArNHOH$ by inclusion of a good hydrogen bond acceptor adjacent to a metal center can be used as a general strategy for synthesis of complexes of $L_nArNO$, in which the ArNO can act as a hemilabile redox non-innocent ligand.

## 3.5 Experimental

All experiments were carried out under inert atmosphere of nitrogen. All experimental details are provided in the Supporting Information.

## 3.6 Acknowledgements

The Natural Sciences and Engineering Council of Canada is acknowledged for Discovery Grants to P.K, X.O. and an Undergraduate Summer Award to J.Z.P. We are grateful to the Québec-funded Centre of Green Chemistry and Catalysis for additional resources. We are also grateful to Dr. Brian Patrick (UBC) for work on the X-ray structures of 3 and 4, Prof. Friščić, Prof. Cuccia and J.-L. Do for their help with solid-state experiments, and Dr. Ragnar Björnsson (MPI) for fruitful discussion and helpful suggestions on computational methodology.

# Chapter 4: Conclusion

## 4.1 Conclusion

This research has shown that arylnitrosos redox self-assembly to copper complexes is highly controlled by not only geometric factors like denticity of supporting ligand but also by the electronic nature of arylnitroso moiety and supporting ligand. The copper(I)-arylnitroso interactions can lead to an inner-sphere electron transfer process from copper center to the arylnitroso moiety. This suggests that copper-catalyzed arylnitroso-based reactions, such as the nitroso-ene transformation, could involve radical-type intermediates. Currently the proposed mechanisms are simply considering a $Cu^{I}/Cu^{II}$ redox shuttle (1 electron apart) to enact hydroxylamine /arylnitroso transformations (2 electrons apart). In light of our results, a deeper analysis of these mechanisms is warranted, especially to reach satisfactory structure-activity relationships.

It is commonly thought that arylhydroxylamines would normally react with copper ions to form its disproportionation products, amine and nitroso. In this work, we show that an intact hydroxylamine can be stabilized within a copper complex via intramolecular hydrogen bonding. This works especially reveals a large difference in the use of a copper(I) halide source compared with a weakly coordinating anion. This could have consequences in reactivity profiles. Furthermore, two-electron oxidation of this copper-hydroxylamine complex lead to the formation of a copper complex with a hemilabile arylnitroso function. The hemilability and redox noninnocence of this ligand could be beneficial in ligand-participatory catalysis.

## 4.2 Future Work

Below are proposed two directions for future work on these projects:

1) Exploring the Intramolecular hydrogen binding effects on stability of Intermolecular self-assembly of arylnitroso with copper centers by employing the supporting ligands that are capable of hydrogen bond donation to the nitroso moiety upon the coordination. One possible candidate for this type of supporting ligands could be the ligand that Solomon and Karlin has been using to stabilize copper(II)-superoxide species (Scheme 4-1).[107,108] This ligand should be capable of hydrogen bond donation to a coordinated nucleophile like arylnitrosos via the hydrogen on its amide group.

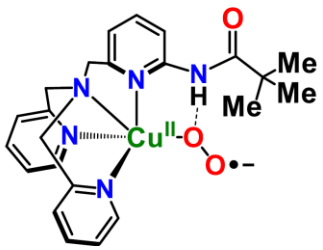


Scheme 4-1: Proposed supporting ligand for stabilization of unstable **LCu-Z** adducts. Adapted from [107].

2) Redesigning the $L^{NHOH}$ ligand in order to prevent dimerization in solid state. Since complex **2** dimerizes in solid state by bridging the chloride atom between copper centers which leads to de-coordination of arylnitroso moiety, this prevents us from studying the structural analysis of this complex in monomeric form with a coordinated nitroso group. The use of a bulkier ligand could help us for isolation and structural investigation of $L^{NO}Cu$ complex. One candidate for this approach would a ligand containing 6-substituents on the pyridine rings (Scheme 4-2).

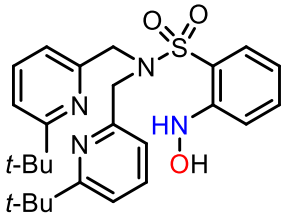


Scheme 4-2: Proposed ligand for future work on chapter 3.

# References


[1] A. B. McQuarters, L. E. Goodrich, C. M. Goodrich, N. Lehnert, *Zeitschrift fur Anorg. und Allg. Chem.* **2013**, *639*, 1520–1526.
[2] J. Lee, L. Chen, A. H. West, G. B. Richter-Addo, *Chem. Rev.* **2002**, *102*, 1019–1066.
[3] X. Dai, P. Kapoor, T. H. Warren, *J. Am. Chem. Soc.* **2004**, *126*, 4798–4799.
[4] S. Wiese, P. Kapoor, K. D. Williams, T. H. Warren, *J. Am. Chem. Soc.* **2009**, *131*, 18105–18111.
[5] N. C. Tomson, L. A. Labios, T. Weyhermüller, J. S. Figueroa, K. Wieghardt, *Inorg. Chem.* **2011**, *50*, 5763–5776.
[6] M. S. Askari, B. Girard, M. Murugesu, X. Ottenwaelder, *Chem. Commun.* **2011**, *47*, 8055–8057.
[7] K. D. Williams, A. J. P. Cardenas, J. D. Oliva, T. H. Warren, *Eur. J. Inorg. Chem.* **2013**, 3812–3816.
[8] M. S. Askari, M. Orio, X. Ottenwaelder, *Chem. Commun.* **2015**, *51*, 11206–11209.
[9] N. C. Tomson, K. D. Williams, X. Dai, S. Sproules, S. DeBeer, T. H. Warren, K. Wieghardt, *Chem. Sci.* **2015**, *6*, 2474–2487.
[10] S. Kundu, S. C. E. Stieber, M. G. Ferrier, S. A. Kozimor, J. A. Bertke, T. H. Warren, *Angew. Chem. Int. Ed.* **2016**, *55*, 10321–10325.
[11] M. R. Kumar, A. Zapata, A. J. Ramirez, S. K. Bowen, W. A. Francisco, P. J. Farmer, *Proc. Natl. Acad. Sci.* **2011**, *108*, 18926–18931.
[12] F. Doctorovich, D. E. Bikiel, J. Pellegrino, S. A. Suárez, M. A. Martí, *Acc. Chem. Res.* **2014**, *47*, 2907–2916.
[13] F. Doctorovich, D. E. Bikiel, J. Pellegrino, S. A. Suárez, M. A. Martí, in *Prog. Inorg. Chem. Vol. 58*, John Wiley & Sons, Inc., **2014**, pp. 145–184.
[14] Z. Miao, S. B. King, *Nitric Oxide* **2016**, *57*, 1–14.
[15] S. Otsuka, Y. Aotani, Y. Tatsuno, T. Yoshida, *Inorg. Chem.* **1976**, *15*, 656–660.
[16] R. S. Srivastava, M. A. Khan, K. M. Nicholas, *J. Am. Chem. Soc.* **2005**, *127*, 7278–7279.
[17] R. S. Srivastava, N. R. Tarver, K. M. Nicholas, *J. Am. Chem. Soc.* **2007**, *129*, 15250–15258.
[18] M. Kiese, *Pharmacol. Rev.* **1966**, *18*, 1091.
[19] P. Eyer, *Xenobiotica* **1988**, *18*, 1327–1333.
[20] P. J. O'brien, W. C. Wong, J. Silva, S. Khan, *Xenobiotica* **1990**, *20*, 945–955.
[21] C.-M. Ho, T.-C. Lau, *New J. Chem.* **2000**, *24*, 859–863.
[22] W. Adam, O. Krebs, *Chem. Rev.* **2003**, *103*, 4131–4146.
[23] N. Xu, G. B. Richter-Addo, in *Prog. Inorg. Chem. Vol. 59*, John Wiley & Sons, Inc., **2014**, pp. 381–446.
[24] P. Zuman, B. Shah, *Chem. Rev.* **1994**, *94*, 1621–1641.
[25] E. I. Solomon, D. E. Heppner, E. M. Johnston, J. W. Ginsbach, J. Cirera, M. Qayyum, M. T. Kieber-Emmons, C. H. Kjaergaard, R. G. Hadt, L. Tian, *Chem. Rev.* **2014**, *114*, 3659–3853.
[26] M. O. Ross, F. MacMillan, J. Wang, A. Nisthal, T. J. Lawton, B. D. Olafson, S. L. Mayo, A. C. Rosenzweig, B. M. Hoffman, *Science,* **2019**, *364*, 566.
[27] C. E. Elwell, N. L. Gagnon, B. D. Neisen, D. Dhar, A. D. Spaeth, G. M. Yee, W. B. Tolman, *Chem. Rev.* **2017**, *117*, 2059–2107.
[28] E. A. Lewis, W. B. Tolman, *Chem. Rev.* **2004**, *104*, 1047–1076.
[29] L. M. Mirica, X. Ottenwaelder, T. D. P. Stack, *Chem. Rev.* **2004**, *104*, 1013–1046.
[30] L. A. Labios, M. D. Millard, A. L. Rheingold, J. S. Figueroa, *J. Am. Chem. Soc.* **2009**, *131*, 11318–11319.
[31] B. R. Barnett, L. A. Labios, C. E. Moore, J. England, A. L. Rheingold, K. Wieghardt, J. S. Figueroa, *Inorg. Chem.* **2015**, *54*, 7110–7121.
[32] G. Matsubayashi, K. Nakatsu, *Inorg. Chim. Acta* **1982**, *64*, L163–L164.
[33] S. Hu, D. M. Thompson, P. O. Ikekwere, R. J. Barton, K. E. Johnson, B. E. Robertson, *Inorg. Chem.* **1989**, *28*, 4552–4554.

[34] N. G. Bokii, A. I. Udel'nov, Y. T. Struchkov, D. N. Kravtsov, V. M. Pachevskaya, *J. Struct. Chem.* **1977**, *18*, 814–819.
[35] S. J. Fox, L. Chen, M. A. Khan, G. B. Richter-Addo, *Inorg. Chem.* **1997**, *36*, 6465–6467.
[36] L.-S. Wang, L. Chen, M. A. Khan, G. B. Richter-Addo, *Chem. Commun.* **1996**, 323–324.
[37] F. Effaty, J. Zsombor-Pindera, A. Kazakova, B. Girard, M. S. Askari, X. Ottenwaelder, *New J. Chem.* **2018**, *42*, 7758–7764.
[38] J. C. Stephens, M. A. Khan, K. M. Nicholas, *J. Organomet. Chem.* **2005**, *690*, 4727–4733.
[39] S. Dey, S. Panda, P. Ghosh, G. K. Lahiri, *Inorg. Chem.* **2019**, *58*, 1627–1637.
[40] C. Krinninger, C. Högg, H. Nöth, J. C. Gálvez Ruiz, P. Mayer, O. Burkacky, A. Zumbusch, I.-P. Lorenz, *Chem. – A Eur. J.* **2005**, *11*, 7228–7236.
[41] C. Krinninger, S. Wirth, P. Klüfers, P. Mayer, I. P. Lorenz, *Eur. J. Inorg. Chem.* **2006**, 1060–1066.
[42] R. Wilberger, C. Krinninger, H. Piotrowski, P. Mayer, I.-P. Lorenz, *Eur. J. Inorg. Chem.* **2004**, 2488–2492.
[43] K. K. H. Lee, W. T. Wong, *J. Chem. Soc. Dalt. Trans.* **1996**, 3911–3912.
[44] T. Iwasa, H. Shimada, A. Takami, H. Matsuzaka, Y. Ishii, M. Hidai, *Inorg. Chem.* **1999**, *38*, 2851–2859.
[45] D. L. Packett, W. C. Trogler, A. L. Rheingold, *Inorg. Chem.* **1987**, *26*, 4308–4309.
[46] E. Ferretti, S. Dechert, F. Meyer, *Inorg. Chem.* **2019**, *58*, 5154–5162.
[47] L. S. Liebeskind, K. B. Sharpless, R. D. Wilson, J. A. Ibers, *J. Am. Chem. Soc.* **1978**, *100*, 7061–7063.
[48] F. Ridouane, J. Sanchez, H. Arzoumanian, M. Pierrot, *Acta Crystallogr. Sect. C* **1990**, *46*, 1407–1410.
[49] S. K. Dutta, D. B. McConville, W. J. Youngs, M. Chaudhury, *Inorg. Chem.* **1997**, *36*, 2517–2522.
[50] E. B. Brouwer, P. Legzdins, S. J. Rettig, K. J. Ross, *Organometallics* **1994**, *13*, 2088–2091.
[51] S. J. Skoog, J. P. Campbell, W. L. Gladfelter, *Organometallics* **1994**, *13*, 4137–4139.
[52] S. J. Skoog, W. L. Gladfelter, *J. Am. Chem. Soc.* **1997**, *119*, 11049–11060.
[53] M. Pizzotti, F. Porta, S. Cenini, F. Demartin, N. Masciocchi, *J. Organomet. Chem.* **1987**, *330*, 265–278.
[54] M. J. Barrow, O. S. Mills, *J. Chem. Soc. A Inorganic, Phys. Theor.* **1971**, 864–868.
[55] M. Calligaris, T. Yoshida, S. Otsuka, *Inorg. Chim. Acta* **1974**, *11*, L15–L16.
[56] S. Stella, C. Floriani, A. Chiesi-Villa, C. Guastini, *J. Chem. Soc. Dalt. Trans.* **1988**, 545–547.
[57] H. G. Ang, W. L. Kwik, K. K. Ong, *J. Fluor. Chem.* **1993**, *60*, 43–48.
[58] D. W. Hoard, P. R. Sharp, *Inorg. Chem.* **1993**, *32*, 612–620.
[59] P. R. Sharp, D. W. Hoard, C. L. Barnes, *J. Am. Chem. Soc.* **1990**, *112*, 2024–2026.
[60] M. J. Scott, S. J. Lippard, *Organometallics* **1998**, *17*, 466–474.
[61] V. Mahadevan, J. L. DuBois, B. Hedman, K. O. Hodgson, T. D. P. Stack, *J. Am. Chem. Soc.* **1999**, *121*, 5583–5584.
[62] S. Herres-Pawlis, P. Verma, R. Haase, P. Kang, C. T. Lyons, E. C. Wasinger, U. Flörke, G. Henkel, T. D. P. Stack, *J. Am. Chem. Soc.* **2009**, *131*, 1154–1169.
[63] T. A. G. Large, V. Mahadevan, W. Keown, T. D. P. Stack, *Inorg. Chim. Acta* **2019**, *486*, 782–792.
[64] H. Yamamoto, N. Momiyama, *Chem. Commun.* **2005**, 3514–3525.
[65] H. Yamamoto, M. Kawasaki, *Bull. Chem. Soc. Jpn.* **2007**, *80*, 595–607.
[66] N. Momiyama, H. Yamamoto, *Org. Lett.* **2002**, *4*, 3579–3582.
[67] J. G. Aston, D. F. Menard, *J. Am. Chem. Soc.* **1935**, *57*, 1920–1924.
[68] A. R. Forrester, S. P. Hepburn, *J. Chem. Soc. C Org.* **1971**, 3322–3328.
[69] P. Ehrlich, F. Sachs, *Berichte der Dtsch. Chem. Gesellschaft* **1899**, *32*, 2341–2346.
[70] A. P. Chavannavar, A. G. Oliver, B. L. Ashfeld, *Chem. Commun.* **2014**, *50*, 10853–10856.
[71] S. Carosso, M. J. Miller, *Org. Biomol. Chem.* **2014**, *12*, 7445–7468.
[72] K. K. Wan, K. Iwasaki, J. C. Umotoy, D. W. Wolan, R. A. Shenvi, *Angew. Chem. Int. Ed.* **2015**, *54*, 2410–2415.
[73] X. Lu, *Org. Lett.* **2004**, *6*, 2813–2815.

[74] A. Srivastava, Y.-A. Ma, R. Pankayatselvan, W. Dinges, K. M. Nicholas, *J. Chem. Soc. Chem. Commun.* **1992**, 853–854.
[75] R. S. Srivastava, K. M. Nicholas, *J. Org. Chem.* **1994**, *59*, 5365–5371.
[76] R. S. Srivastava, M. A. Khan, K. M. Nicholas, *J. Am. Chem. Soc.* **1996**, *118*, 3311–3312.
[77] S. Murru, C. S. Lott, F. R. Fronczek, R. S. Srivastava, *Org. Lett.* **2015**, *17*, 2122–2125.
[78] Y. Yu, J. Srogl, L. S. Liebeskind, *Org. Lett.* **2004**, *6*, 2631–2634.
[79] L. M. Mirica, T. D. P. Stack, *Inorg. Chem.* **2005**, *44*, 2131–2133.
[80] M. Becker, F. W. Heinemann, S. Schindler, *Chem. – A Eur. J.* **1999**, *5*, 3124–3129.
[81] S. Kundu, C. Greene, K. D. Williams, T. K. Salvador, J. A. Bertke, T. R. Cundari, T. H. Warren, *J. Am. Chem. Soc.* **2017**, *139*, 9112–9115.
[82] P. Verma, J. Weir, L. Mirica, T. D. P. Stack, *Inorg. Chem.* **2011**, *50*, 9816–9825.
[83] L. M. Mirica, D. J. Rudd, M. A. Vance, E. I. Solomon, K. O. Hodgson, B. Hedman, T. D. P. Stack, *J. Am. Chem. Soc.* **2006**, *128*, 2654–2665.
[84] X. Ottenwaelder, D. J. Rudd, M. C. Corbett, K. O. Hodgson, B. Hedman, T. D. P. Stack, *J. Am. Chem. Soc.* **2006**, *128*, 9268–9269.
[85] G. J. Kubas, *Inorg. Synth.* **1990**, *28*, 68–70.
[86] A. Defoin, *Synthesis,* **2004**, 706–710.
[87] B. Priewisch, K. Rück-Braun, *J. Org. Chem.* **2005**, *70*, 2350–2352.
[88] R. S. Heying, L. G. Nandi, A. J. Bortoluzzi, V. G. Machado, *Spectrochim. Acta Part A Mol. Biomol. Spectrosc.* **2015**, *136*, *Part*, 1491–1499.
[89] G. Wu, J. Zhu, X. Mo, R. Wang, V. Terskikh, *J. Am. Chem. Soc.* **2010**, *132*, 5143–5155.
[90] J. S. Renny, L. L. Tomasevich, E. H. Tallmadge, D. B. Collum, *Angew. Chem. Int. Ed.* **2013**, *52*, 11998–12013.
[91] M. J. Frisch, G. W. Trucks, H. B. Schlegel, M. A. Robb, J. R. Cheeseman, G. Scalmani, V. Barone, G. A. Petersson, H. Nakatsuji, M. Caricato, et al., **2010**.
[92] L. Que, W. B. Tolman, *Nature* **2008**, *455*, 333–340.
[93] T. Storr, R. Mukherjee, *Inorg. Chem.* **2018**, *57*, 9577–9579.
[94] P. J. Chirik, K. Wieghardt, *Science,* **2010**, *327*, 794–795.
[95] S.-C. Chan, C.-Y. Wong, *Coord. Chem. Rev.* **2020**, *402*, 213082.
[96] V. T. Annibale, D. Song, *RSC Adv.* **2013**, *3*, 11432–11449.
[97] W. Kaim, K. Beyer, V. Filippou, S. Záliš, *Coord. Chem. Rev.* **2018**, *355*, 173–179.
[98] M. M. Gutierrez, G. B. Alluisetti, J. A. Olabe, V. T. Amorebieta, *Dalt. Trans.* **2009**, 1187–1194.
[99] Z. Rappoport, J. F. Liebman, Z. Rappoport, J. F. Liebman, *The Chemistry of Hydroxylamines, Oximes and Hydroxamic Acids*, John Wiley & Sons Ltd., **2009**.
[100] J. B. Gordon, A. C. Vilbert, I. M. DiMucci, S. N. MacMillan, K. M. Lancaster, P. Moënne-Loccoz, D. P. Goldberg, *J. Am. Chem. Soc.* **2019**, *141*, 7046–7055.
[101] S. V Fokin, G. V Romanenko, V. I. Ovcharenko, *Mendeleev Commun.* **2001**, *11*, 127–128.
[102] K. V Luzyanin, P. V Gushchin, A. J. L. Pombeiro, M. Haukka, V. I. Ovcharenko, V. Y. Kukushkin, *Inorg. Chem.* **2008**, *47*, 6919–6930.
[103] R. C. Walroth, K. C. Miles, J. T. Lukens, S. N. MacMillan, S. S. Stahl, K. M. Lancaster, *J. Am. Chem. Soc.* **2017**, *139*, 13507–13517.
[104] M. Usman, X.-W. Zhang, D. Wu, Z.-H. Guan, W.-B. Liu, *Org. Chem. Front.* **2019**, *6*, 1905–1928.
[105] D. Wang, X. Leng, S. Ye, L. Deng, *J. Am. Chem. Soc.* **2019**, *141*, 7731–7735.
[106] M. L. Baker, M. W. Mara, J. J. Yan, K. O. Hodgson, B. Hedman, E. I. Solomon, *Coord. Chem. Rev.* **2017**, *345*, 182–208.
[107] M. Bhadra, J. Y. C. Lee, R. E. Cowley, S. Kim, M. A. Siegler, E. I. Solomon, K. D. Karlin, *J. Am. Chem. Soc.* **2018**, *140*, 9042–9045.
[108] D. E. Diaz, D. A. Quist, A. E. Herzog, A. W. Schaefer, I. Kipouros, M. Bhadra, E. I. Solomon, K. D. Karlin, *Angew. Chem. Int. Ed.* **2019**, *58*, 17572–17576.
[109] B. Ravel, M. Newville, in *J. Synchrotron Radiat.*, **2005**, pp. 537–541.
[110] J. J. Rehr, J. J. Kas, F. D. Vila, M. P. Prange, K. Jorissen, *Phys. Chem. Chem. Phys.* **2010**, *12*,

5503–5513.
[111] M. O. Krause, J. H. Oliver, *J. Phys. Chem. Ref. Data* **1979**, *8*, 329–338.
[112] W. Jiang, N. J. Deyonker, A. K. Wilson, *J. Chem. Theory Comput.* **2012**, *8*, 460–468.
[113] A. P. De Lima Batista, A. G. S. De Oliveira-Filho, S. E. Galembeck, *Phys. Chem. Chem. Phys.* **2017**, *19*, 13860–13867.

# Appendix 1 - Supplemental Information for Chapter 2

## Ligand and Electronic Effects on Copper(I)-Arylnitroso Self-Assembly

### Examples of UV-vis multivariate fitting

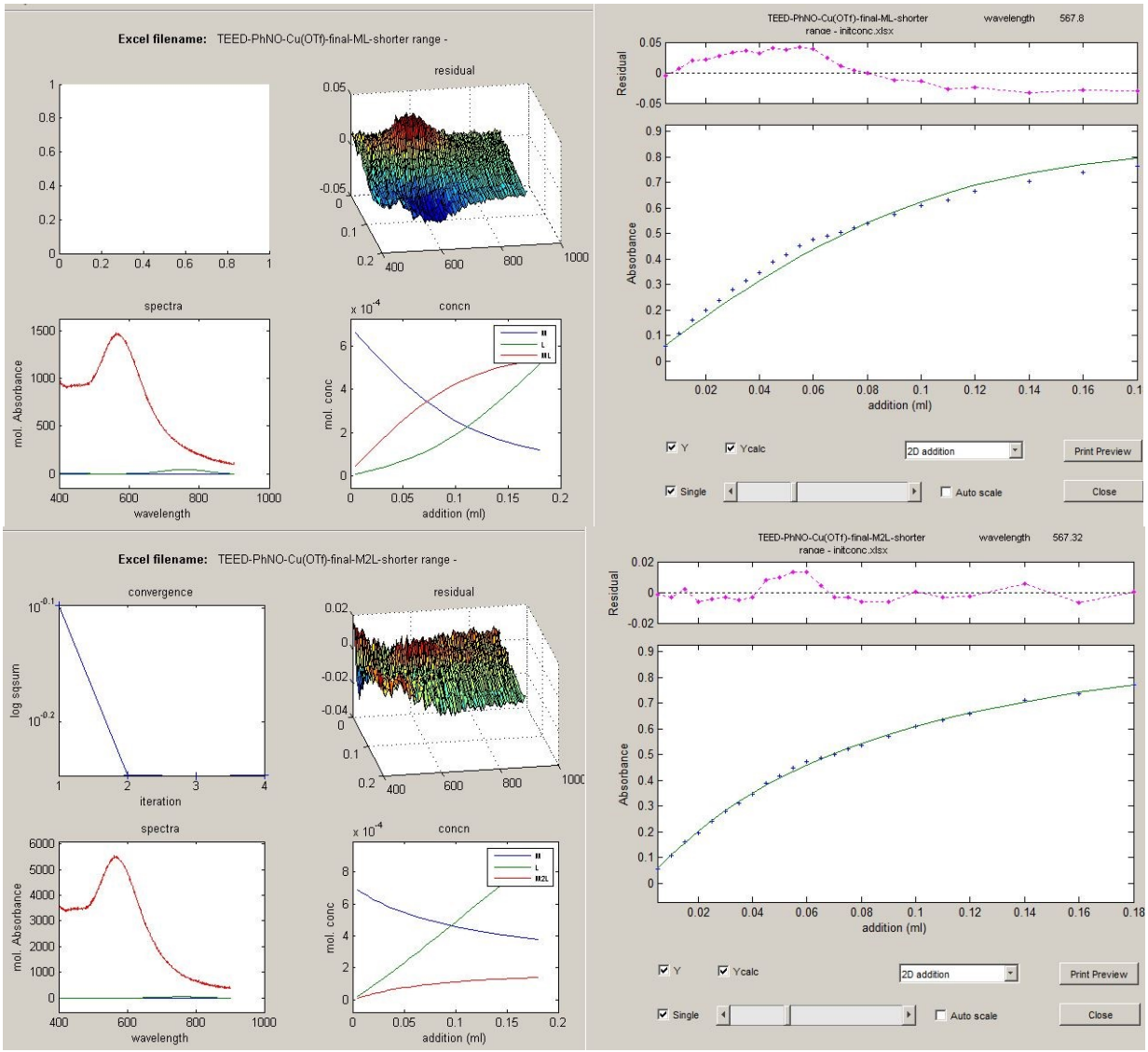


Figure S1- 1: Screenshots of the fitting process with ReactLab™ Equilibria for **TEED-H**: (top) 1:1 Cu:ArNO model (bottom) 2:1 Cu:ArNO model.

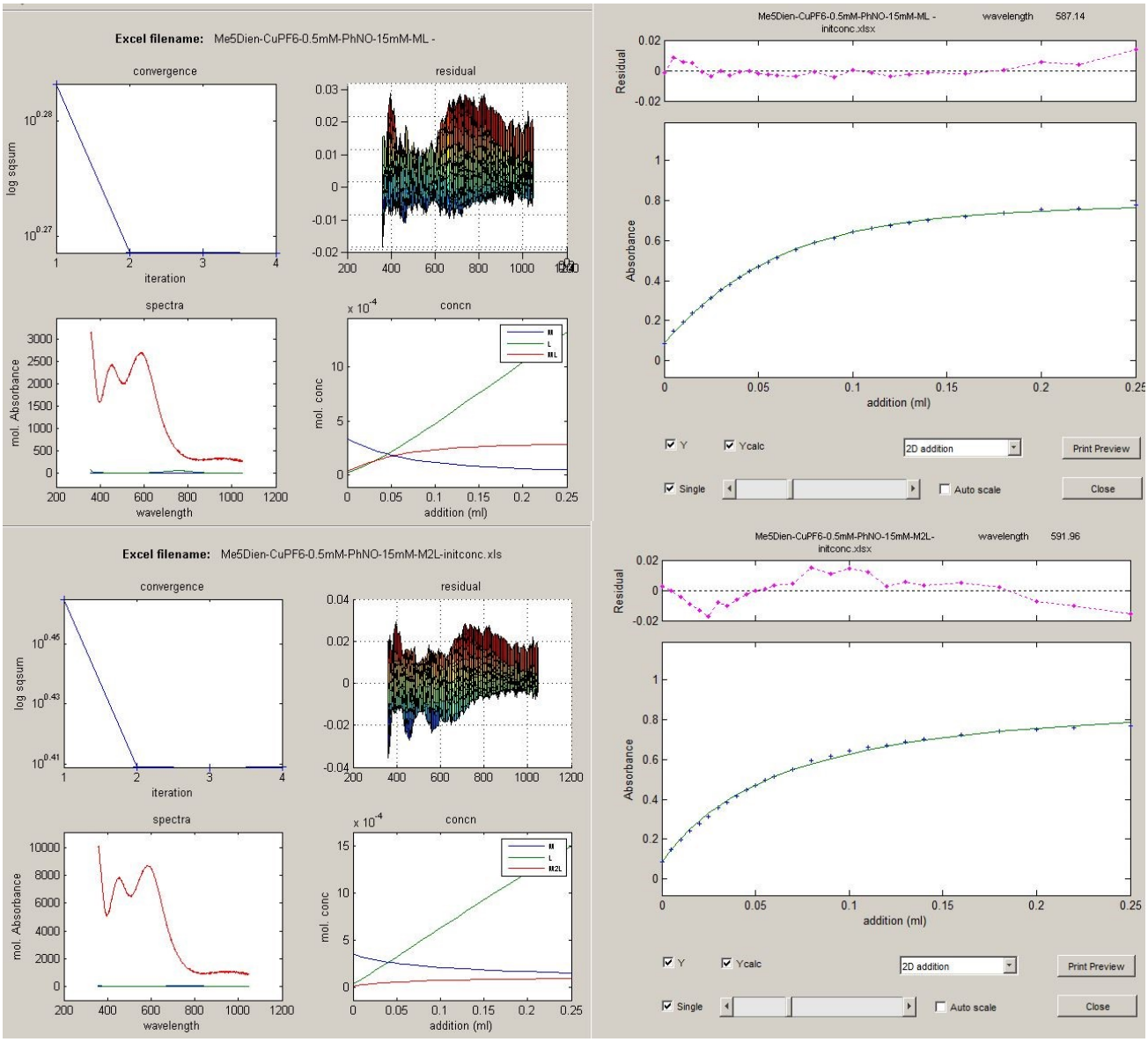


Figure S1- 2: Screenshots of the fitting process with ReactLab™ Equilibria for **$Me_5$DIEN-H**: (top) 1:1 Cu:ArNO model (bottom) 2:1 Cu:ArNO model.

## Selection of NMR spectra

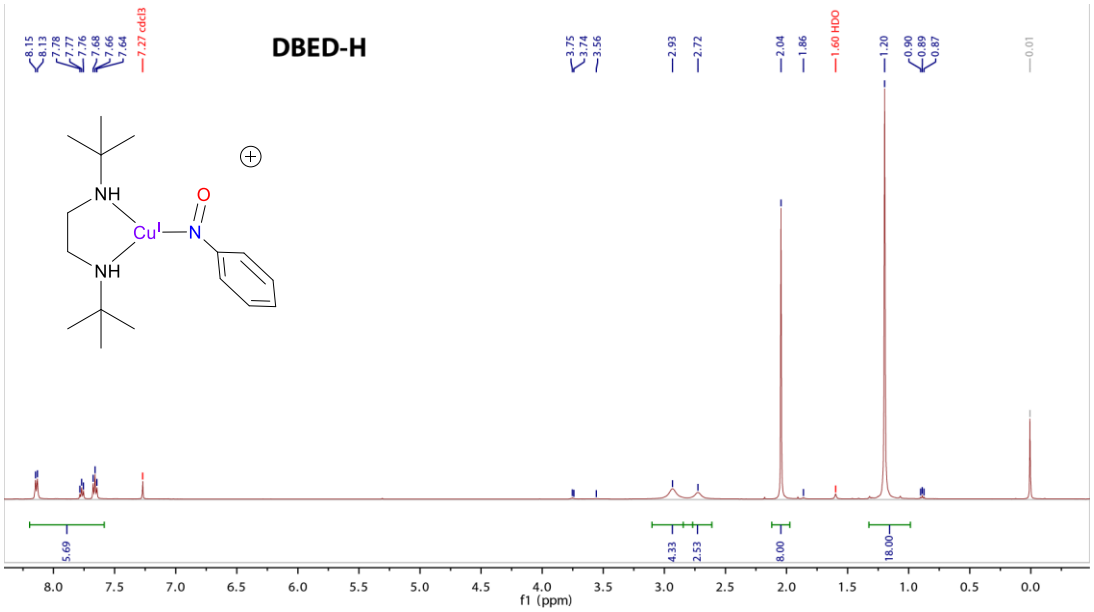


Figure S1- 3: $^{1}$H-NMR (500 MHz) spectra of **DBED-H** formed in situ in CDCl3 at 23°C.

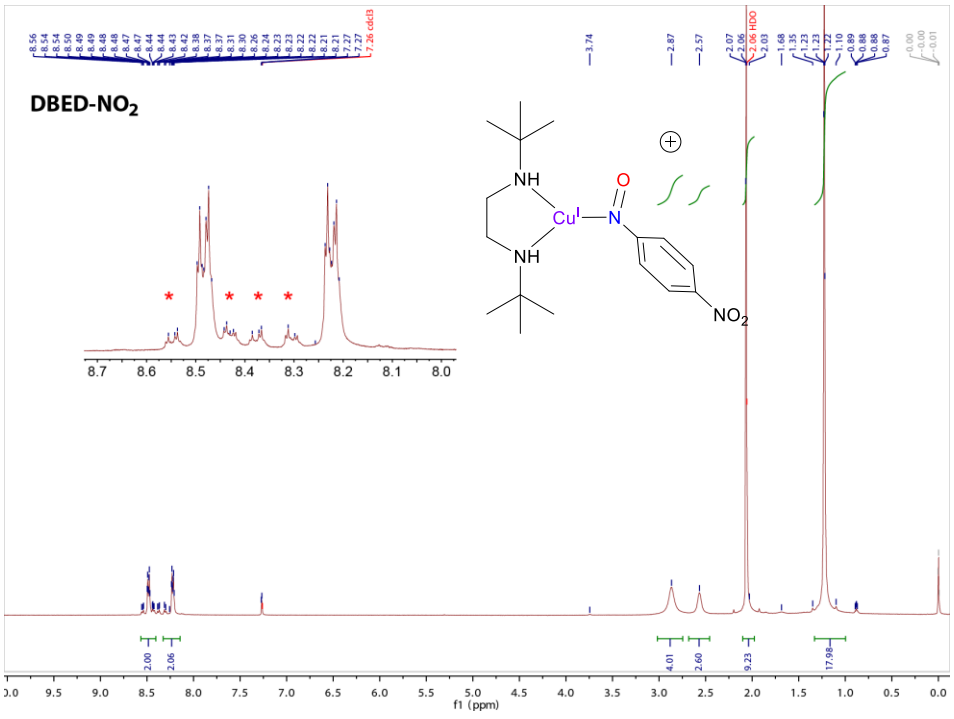


Figure S1- 4: $^{1}$H-NMR (500 MHz) spectra of **DBED-NO$_2$** formed in situ in $d^6$-acetone at 23°C. The red * in the inset denote the azoxy decomposition product.

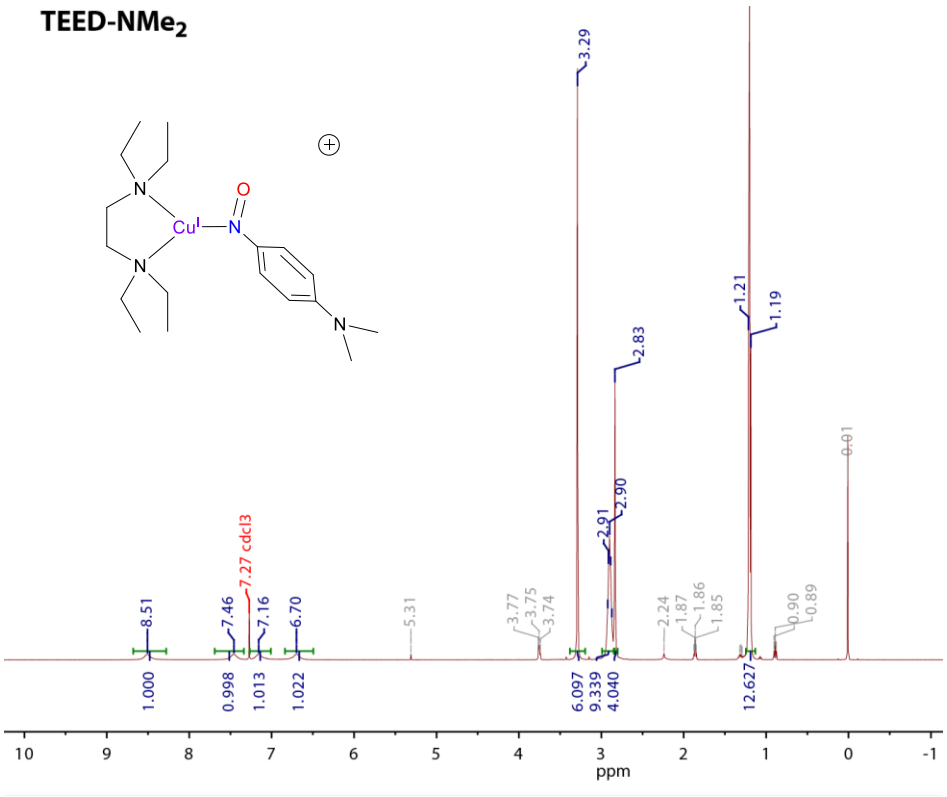


Figure S1- 5: $^{1}$H-NMR (500 MHz) spectra of **TEED-NMe$_2$** dissolved in CDCl3 at 23°C.

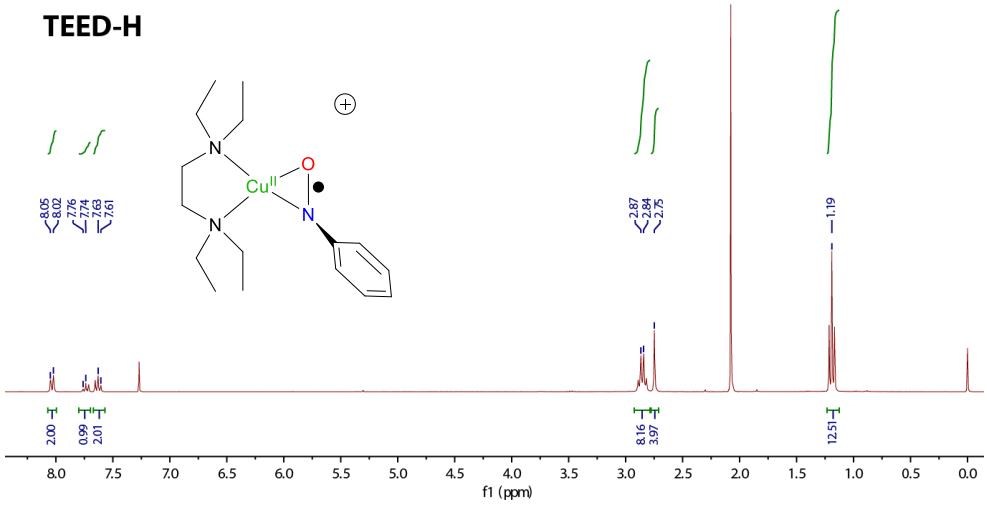


Figure S1- 6: $^{1}$H-NMR (300 MHz) spectra of **TEED-H** formed in situ from a 1:1 TEEDCuI:HArNO stoichiometry in CDCl3 at 23°C.

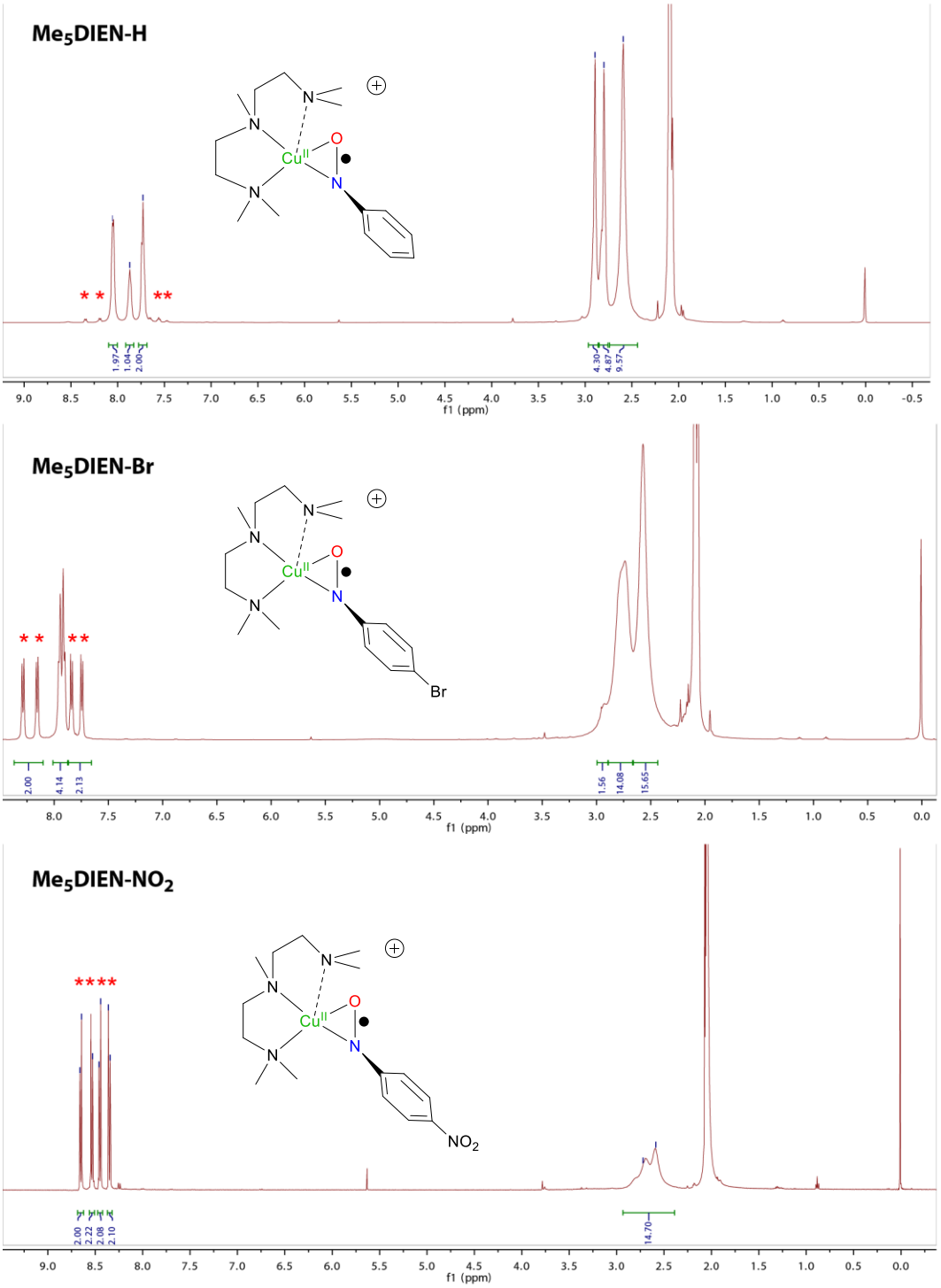


Figure S1- 7: $^{1}$H-NMR (500 MHz) spectra of (top to bottom) **Me$_5$DIEN-H**, **-Br** and **-NO$_2$** formed in situ in $d^6$-acetone at 23°C, showing the increasing amount of azoxy decomposition product (red *) on going to more electron-poor ArNO moieties.

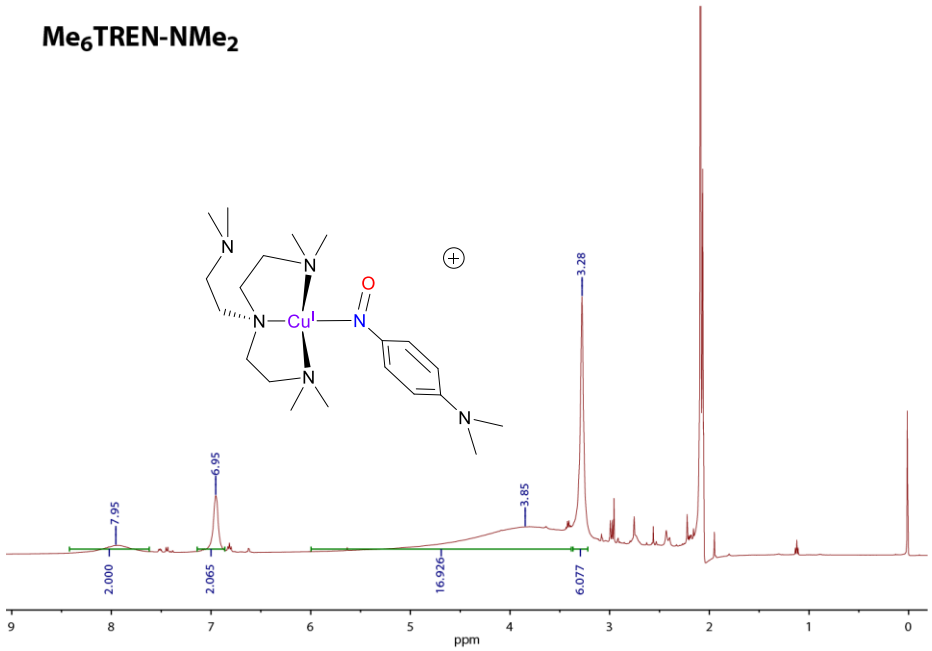


Figure S1- 8: $^{1}$H-NMR (500 MHz) spectra of **$Me_6$TREN-$NMe_2$** in d6-acetone at 23°C.

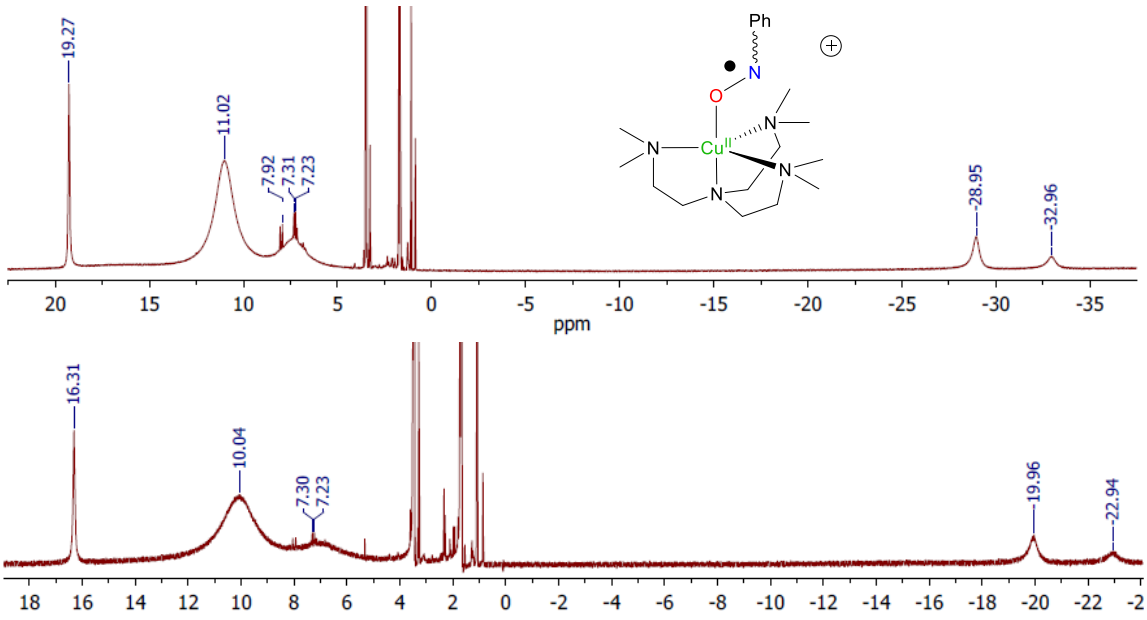


Figure S1- 9: $^{1}$H-NMR (500 MHz) spectra of **$Me_6$TREN-H** with $OTf^-$ (top) or $SbF_6^-$ (bottom) counteranions in $d^8$-THF at 23°C.

## X-ray Crystallography

X-ray crystallographic analysis was performed using the Cu-Kα microfocus or Mo-Kα source of a Bruker APEX-DUO diffractometer or, for **TEED-H**, the Cu-Kα enhanced source of an Oxford Diffraction Gemini A Ultra. The frames were integrated with the Bruker SAINT software package using a narrow-frame algorithm. Data were corrected for absorption effects using the multi-scan method (SADABS or TWINABS). The structures were solved by direct methods and refined using the Bruker APEX2 or APEX3 software package (SHELXL instructions). Non-hydrogen atoms were refined with anisotropic thermal parameters. Hydrogen atoms were generated in idealized positions, riding on the carrier atoms, with isotropic thermal parameters.

Table S1- 1: Crystallography data for **DBED-NMe$_2$**, **DBED-H**, **TEED-NMe$_2$**, **Me$_5$DIEN-NMe$_2$**, **Me$_6$TREN-NMe$_2$** and **TEED-H**.

| **Adduct name** | **DBED-NMe$_2$** | **DBED-H** | **TEED-NMe$_2$** | **Me$_5$DIEN-NMe$_2$** | **Me$_6$TREN-NMe$_2$** | **TEED-H** | |
|---|---|---|---|---|---|---|---|
| Compound | [DBEDCu$^{NMe2}$ArNO](SbF$_6$) | [DBEDCu$^{H}$ArNO](SbF$_6$) | [TEEDCu$^{NMe2}$ArNO](SbF$_6$) | [Me$_5$DIENCu$^{NMe2}$ArNO](TfO) | [Me$_6$TRENCu$^{NMe2}$ArNO](TfO) | [TEEDCu($^{H}$ArNO)CuTEED](TfO)$_2$ | [DBEDCu(μ-DBDI)CuDBED](SbF$_6$)$_2$ |
| CCDC number | 1823004 | 1823005 | 1823006 | 1823007 | 1823008 | 1823009 | 1823010 |
| Chemical formula | $C_{18}H_{34}CuF_6N_4OSb\cdot C_4H_8O$ | $2(C_{16}H_{29}CuN_3O)\cdot 2(F_6Sb)$ | $C_{18}H_{34}CuN_4O\cdot F_6Sb$ | $C_{17}H_{33}CuN_5O\cdot CF_3O_3S$ | $C_{20}H_{40}CuN_6O\cdot CF_3O_3S$ | $C_{27}H_{53}Cu_2F_3N_5O_4S\cdot CF_3O_3S$ | $C_{30}H_{68}Cu_2N_6\cdot 2(F_6Sb)\cdot C_4H_8O$ |
| $M_r$ | 693.88 | 1157.42 | 621.78 | 536.09 | 593.19 | 876.95 | 1183.58 |
| Crystal system, space group | Monoclinic, $P2_1/n$ | Triclinic, *P1* | Monoclinic, $P2_1/c$ | Monoclinic, $P2_1/c$ | Monoclinic, $P2_1/n$ | Monoclinic, $P2_1/c$ | Monoclinic, $P2_1$ |
| Temperature (K) | 150 | 110 | 150 | 110 | 116 | 100 | 150 |
| *a* (Å) | 9.2011 (3) | 10.0469 (3) | 11.8998 (4) | 9.6745 (1) | 8.7738 (11) | 14.4829 (4) | 14.7346 (3) |
| *b* (Å) | 21.4308 (6) | 14.8274 (4) | 25.1515 (9) | 15.6108 (1) | 25.446 (3) | 14.6800 (3) | 10.1121 (2) |
| *c* (Å) | 14.8258 (4) | 15.8106 (4) | 8.3707 (3) | 16.0592 (1) | 12.7528 (15) | 18.7395 (5) | 17.0163 (4) |
| α(°) | | 108.077 (1) | | | | | |
| β (°) | 94.433 (1) | 90.643 (2) | 97.987 (3) | 98.085 (1) | 105.723 (7) | 107.688 (3) | 101.022 (1) |
| γ (°) | | 92.875 (1) | | | | | |
| *V* (Å$^3$) | 2914.71 (15) | 2235.33 (11) | 2481.03 (15) | 2401.26 (3) | 2740.7 (6) | 3795.83 (17) | 2488.62 (9) |
| *Z* | 4 | 2 | 4 | 4 | 4 | 4 | 2 |
| Radiation type | Cu *K*α | Cu *K*α | Cu *K*α | Cu *K*α | Cu *K*α | Cu *K*α | Cu *K*α |
| μ (mm$^{-1}$) | 8.82 | 11.32 | 10.25 | 2.61 | 2.35 | 3.10 | 10.15 |
| Crystal size (mm) | 0.31 × 0.17 × 0.12 | 0.20 × 0.15 × 0.05 | 0.32 × 0.15 × 0.14 | 0.16 × 0.14 × 0.08 | 0.34 × 0.18 × 0.06 | 0.14 × 0.09 × 0.07 | 0.36 × 0.06 × 0.06 |
| $T_{min}$, $T_{max}$ | 0.492, 0.753 | 0.356, 0.753 | 0.407, 0.753 | 0.667, 0.753 | 0.617, 0.753 | 0.880, 1 | 0.430, 0.753 |
| No. of measured, independent and observed [$I > 2\sigma(I)$] reflections | 43477, 5344, 4774 | 7984, 7984, 7434 | 36450, 4552, 4099 | 35778, 4408, 4063 | 37557, 4990, 4536 | 33632, 6625, 5038 | 34981, 8642, 8062 |
| $R_{int}$ | 0.071 | 0.044 | 0.095 | 0.029 | 0.039 | 0.054 | 0.049 |
| $(\sin\theta/\lambda)_{max}$ (Å$^{-1}$) | 0.603 | 0.603 | 0.603 | 0.603 | 0.602 | 0.595 | 0.604 |
| $R[F^2 > 2\sigma(F^2)]$ | 0.036 | 0.033 | 0.034 | 0.024 | 0.028 | 0.073 | 0.027 |
| $wR(F^2)$ | 0.095 | 0.073 | 0.085 | 0.064 | 0.074 | 0.207 | 0.055 |
| Goodness of of fit, *S* | 1.04 | 1.05 | 1.05 | 1.06 | 1.04 | 1.11 | 0.98 |
| No. of reflections, parameters, restraints | 5344, 333, 0 | 7984, 517, 0 | 4552, 286, 0 | 4408, 296, 0 | 4990, 333, 0 | 6625, 470, 0 | 8642, 549, 1 |
| $\Delta\rho_{max}$, $\Delta\rho_{min}$ (e Å$^{-3}$) | 1.09, −0.82 | 1.26, −0.74 | 0.69, −1.52 | 0.29, −0.30 | 0.34, −0.29 | 2.59, −1.12 | 0.40, −0.59 |
| Absolute structure Flack | | | | | | | Refined as an inversion twin 0.010 (5) |

| parameter | | | | | | | |
|---|---|---|---|---|---|---|---|
| **Selected metrical parameters** | | | | | | | |
| N–O (Å) | 1.269 | 1.236 | 1.254 | 1.266 | 1.260 | 1.322 | |
| Cu–$N_{nitroso}$ (Å) | 1.867 | 1.827-1.828 | 1.872 | 1.896 | 1.934 | 2.036 ($Cu^{II}$), 1.885 ($Cu^{I}$) | |
| Cu–$O_{nitroso}$ (Å) | | | | | | 1.880 ($Cu^{II}$), 2.666 ($Cu^{I}$) | |
| Cu–OTf (Å) | | | | | | 2.266 ($Cu^{II}$), 2.630 ($Cu^{I}$) | |
| Cu–$N_{ligand}$ (Å) | 2.039-2.074 | 2.004-2.009 | 2.050-2.058 | 2.063-2.205 | 2.095-2.250 | 2.017-2.019 ($Cu^{II}$) 2.048-2.130 ($Cu^{I}$) | 2.047-2.064 to DBED 1.903-1.904 to DBDI |

## DFT details

The theoretical electronic spectra of the analogous *para*-substituted arylnitroso complexes **DBED-Z** and (Z = $NMe_2$, Br, H, $NO_2$) were predicted using TD-DFT calculations. All calculations were performed on Gaussian 09[1] using the GGA pure DFT functional BP86 with the triple-zeta polarized Ahlrich basis set Def2TZVP. Geometry optimizations were carried out from x-ray crystal structures using the ultrafine integration grid, tight SCF convergence criteria, and Polarized Continuum Model (PCM) solvent corrections for tetrahydrofuran (ε = 7.6), which was the solvent used to record the compounds' experimental UV-Vis spectra. Using the geometries optimized under implicit solvation, 40 singlet excited states were calculated for each compound using TD-DFT at the same level of theory. Theoretical fits of the UV-Vis spectra were plotted based on the 40 calculated excited states, and Electron Density Difference (EDD) plots were generated for each transition associated with the most intense predicted excited state in the visible range, not including de-excitations or excitations with small or negative CI expansion coefficients. A sample input section for each type of calculation is provided below:

Geometry Optimization:

```
# bp86/Def2TZVP opt nosymm int=grid=ultrafine scf=tight
scrf=(solvent=tetrahydrofuran)
geometry optimization with implicit solvation
1 1
```

Excited State Calculation:

```
# td=(nstates=40) bp86/def2TZVP nosymm int=grid=ultrafine scf=tight
geom=check
TDDFT without scrf=solvent=thf
1 1
```

## DBED-NMe$_2$

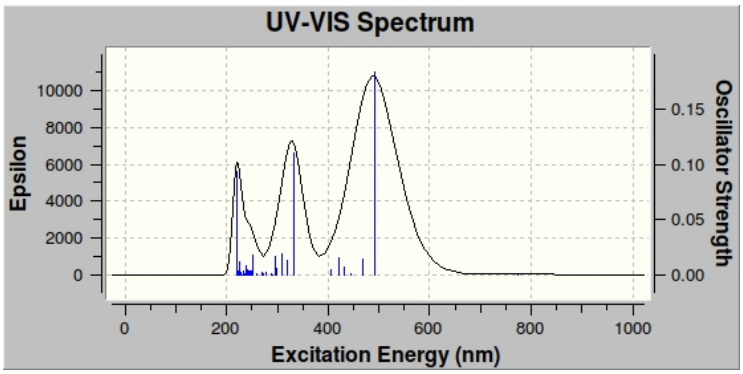


Figure S1- 10: Calculated UV-vis spectrum for **DBED-NMe$_2$**.

Table S1- 2: Transitions involved in the 507.61 nm peak (excited state #2) for **DBED-NMe$_2$**.

| Transition | Orbitals Involved | CI expansion Coefficient | Assignment |
|---|---|---|---|
| 101 → 104 | HOMO-2 → LUMO | 0.12349 | MLCT |
| **102 → 104** | **HOMO-1 → LUMO** | **0.68949** | **MLCT** |
| 102 ← 104 | HOMO-1 ← LUMO | -0.12183 | |

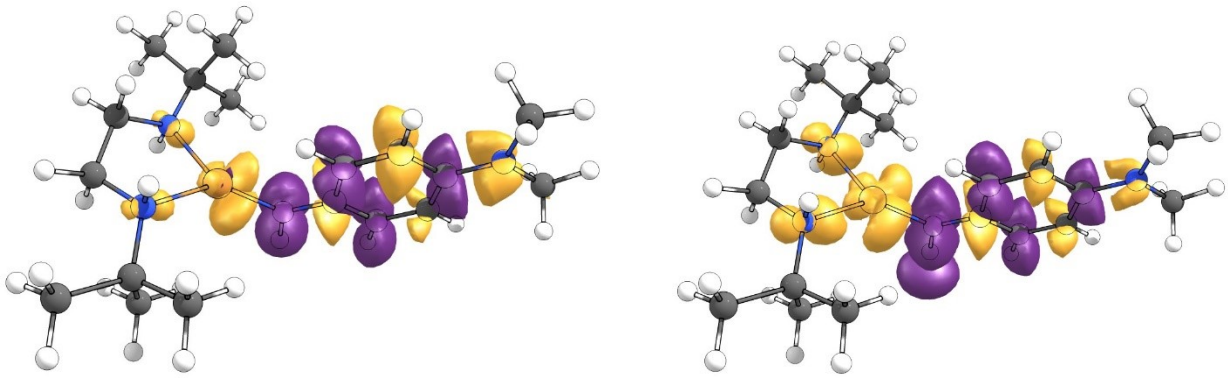

Figure S1- 11: EDD plot of absolute value of 104-101 (left) and 140-102 (right) for **DBED-NMe$_2$**. Purple = (+), yellow = (-).

## DBED-H

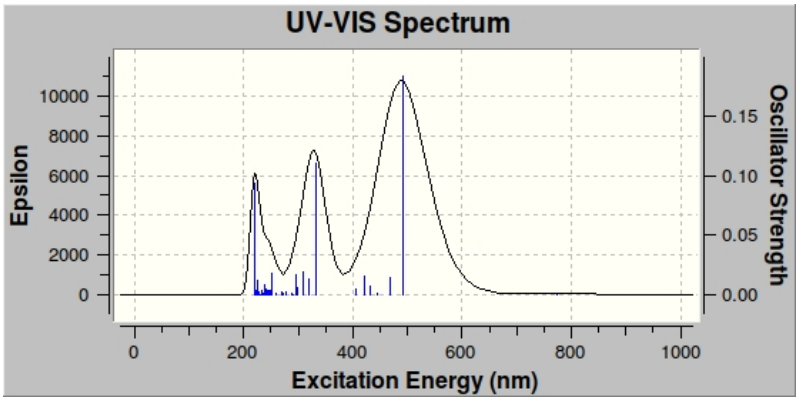


Figure S1- 12: Calculated UV-vis spectrum for **DBED-H**.

Table S1- 3: Transitions involved in the 491.31 nm peak (excited state #2) for **DBED-H**.

| Transition | Orbitals Involved | CI expansion Coefficient | Assignment |
|---|---|---|---|
| 83 → 92 | HOMO-8 → LUMO | 0.11167 | |
| 85 → 92 | HOMO-6 → LUMO | 0.10364 | |
| 89 → 92 | HOMO-2 → LUMO | -0.15051 | |
| **90 → 92** | **HOMO-1 → LUMO** | **0.67080** | **MLCT** |
| 90 ← 92 | HOMO-1 ← LUMO | -0.13135 | |

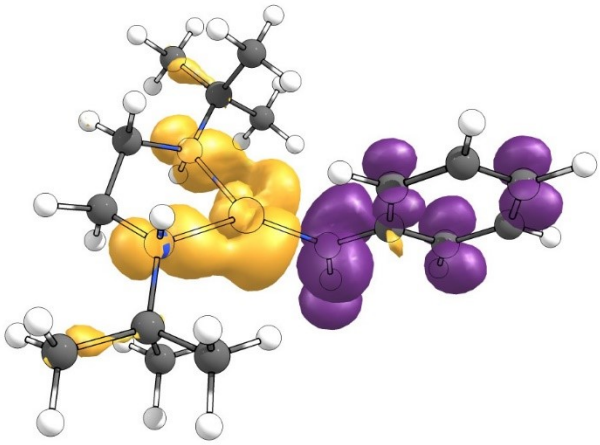

Figure S1- 13: EDD plot of absolute value of 92-90 for **DBED-H**. Purple = (+), yellow = (-).

## DBED-Br

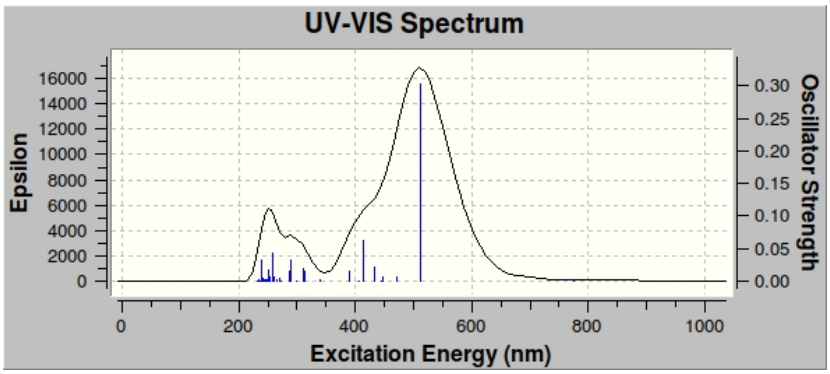


Figure S1- 14: Calculated UV-vis spectrum for **DBED-Br**.

Table S1- 4: Transitions involved in the 512.53 nm peak (excited state #2) for **DBED-Br**.

| Transition | Orbitals Involved | CI expansion Coefficient | Assignment |
|---|---|---|---|
| 106 → 109 | HOMO-2 → LUMO | 0.15535 | LMCT |
| **107 → 109** | **HOMO-1 → LUMO** | **0.67634** | **MLCT** |
| 107 ← 109 | HOMO-1 ← LUMO | -0.12520 | |

Interestingly, **DBED-Br** is an exception to the MLCT assignment, compared with the other species. Its most intense visible excited state includes important contribution from both MLCT and LMCT component transitions, with the second most important contributor identified by EDD plots as an LMCT from HOMO-2 → LUMO (see below).

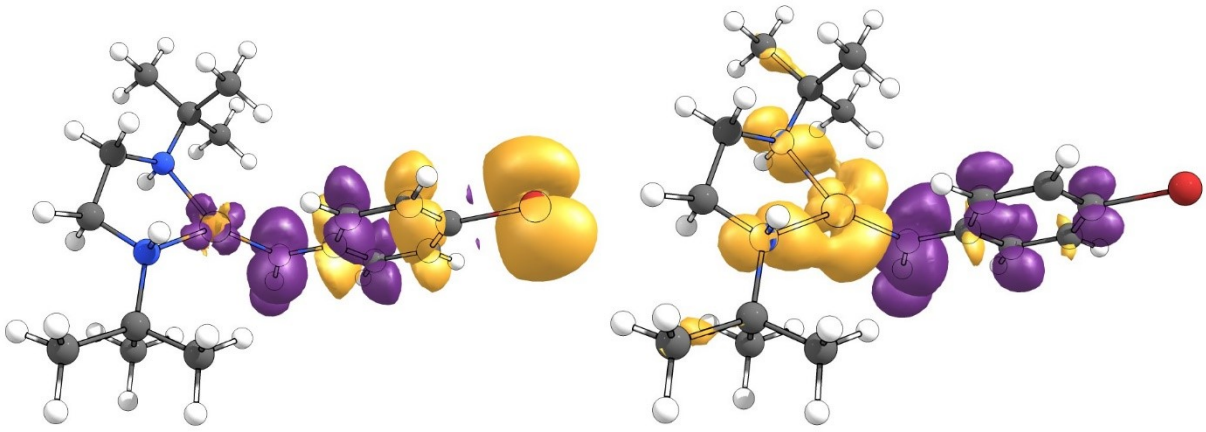

Figure S1- 15: EDD plot of absolute value of 109-106 (left) and 109-107 for **DBED-Br** (right). Purple = (+), yellow = (-).

## DBED-$NO_2$

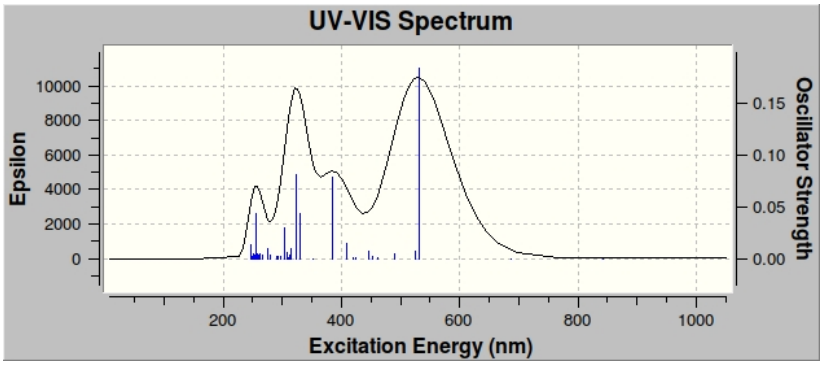


Figure S1- 16: Calculated UV-vis spectrum for **DBED-$NO_2$**.

Table S1- 5: Transitions involved in the 531.58 nm peak (excited state #2) for **DBED-$NO_2$**.

| Transition | Orbitals Involved | CI expansion Coefficient | Assignment |
|---|---|---|---|
| 99 → 103 | HOMO-3 → LUMO | -0.11235 | |
| **101 → 103** | **HOMO-1 → LUMO** | **0.66326** | **MLCT** |
| 101 → 104 | HOMO-1 → LUMO+1 | 0.17260 | MLCT |
| 101 ← 103 | HOMO-1 ← LUMO | -0.13253 | |

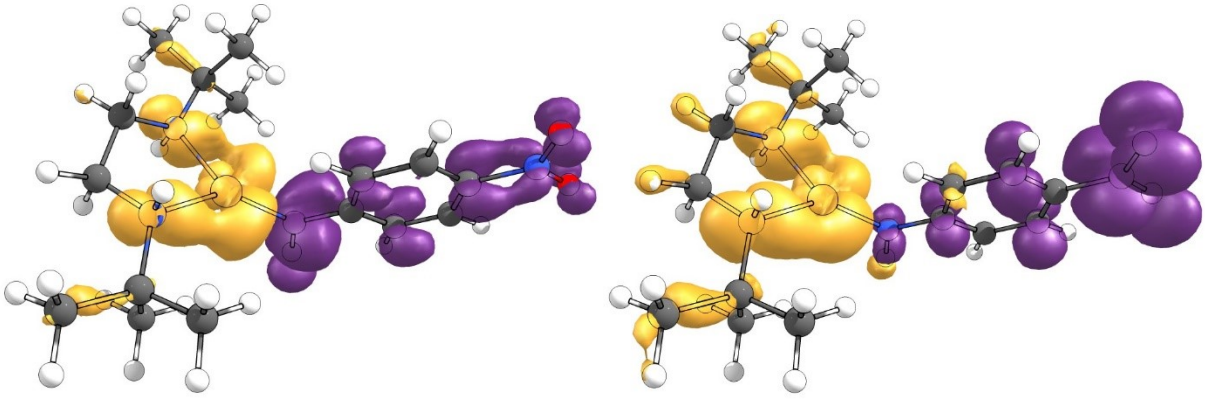

Figure S1- 17: EDD plot of absolute value of 103-101 (left) and 104-101 (right) for **DBED-$NO_2$**. Purple = (+), yellow = (-).

# Appendix 2 - Supplemental Information for Chapter 3

## A Stable Copper-Arylhydroxylamine Complex and its Conversion to a Hemilabile Arylnitroso

### Experimental Procedures

### General Information

**Materials**: Organics reagents and metal salts were obtained from commercial sources and used as received unless indicated otherwise. Inhibitor-free solvents were degassed, dried over a MBraun SPS 800 solvent purification system, and then stored over activated 4 Å molecular sieves inside an inert-atmosphere glovebox filled with a dry nitrogen atmosphere (MBraun Labmaster, <1 ppm of $O_2$ and H2O, filled with a dry $N_2$ atmosphere).

**Characterization**: $^{1}$H and $^{13}$C-NMR spectra were recorded on a Varian VNMRS 500 MHz or Inova 300 MHz and referenced to internal tetramethylsilane, using samples in a 5 mm air-tight tube prepared under a N2 atmosphere. Various temperature measurements were performed on Varian VNMRS 500 MHz. UV-visible spectra were recorded on a B&W Tek iTrometer equipped with fiber optic cables. Mass spectrometry data for samples were obtained by direct injection of their acetonitrile solutions into a Micromass Quattro LC triple-quad instrument equipped with an electrospray ionization (ESI) chamber.

**X-Ray Crystallography**: Crystallographic analysis was performed using the Mo Kα or microfocus Cu Kα source of a Bruker APEX-DUO or APEX-II diffractometer. The frames were integrated with the Bruker SAINT software package using a narrow-frame algorithm. Data were corrected for absorption effects using the multi-scan method (SADABS). The structures were solved by ShelXT and refined using the Bruker APEX3 software package (SHELXL instructions). All non-hydrogen atoms were refined with anisotropic thermal parameters. H atoms were generated in idealized positions, riding on the carrier atoms with isotropic thermal parameters. Further details in the CIFs.

## Synthesis of ligand $L^{NO2}$

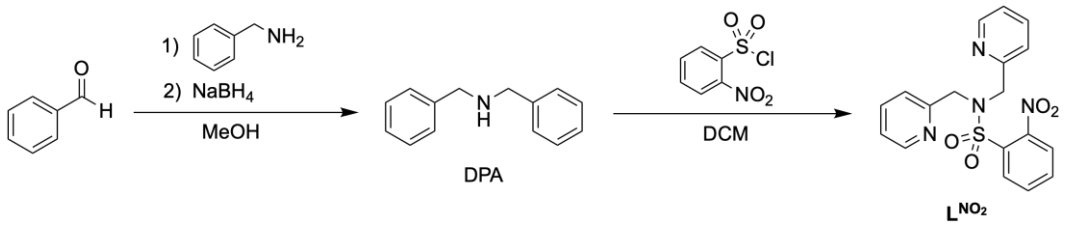


Scheme S2- 1: Synthesis of 2-nitro-N,N-bis(2-pyridinylmethyl)benzenesulfonamide ($\mathbf{L^{NO2}}$).

## Reduction of $L^{NO2}$

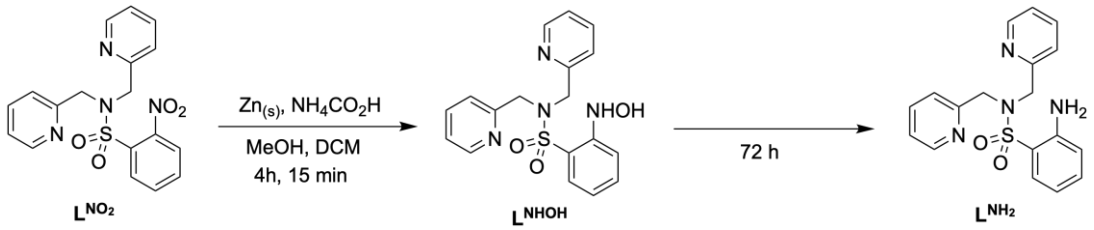


Scheme S2- 2: Reduction of $\mathbf{L^{NO2}}$ to 2-hydroxylamine-*N,N*-bis(2-pyridinylmethyl)benzenesulfonamide ($\mathbf{L^{NHOH}}$) or 2-amine-*N,N*-bis(2-pyridinylmethyl)benzenesulfonamide ($\mathbf{L^{NH2}}$).

Reduction of $\mathbf{L^{NO2}}$ can be carried out by heterogeneous activated zinc-catalyzed transfer hydrogenation from $NH_4CO_2H$ using fine $Zn_{(s)}$ dust activated by stirring for 2h in 2M HCl. The thermodynamic product of this reaction is the amine $\mathbf{L^{NH2}}$, but the hydroxylamine $\mathbf{L^{NHOH}}$ is an intermediate and can be isolated by early quenching of the reaction. Due to the heterogeneous nature of the reaction, the precise time at which the reaction mixture contains purely $\mathbf{L^{NHOH}}$ is dependent on the grade and activation of the zinc powder, the flask, and the rate of agitation, therefore isolation of pure $\mathbf{L^{NHOH}}$ requires careful monitoring. Both TLC and $^1$H NMR were used for this purpose. A comparison of the methylene peaks of $\mathbf{L^{NO2}}$ ($CDCl_3$, 500 MHz, $\delta$ 4.75), $\mathbf{L^{NHOH}}$ ($CDCl_3$, 500 MHz, $\delta$ 4.59), and $\mathbf{L^{NH2}}$ ($CDCl_3$, 500 MHz, $\delta$ 4.64) is shown in Figure S2- 1.

$\mathbf{L^{NHOH}}$: A solution of 28.0 mg of $NH_4CO_2H$ (0.438 mmol, 6 eq.) was dissolved in 3 mL MeOH and added to a solution of 104.9 mg $L^SNO_2$ (0.273 mmol, 1.6 eq.) in 4 mL DCM, stirred at 600 rpm in a teardrop-shaped 25 mL boiling flask. The mixture was cooled to 0˚C in an ice-water bath and 35.5 mg (0.546 mmol, 2 eq.) of activated $Zn_{(s)}$ was added. For the first 90 minutes of the reaction, 6 further 9mg (0.5 eq.) aliquots of activated $Zn_{(s)}$ were added every 15 minutes. After 90 minutes, the reaction was closely monitored by TLC and $^1$H NMR. Complete consumption of the starting material was observed after 210 min. The

reaction should be quenched when complete consumption of $L^SNO_2$ is observed, but before the formation of any $L^SNH_2$ begins to occur. This was noted at after 255 min and the reaction was immediately filtered over Celite. The filtrate was then washed twice with 15 mL 0.5 M EDTA, followed by distilled water and brine. The organic layer was then dried over $MgSO_4$, concentrated under reduced pressure, and dried under high-vacuum, yielding the product as a yellow-orange oil. The product was stored under vacuum or inert gas. TLC: (stationary phase: $SiO_2$, mobile phase: DCM:$Et_3N$:hexanes = 5:3:2) $R_f$ (**$L^{NO2}$**) = 0.60m, $R_f$ (**$L^{NHOH}$**) = 0.85, $R_f$ (**$L^{NH2}$**) = 0.63. $^1$H NMR: ($CDCl_3$, 500 MHz): $\delta$ 8.90-9.50 (b, 1H, OH), 8.39 (d, 1H, $H_{Py}$), 7.79 (d, 1H, $H_{Ar}$), 7.70 (b, 1H, NH), 7.42-7.52 (m, 4H, $2H_{Py}$ & $2H_{Ar}$), 7.23 (d, 2H, $H_{Py}$), 7.06 (m, 2H, $H_{Py}$), 6.87 (t, 1H, $H_{Ar}$), 4.59 (s, 4H, $H_{CH_2}$). HRMS m/z (MeOH, $ESI^+$) calcd for $[C_{18}H_{18}N_4O_3S]H^+$ 371.12, found 371.3 (100%), calculated for $[C_{18}H_{18}N_4O_3S]Na^+$ 393.10, found 393.2 (15%).

**$L^{NH2}$**: As shown in Scheme S2- 2, reduction of **$L^{NO2}$** by heterogeneous activated zinc-catalyzed transfer hydrogenation from $NH_4CO_2H$ affords can be used to produce both **$L^{NHOH}$** and **$L^{NH2}$**. The reaction yields the hydroxylamine at short reaction times, but total conversion to the amine is eventually observed at very long reaction times, however the yield is reduced. 126.1 mg $NH_4CO_2H$ (2 mmol, 2 eq.) was dissolved in 1.5 mL MeOH and added to a stirred solution of 384.4 mg **$L^{NO2}$** (1 mmol, 1 eq) in 1.5 mL DCM. To this mixture was added 130.8 mg of activated $Zn_{(s)}$ (2 mmol, 2 eq.). At 15-20-minute intervals during the first 150 minutes of the reaction, 8 further 0.5 eq. aliquots of activated $Zn_{(s)}$ (32.7 mg, 0.5 mmol, 0.5 eq.) were added to the reaction mixture. Additionally, 3 further 0.5 eq. aliquots of $NH_4CO_2H$ were added to the reaction mixture at 30-minute intervals during the first 90 minutes of the reaction. Total consumption of **$L^{NO2}$** was observed by TLC after 255 minutes, but the main product was **$L^{NHOH}$** at this point. The mixture was left stirring at RT for 72 h, at which point only **$L^{NH2}$** was observed by TLC. The reaction mixture was then filtered over Celite. The filtrate was then washed twice with 15 mL 0.5 M EDTA, followed by distilled water and brine. The organic layer was then dried over $MgSO_4$, concentrated under reduced pressure, and dried under high-vacuum, yielding the product was a thick brown oil in 45% yield. TLC: (stationary phase: $SiO_2$, mobile phase: DCM:$Et_3N$:hexanes = 5:3:2) $R_f$ ($L^SNO_2$)= 0.60m, $R_f$ ($L^SNHOH$) = 0.85, $R_f$ ($L^SNH_2$) = 0.63. $^1$H NMR: ($CDCl_3$, 500 MHz): $\delta$ 8.40 (qd, 2H, $H_{Py}$), 7.67-7.71 (dd, 1H, $H_{Ar}$), 7.49-7.56 (dt, 2H, $H_{Ar}$), 7.25-7.30 (m, 3H, $1H_{Ar}$ & $2H_{Py}$), 7.05-7.10 (qd, 2H, $H_{Py}$), 6.70-6.73 (m, 2H, $H_{Py}$), 4.90-5.40 (b, 2H, $_{NH2}$), 4.64 (s, 4H, $H_{CH2}$). HRMS m/z (MeOH, $ESI^+$) calculated for $[C_{18}H_{18}N_4O_2S]H^+$ 355.12, found 355.1 (100%).

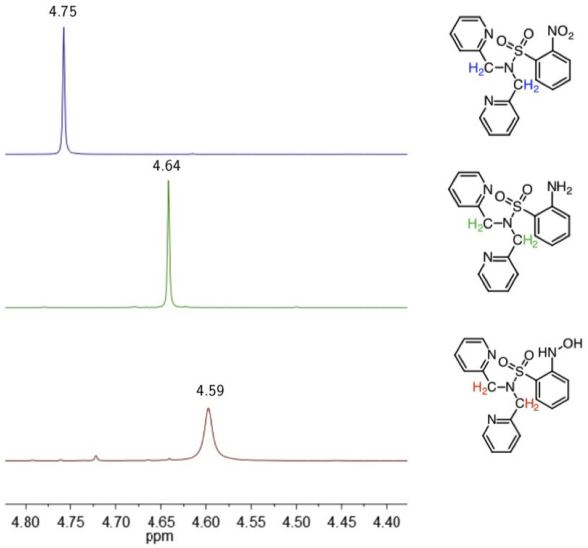


Figure S2- 1: Diagnostic peaks for monitoring of reduction of **L$^{NO2}$** to **L$^{NHOH}$** by $^{1}$H NMR.

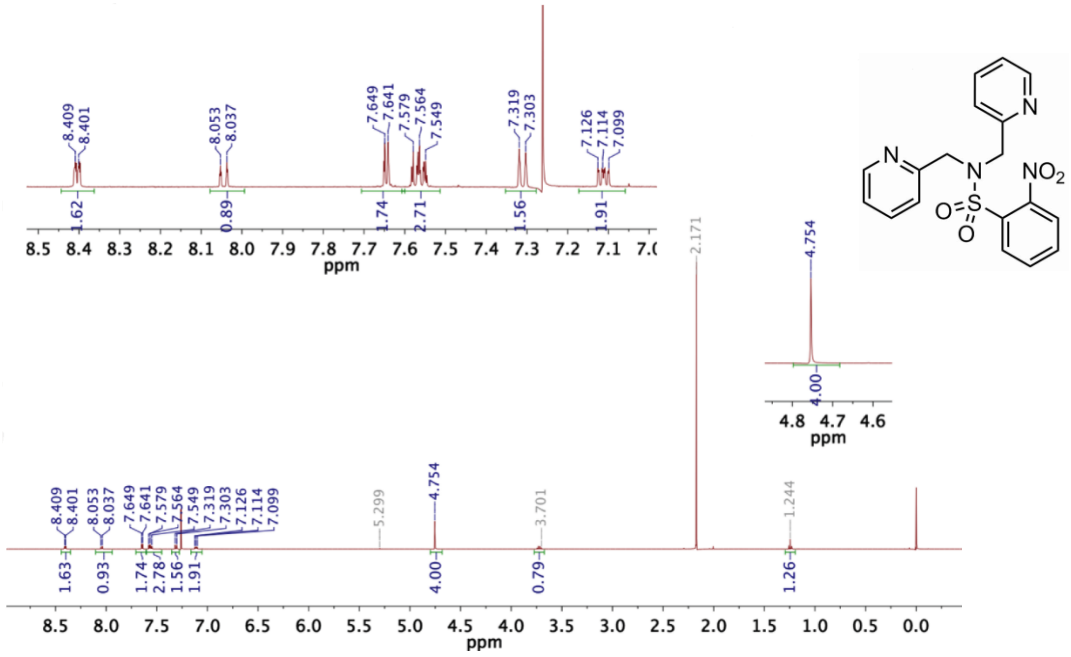


Figure S2- 2: 500 MHz $^{1}$H NMR of **L$^{NO2}$** in $CDCl_3$, insets showing aromatic region and methylene.

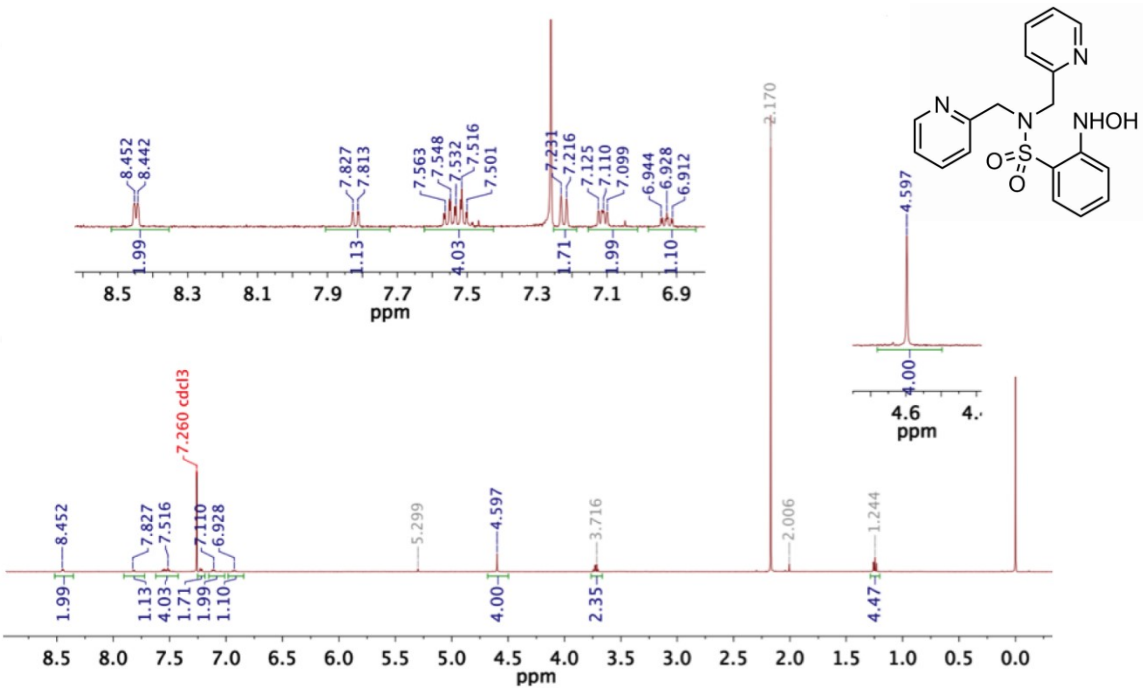


Figure S2- 3: 500 MHz $^{1}$H NMR of **L$^{NHOH}$** in $CDCl_3$, insets showing aromatic region and methylene.

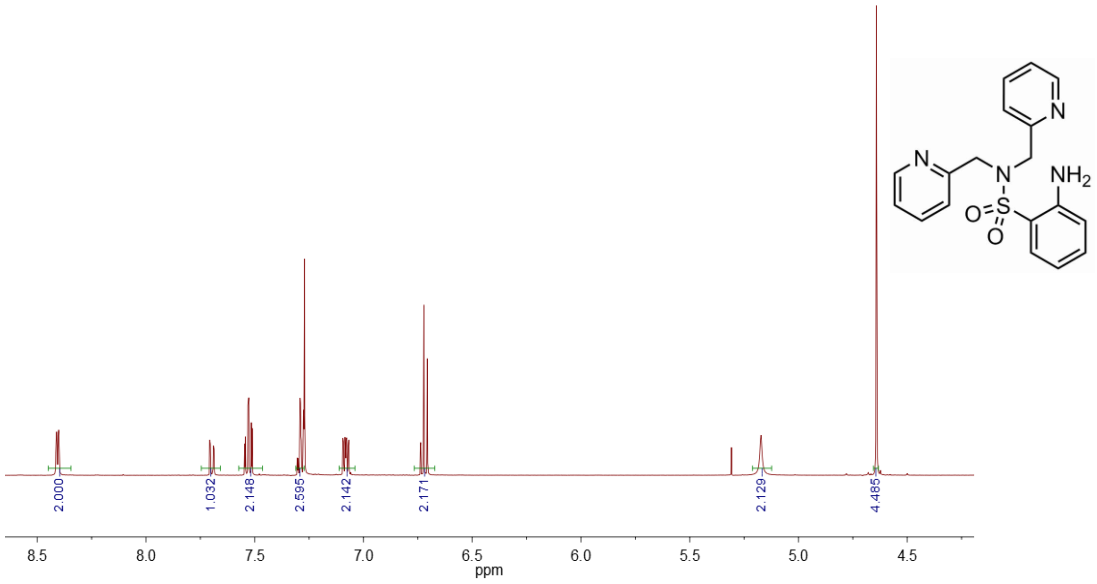


Figure S2- 4: 500 MHz $^{1}$H NMR of **L$^{NH2}$** in $CDCl_3$, insets showing aromatic region and methylene.

## Complexation of $L^{NHOH}$ with $[Cu^{I}(CH_3CN)_4]+$

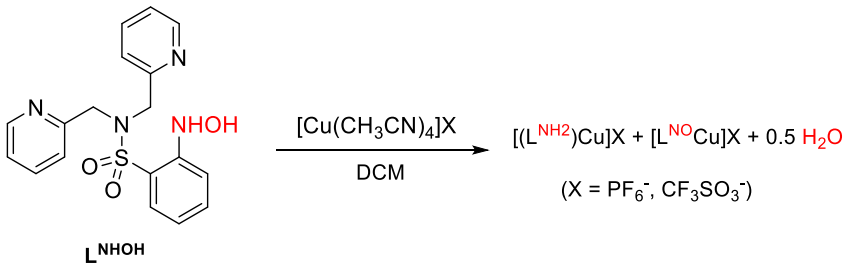


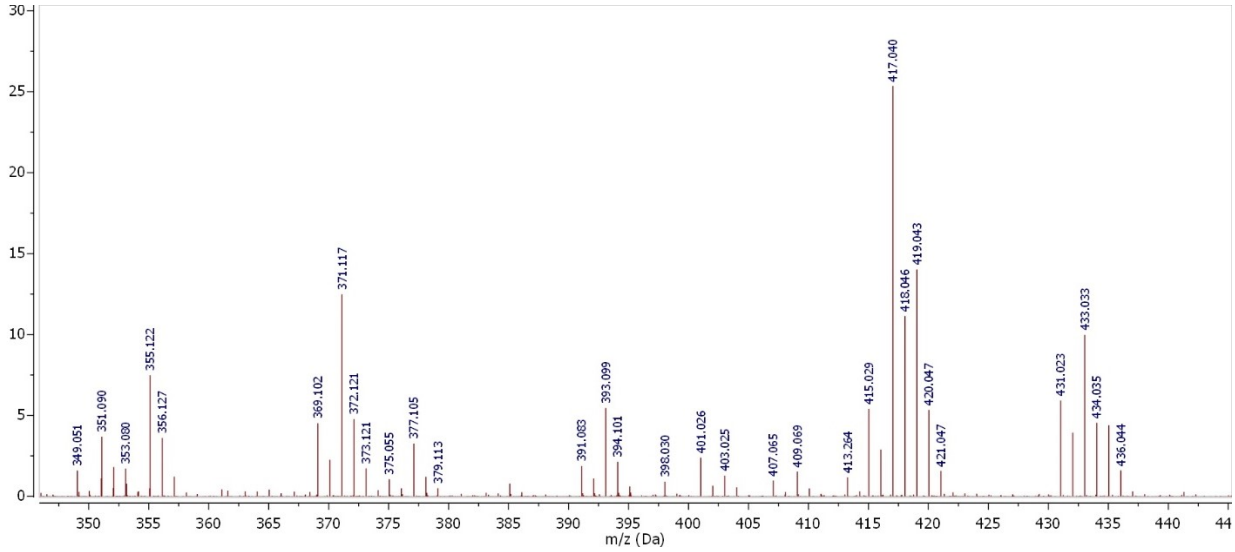


Figure S2- 5: ESI-MS positive mode data for $L^{NHOH}$ + 1 equiv. of $[Cu^{I}(CH_3CN)_4](CF_3SO_3)$ reacted in HPLC grade DCM and diluted in HPLC grade MeCN. The peak at 431.1 corresponds to $[\mathbf{L^{NO}Cu}]^+$; 417.01 to $[\mathbf{L^{NH2}Cu}]^+$, the peaks at 369.1 and 391.1 corresponds to $[\mathbf{L^{NO}}]H^+$ and $[\mathbf{L^{NO}}]Na^+$, 355.1 and 377.1 corresponds to $[\mathbf{L^{NH2}}]H^+$ and $[\mathbf{L^{NH2}}]Na^+$.

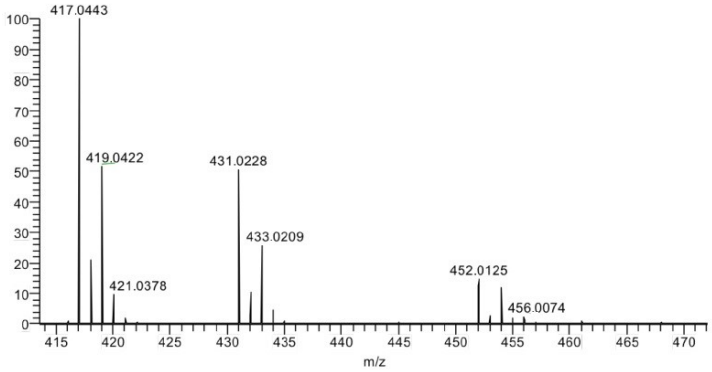


Figure S2- 6: ESI-MS positive mode data for $L^{NHOH}$ + 1 equiv. of $[Cu^{I}(CH_3CN)_4](PF_6)$ reacted in HPLC grade DCM and diluted in HPLC grade MeCN. The peak at 431.02 corresponds to $[\mathbf{L^{NO}Cu}]^+$; 417.04 to $[\mathbf{L^{NH2}Cu}]^+$.

## Synthesis and characterization of [($L^{NHOH}$)CuCl] (1)

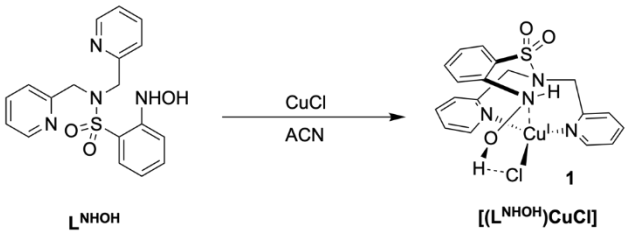


Scheme S2- 3: Synthesis of [($L^{NHOH}$)CuCl] (**1**) from $L^{NHOH}$.

[($L^{NHOH}$)CuCl]: In the $N_2$ glovebox, a stock solution of $\mathbf{L^{NHOH}}$ was prepared by dissolution of a 60.1 mg sample of $\mathbf{L^{NHOH}}$ in 1000 µL dry ACN. 10.0 mg CuCl (0.101 mmol) was suspended in 340 µL dry ACN and stirred. A 540 µL of the $\mathbf{L^{NHOH}}$ stock solution (0.101 mmol, 1 eq.) was added to the suspension, leading to immediate formation of a bright yellow precipitate. The mixture was allowed to stir for another 5 min and then diethyl ether was added dropwise to the reaction mixture until it lost its yellow colour, after which the reaction mixture was transferred to a -20 ˚C freezer for 5 minutes and then filtered over a fritted funnel. The resulting bright yellow powder was then washed liberally with pentane and collected (75%). $^1$H NMR: ($CD_3CN$, 500 MHz, assigned with COSY): δ 8.60-8.61 (d, 2H, $H_{Py}$), 8.49 (s, br. 1H, $OH_{NHOH}$ ), 8.04 (s, br. 1H, $NH_{NHOH}$), 7.67-7.71 (t, 2H, $H_{Py}$), 7.60-7.61 (d, 1H, $H_{Ar}$), 7.38-7.43 (t, 1H, $H_{Ar}$), 7.21-7.25 (m, 4H, $H_{Py}$), 6.81-6.84 (t, 1H, $H_{Ar}$), 4.55 (s, 4H, $H_{CH2}$) see Figure S2- 7.

Crystallization of [($L^{NHOH}$)CuCl]: Crystals of **1** can be grown slow vapour diffusion of pentane into a DCM solution of **1** at RT, however, these this procedure yields extremely thin needles, which single crystalline, but from which it is difficult to obtain a good dataset. Alternatively, crystals of **1** can be formed by addition of a solution of $\mathbf{L^{NHOH}}$ in ACN directly to $CuCl_{(s)}$, followed by brief stirring (10 s) and immediate transfer to the -20˚C freezer. This procedure led to formation of X-ray crystals in the form of bright yellow needles after 24 hours.

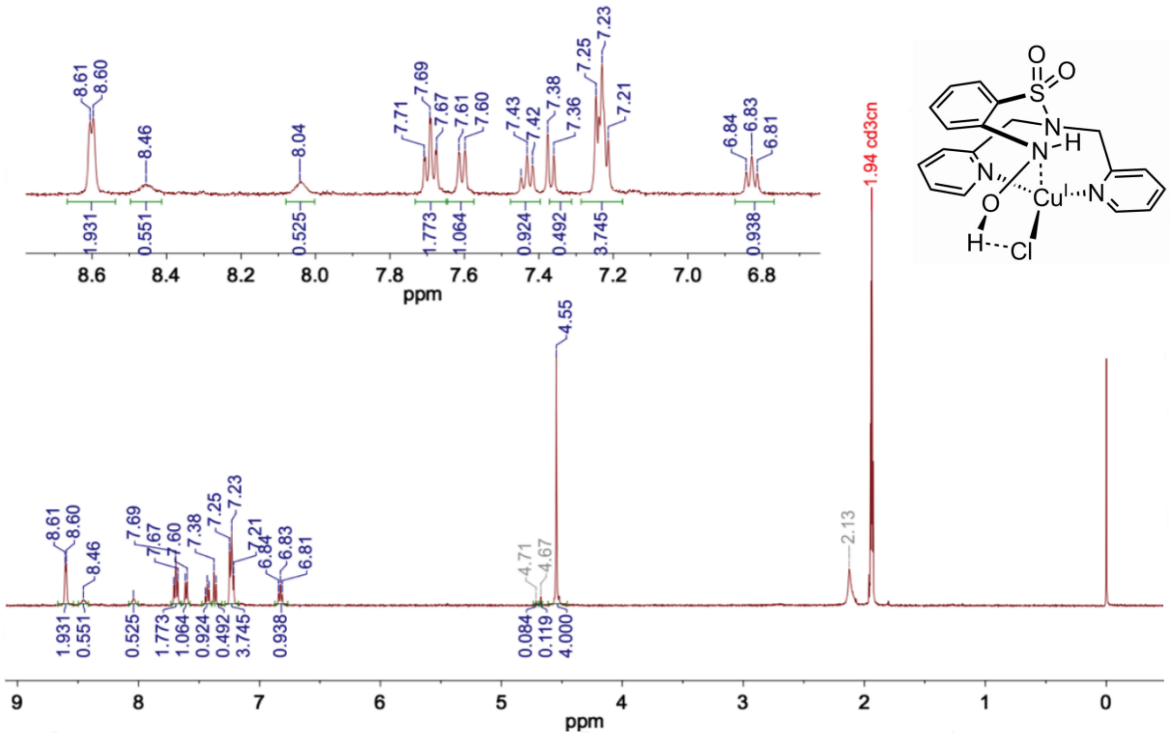


Figure S2- 7: 500 MHz $^{1}$H NMR of **1** in $CD_3CN$, inset showing zoom of aromatic region.

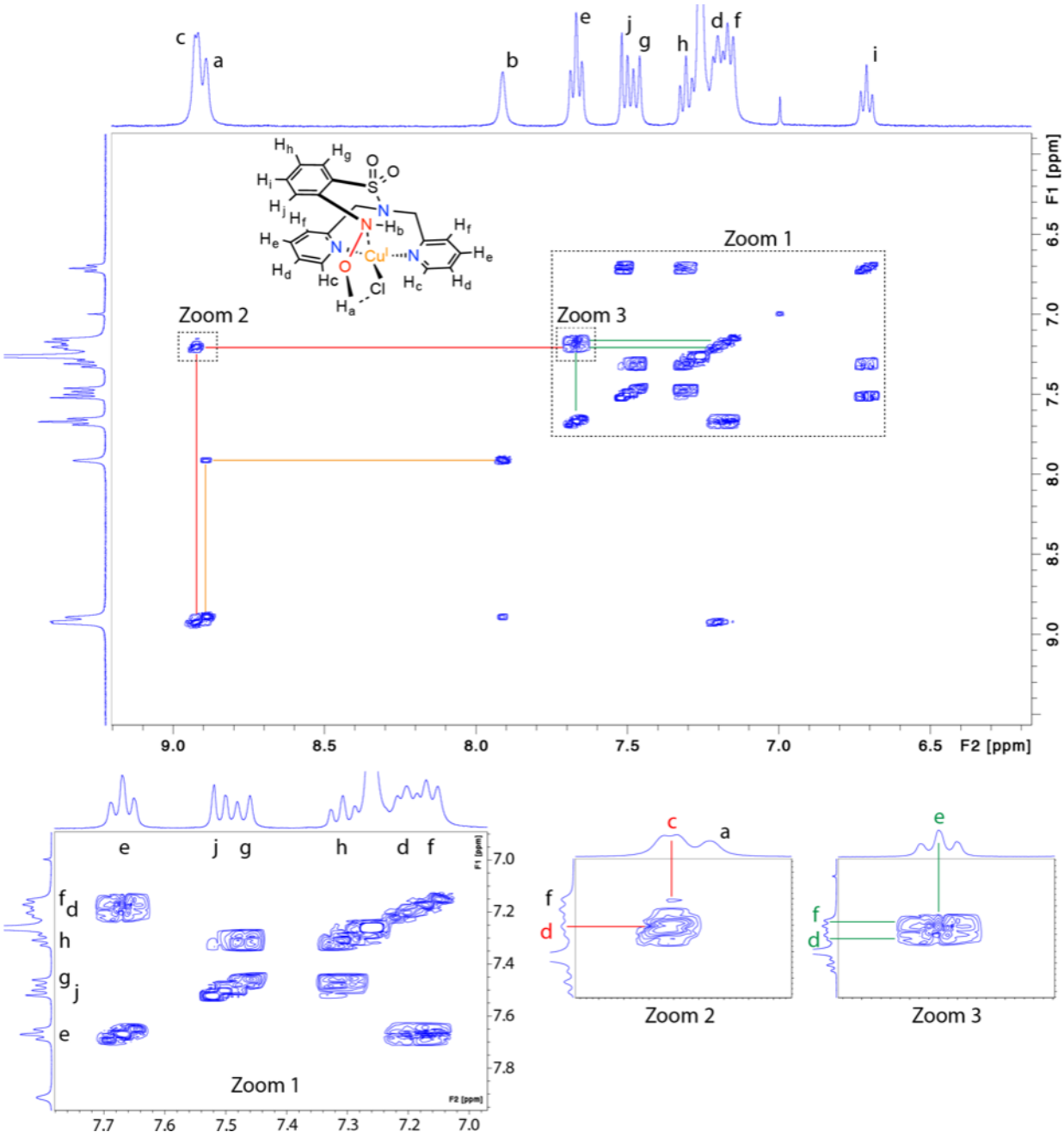


Figure S2- 8: $^{1}$H-NMR COSY experiment for **1**, $CDCl_3$, 25 °C, showing the magnetic coupling topology.

## Synthesis and characterization of $[(L^{NH2})CuCl]_2$ and $[(L^{NO2})CuCl]$

For comparison with **1**, we also investigated the structure of the $Cu^{I}Cl$ complexes of the reduced or oxidized forms of the ligand, $L^{NH2}$ and $L^{NO2}$, therefore the complexations shown in Scheme S2- 4 were carried out and their products were crystallized for x-ray diffraction analysis.

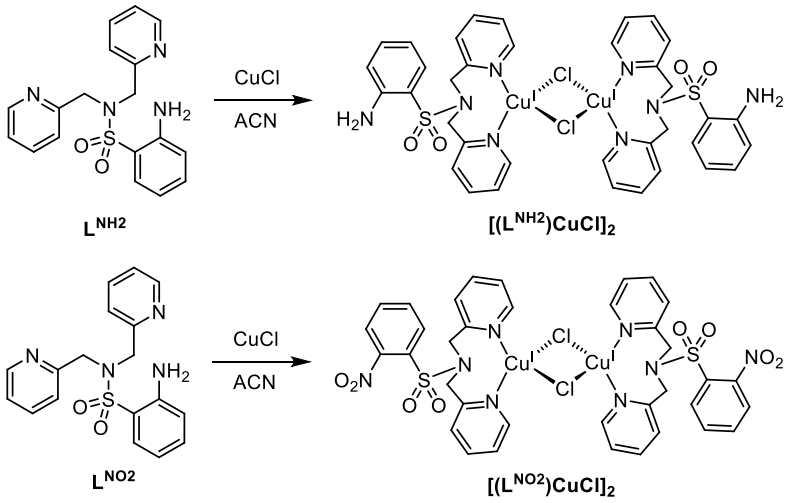


Scheme S2- 4: Synthesis of **$[(L^{NH2})CuCl]_2$** from **$L^{NH2}$** (top) and of **$[(L^{NO2})CuCl]_2$** from **$L^{NO2}$** (bottom).

**$[(L^{NH2})CuCl]$**: In the $N_2$ glovebox, 10.0 mg **$L^{NH2}$** dissolved in 2.0 mL ACN was slowly added to a slurry of 2.8 mg (0.028 mmol, 1 eq.) $Cu^{I}Cl$ in a few drops of ACN, yielding a light green solution. The solution was layered with $Et_2O$ followed by a few drops of pentane and transferred to the -20°C glovebox freezer. After 1 week, crystalline plates had grown. These crystals were used for X-ray diffraction analysis.

**$[(L^{NO2})CuCl]$**: In the $N_2$ glovebox, 9.4 mg **$L^{NO2}$** dissolved in 1.0 mL ACN was slowly added to a slurry of 2.4 mg (0.024 mmol, 1 eq.) $Cu^{I}Cl$ in a few drops of ACN, yielding a light yellow solution. The solution was layered with $Et_2O$ followed by a few drops of pentane and transferred to the -20°C glovebox freezer. After ca. 24 hours, polycrystalline urchins not suitable for x-ray diffraction had grown. These crystals were redissolved in 2 mL ACN and $Et_2O$ was added dropwise until the saturation. The saturated solution was then transferred to the -20°C glovebox freezer. After 1 week, large, high quality needles were observed. These crystals were used for X-ray diffraction analysis.

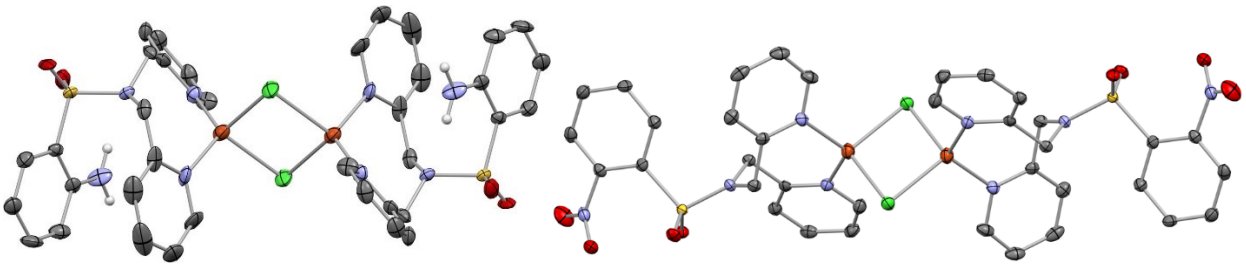

Figure S2- 9: ORTEP at 50% ellipsoid probability of **[(L$^{NH2}$)CuCl]$_2$** (left) and **[(L$^{NO2}$)CuCl]$_2$** (right). Crystallization solvents and hydrogen atoms were removed for clarity, except on the $NH_2$ groups.

## Oxidation of [(L$^{NHOH}$)CuCl] with DEAD/DIAD

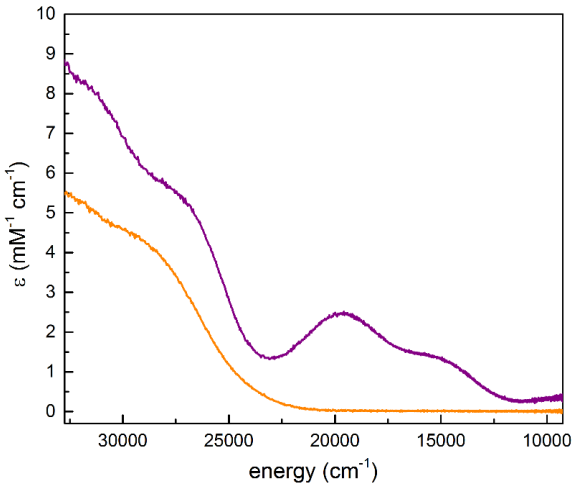


Figure S2- 10: Comparison of the UV-Vis spectra of **[(L$^{NHOH}$)CuCl]** (yellow) and **[(L$^{NO}$)CuCl]** (purple).

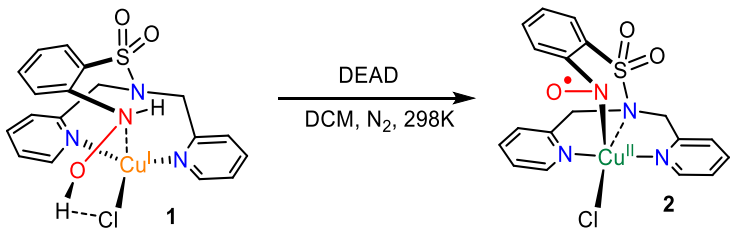

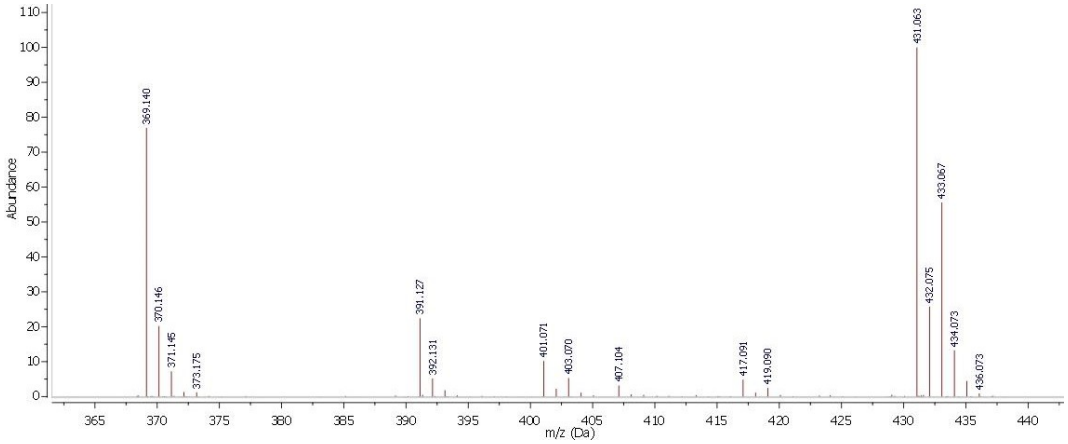


Figure S2- 11: ESI-MS positive mode data for $L^{NHOH}CuCl$ + 2eq. of DEAD in MeCN. The peak at 431.1 corresponds to $[\mathbf{L^{NO}Cu}]^+$; peaks at 391.1 and 369.1 correspond to $[\mathbf{L^{NO}}]Na^+$ and $[\mathbf{L^{NO}}]H^+$ , respectively.

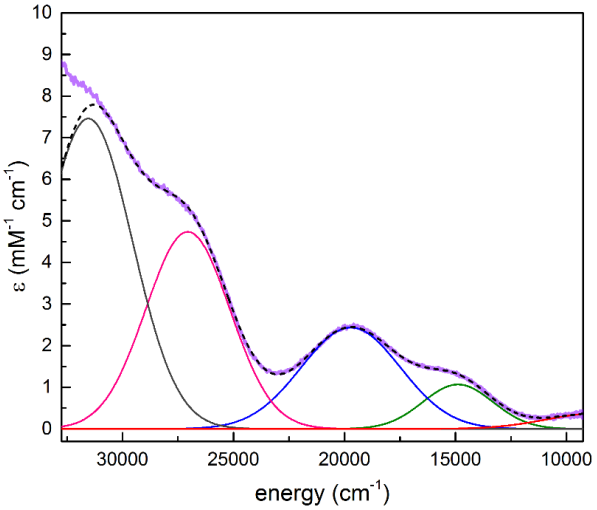


Figure S2- 12: A Gaussian deconvolution of the UV-Vis spectrum of **$[(L^{NO})CuCl]$** made by addition of 2 eq. of DEAD.

Table S2- 1: Fit parameters for Gaussian deconvolution shown above.

| Energy ($cm^{-1}$) | peak width at half-maximum ($cm^{-1}$) | Peak amplitude ($\varepsilon$ ($mM^{-1}\,cm^{-1}$)) |
|---|---|---|
| 8600 | 4660 | 0.38 |
| 14900 | 3160 | 1.1 |
| 19700 | 4470 | 2.4 |
| 27000 | 3800 | 4.7 |
| 31500 | 3970 | 7.4 |

## Mechanochemically-induced disproportionation of [($L^{NHOH}$)CuCl]

The mechanochemically-induced disproportionation of **$L^{NHOH}$CuCl** to amine and nitroso derivatives performed by adding 20 mg of microcrystalline sample of **$L^{NHOH}$CuCl** in small plastic jar with one zirconia ball inside the glovebox under nitrogen atmosphere. The jar then sealed and taken out and placed on vibratory ball miller and ground at 30 Hz for 15 minutes. After that the jar transferred inside back to the glovebox. The resulting fine purple powder has been dissolved in oxygen free anhydrous MeCN and directly injected to the ESI-QTOF Mass Spectrometer to analyze the products. The same transformation has been observed by taking the 1:1 mixture of **$L^{NHOH}$** and **CuCl** with total mass of 20 mg and grinding in the exact same condition. Both ways ended up giving the same MS profile which suggests the complexation and disproportionation transformation can happen in one pot under mechanical solid state grinding condition.

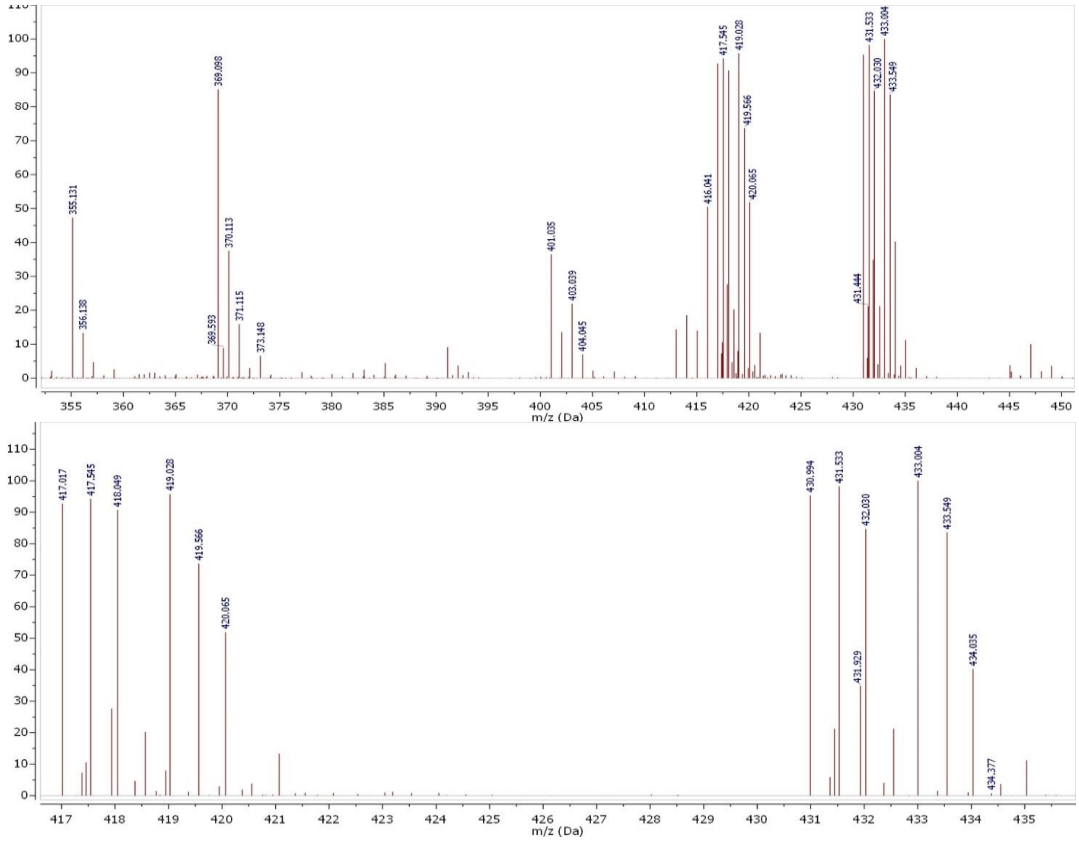


Figure S2- 13: ESI-MS data for **$L^{NHOH}$CuCl** + ground in plastic jar with zirconia ball under $N_2$ at 30 Hz for 15 minutes. The peak at 431.1 corresponds to [**$L^{NO}$Cu**]$^+$, 417.01 to [**$L^{NH2}$Cu**]$^+$, the peak at 369.1 corresponds to [**$L^{NO}$**]$H^+$ and 355.1 to [**$L^{NH2}$**]$H^+$.

## VT-NMR observation of heat-induced disproportionation

Since it was observed that mechanochemical grinding could initiate disproportionation of **1** to **2** + **[($L^{NH2}$)CuCl]** by mechanical force, it seems reasonable that input of simple thermal energy could initiate the same reaction. To test this, heating of **1** in solution was monitored by high temperature 400 MHz $^{1}H$ NMR. In the nitrogen glovebox, 3 mg of **1** was dissolved in 0.7 mL $CaH_2$-droed, degassed $CDCl_3$ and transferred to a sealed J-Young tube. An initial spectrum was measured at RT and then the sample was removed from the spectrometer, stored at RT, and replaced with a "dummy" sealed sample of neat DMSO. The probe temperature was then increased to 55 °C. Upon reaching 55 °C, the dummy sample was replaced with the experimental sample and the reaction timing was initiated. The coil was then re-tuned, re-matched, and re-shimmed, and then the initial HT NMR was taken after 7 min, 30s and new spectra were recorded roughly every 5 min for a total of 85 min.

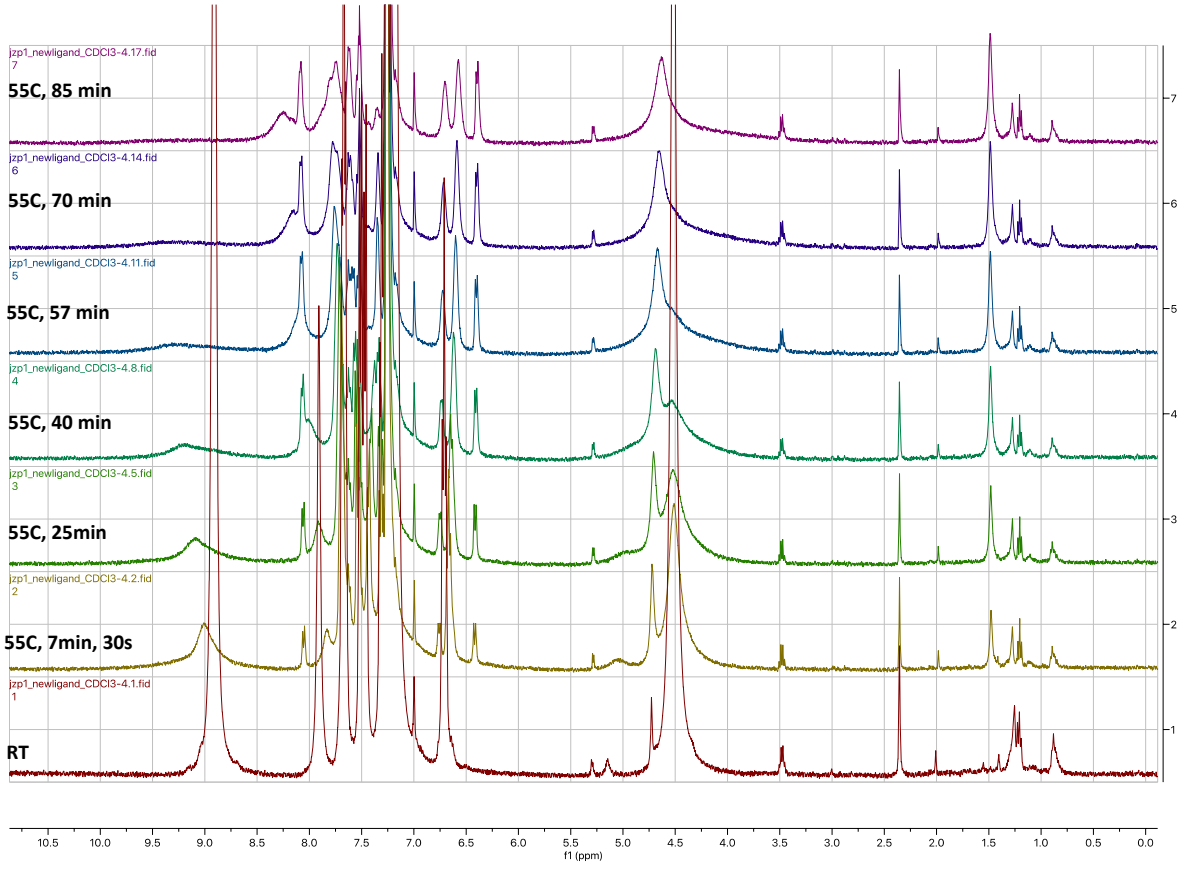


Figure S2- 14: VT-1H-NMR of **1** in $CDCl_3$, showing the initial spectrum at RT (bottom, red), followed by spectra recorded after heading the sample to 55° C at 7 min, 30s, 25 min, 40 min, 57 min, 70 min, and 85 min.

## Crystallographic data

Table S2- 2: Crystallographic data for **1**, **3**, **4**, **$[L^{NH2}CuCl]_2$** and **$[L^{NO2}CuCl]_2$**.

| | **1** | **3** | **4**[a] | **$[L^{NH2}CuCl]_2$** | **$[L^{NO2}CuCl]_2$** |
|---|---|---|---|---|---|
| CCDC number | 1962820 | 1962821 | 1962822 | 1962858 | 1962859 |
| Formula | $C_{18}H_{18}ClCuN_4O_3S\cdot C_2H_3N$ | $C_{18}H_{16}Cl_{1.119}CuN_{3.881}O_{2.881}S$ | $C_{100}H_{57}B_2Cu_2F_{48}N_8O_5S_2$ | $C_{19}H_{19}Cl_4CuN_4O_2S$ | $C_{18}H_{16}ClCuN_4O_4S$ |
| Formula Weight | 510.47 | 467.40 | 2575.35 | 572.78 | 483.40 |
| *T*/K | 150(2) | 150(2) | 100(2) | 150(2) | 150(2) |
| Wavelength/Å | 1.54178 (Cu *K*□□ | 1.54178 (Cu *K*□□ | 0.71073 (Mo *K*□□ | 1.54178 (Cu *K*□□ | 1.54178 (Cu *K*□□ |
| Size/mm$^3$ | 0.51×0.29×0.27 | 0.153×0.122×0.065 | 0.25×0.20×0.13 | 0.275×0.146×0.038 | 0.651×0.134×0.052 |
| Crystal System | Monoclinic | Triclinic | Triclinic | Monoclinic | Monoclinic |
| Space Group | $P2_1/n$ | $P$-1 | $P$-1 | $P2_1/c$ | $P2_1/c$ |
| *a*/Å | 10.8103(2) | 7.71840(10) | 15.243(2) | 7.9754(3) | 13.7726(5) |
| *b*/Å | 13.6690(2) | 9.4477(2) | 18.200(2) | 9.6467(3) | 8.9756(3) |
| *c*/Å | 15.5083(3) | 13.9101(3) | 20.812(2) | 29.6489(9) | 15.8948(6) |
| $\alpha$/° | 90 | 71.6860(10) | 94.964(7) | 90 | 90 |
| $\beta$/° | 110.304(1) | 79.1810(10) | 105.186(7) | 93.529(2) | 108.792(2) |
| $\gamma$/° | 90 | 78.9680(10) | 106.059(7) | 90 | 90 |
| V/Å$^3$ | 2149.21(7) | 936.27(3) | 5275.7(11) | 2276.75(13) | 1860.13(12) |
| *Z* | 4 | 2 | 2 | 4 | 4 |
| $D_{calc.}$/ g cm$^{-3}$ | 1.578 | 1.658 | 1.621 | 1.671 | 1.726 |
| $\mu$/mm$^{-1}$ | 3.77 | 4.254 | 0.584 | 6.750 | 4.347 |
| $\Theta_{min}$/° | 4.4 | 3.38 | 1.029 | 2.986 | 3.390 |
| $\Theta_{max}$/° | 68.3 | 66.72 | 22.603 | 68.321 | 68.360 |
| Measured Refl's. | 32095 | 5757 | 35495 | 4164 | 27236 |
| Independent reflections | 3883 | 5757 | 13745 | 4164 | 3407 |
| Reflexions with I > 2(I) | 3546 | 5332 | 8599 | 3322 | 2984 |
| $R_{int}$ | 0.055 | 0.057 | 0.0552 | 0.109 | 0.087 |
| Parameters | 286 | 258 | 1777 | 280 | 262 |
| Restraints | 0 | 0 | 3704 | 0 | 0 |
| Largest Peak | 0.24 | 0.79 | 1.836 | 0.52 | 0.29 |
| Deepest Hole | -0.50 | -0.39 | -0.929 | -0.66 | -0.49 |
| Goodness of fit | 1.034 | 1.088 | 1.024 | 1.064 | 1.059 |
| $wR_2$ (all data) | 0.828 | 0.1354 | 0.2714 | 0.1525 | 0.0867 |
| $wR_2$ | 0.806 | 0.1328 | 0.2209 | 0.1441 | 0.0834 |
| $R_1$ (all data) | 0.0349 | 0.0509 | 0.1401 | 0.0830 | 0.0382 |
| $R_1$ | 0.0319 | 0.0475 | 0.0884 | 0.0655 | 0.0327 |

[a] Details for the solution of **4**: The material crystallizes with considerable disorder in the two BArF anions, as well as with solvent in the lattice. The solvent could not be modeled satisfactorily, so the PLATON/SQUEEZE program was employed to generate a 'solvent-free' data set. Disorder in the BArF anions was modeled using appropriate restraints on bond lengths. Rigid groups were employed to model six-membered rings in the BArF anions. All non-hydrogen atoms were refined anisotropically. Most hydrogen atom positions were calculated geometrically and refined using the riding model, but some hydrogen atom H7 was located in a difference map and refined freely.

## XAS data

All Cu K-edge XAS spectra were recorded at beamline 7-3 of the Stanford Synchrotron Radiation Lightsource (SSRL) using a 32 element Ge detector. All spectra were recorded at 4K using a liquid helium cryostat and all samples were prepared in an argon glovebox. All Data were processed using Athena, from the Demeter software package.[109] The Cu K-edge XAS of **1** was measured using the microcrystalline powder formed by precipitation upon reaction of $L^{NHOH}$ with $Cu^{I}Cl$ in ACN. This reaction was performed on-site in the argon glovebox and the precipitate was sealed into a sample holder using Tygon® tape. The Cu K-edge XAS of **2**, which tends to dimerize upon concentration, was measured in a frozen 15 mM solution in DCM. To produce this solution, 3 eq. of DIAD, dissolved in DCM, was added dropwise to a 15 mM solution of **1** in DCM in an argon glovebox. This solution was injected into an acrylic sample cell tightly sealed with Tygon® tape and immediately frozen in liquid nitrogen before transfer to the experimental apparatus and further cooling to 4K by liquid helium. An unoxidized sample of a 15 mM solution of **1** in DCM was prepared similarly and its Cu K-edge XAS was also measured. Samples of the solid products of mechanochemically-induced disproportionation of **1** were measure prepared similarly to **1**. The solid mixtures produced by grinding **1** in a ball miller under three different conditions were measured. These conditions included grinding **1** under an inert nitrogen atmosphere, grinding **1** under air, and grinding an equimolar mixture of $\mathbf{L^{NHOH}}$ and $Cu^{I}Cl$ under nitrogen. the Cu K-edge XAS of **1**, measured in the solid state, had a rising edge at 8982.4 eV, and that of **2** had a rising edge of 8985.0 eV. This edge shift of 2.6 eV is consistent with a change in oxidation state from $Cu^{I}$ to $Cu^{II}$. Interestingly, the frozen solution of **1** in DCM exhibited damaging as the XAS was measured. Over the course of 30 scans, the clear $Cu^{I}$ spectrum of **1** converted to a $Cu^{II}$ spectrum with features identical to those of **2** produced by chemical oxidation. This suggests that oxidation of **1** to **2** can be photochemically initiated, at least using x-rays in the energy range of the Cu K-edge. This damaging was not, however, observed with successive scans of the solid precipitate of **1**, therefore the photochemically-induced oxidation must be environment-dependent, and possibly solvent-dependent.

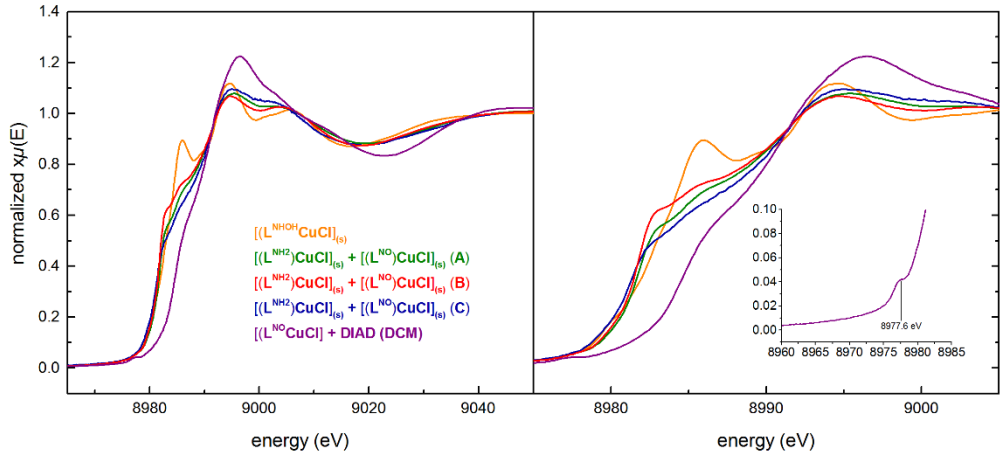


Figure S2- 15: Normalized Cu K-edge XAS (left) and zoom into XANES region (right) for solid **[(L$^{NHOH}$)CuCl]** (**1**), alongside **[(L$^{NH2}$)CuCl] + [(L$^{NO}$)CuCl]**, the products of mechanochemically-induced disproportionation of **[(L$^{NHOH}$)CuCl]**, (A) under a $N_2$ environment, (B) under an $O_2$ environment, and (**C**) **[(L$^{NH2}$)CuCl] + [(L$^{NHOH}$)CuCl]** formed by mechanochemical grinding of equal portions of **L$^{NHOH}$** and **CuCl** in the solid state, and a frozen 15 mM solution of **[(L$^{NO}$)CuCl]** in DCM, formed by reaction with 3 eq. (excess) **DIAD** (inset shows pre-edge region with peak at 8977.6 eV).

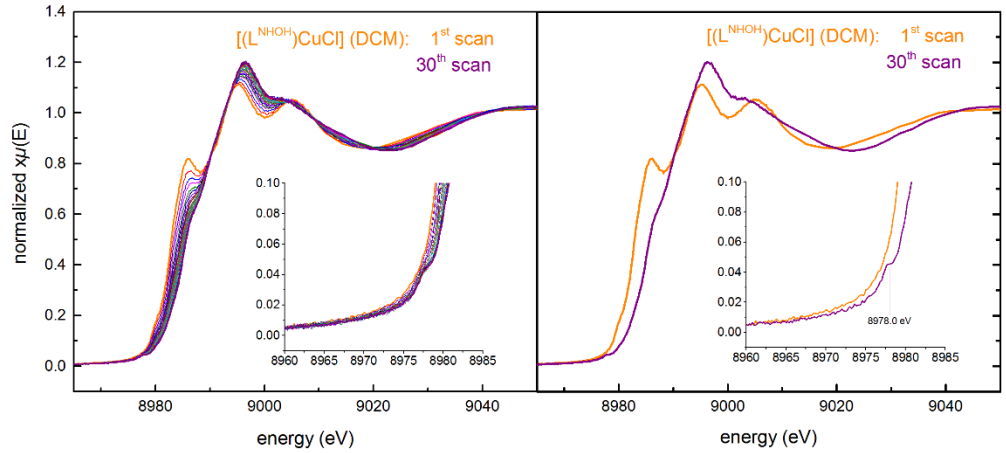


Figure S2- 16: Normalized Cu K-edge XAS (left) of 30 scans of a frozen 15 mM solution of **[(L$^{NHOH}$)CuCl]** in DCM and (right) the 1$^{st}$ and 30$^{th}$ of those scans, with inset showing copper(II) pre-edge feature at 8978 eV. See comparison of Cu K-edge XAS of **[(L$^{NO}$)CuCl]** produced by reaction of **[(L$^{NHOH}$)CuCl]** with **DIAD** to the photo oxidized 30$^{th}$ scan in Figure S2- 17 (right)).

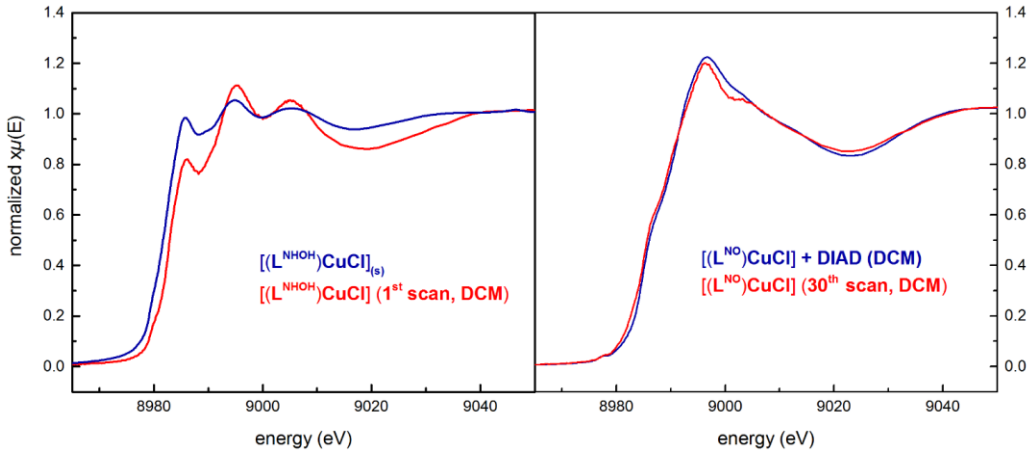


Figure S2- 17: A comparison of the normalized 1st scan of the Cu K-edge XAS of a frozen 15 mM solution of **[(L$^{NHOH}$)CuCl]** in DCM (before photooxidation, red) to the normalized Cu K-Edge XAS of solid **[(L$^{NHOH}$)CuCl]** (blue) (left) and a comparison of the normalized 30th scan (after photooxidation, red) to the normalized Cu K-Edge XAS of a frozen 15 mM solution of **[(L$^{NO}$)CuCl]** in DCM, formed by reaction with 3 eq. **DIAD** (blue) (right).

## EXAFS details

The EXAFS data for the Cu K-edge XAS of a frozen 10 mM solution of [(L$^{NHOH}$)CuCl], oxidized *in situ* with 3 equivalents of DIAD in DCM, **[(L$^{NO}$)CuCl]$_{(DCM)}$**, were fit using Artemis, from the Demeter software package[109]. All fitting was performed using a *k* range of 2.0-12 Å$^{-1}$ and an R range of 1.1-2.1 Å. $S_0^2$ was set to 0.9, and a single $\Delta E_0$ value was guessed for all paths in each fit. In case where restraining $\sigma^2$ was necessary, a range of 1.00x10$^{-3}$-6.00x10$^{-3}$ was used. Paths were predicted using the Feff program[110], based on input from a DFT-optimized geometry.

The goal of this fitting was to investigate the consistency of the experimental EXAFS of **[(L$^{NO}$)CuCl]$_{(DCM)}$**, with an optimized DFT model. Since this complex cannot be crystalized as a monomer due to dimerization at high concentrations, these data were used to confirm the coordination of $N_{NO}$ and the predicted contraction of the other bond distances on oxidation. In the tables on the following pages, restrained parameters are shown in blue, unphysical parameters are shown in red, N refers to "degeneracy", $N_{in}$ refers to the inner nitrogen shell, including the two $N_{Py}$ and $N_{NO}$, and $N_{out}$ refers to the outer nitrogen shell, including $N_{backbone}$, and in some cases $O_{NO}$.

Fit 7 restrains $\sigma^2$ for Cu-Cl and Cu-O,$N_{out}$ from fit 6, leading to a reasonably good fit (R-factor of 0.009285 vs. 0.013069 of fit 5 and 0.009511 of fit 1), and good agreement with the theoretically-predicted bond distances (see Table S2- 3). With *k*-space from 2-10 Å$^{-1}$, the expected resolution of $\pi/2\Delta k$ is 0.157 Å so it is reasonable based on these data that these atoms should be distinguishable. Besides, O and $N_{out}$, all

other shells are separated by more than 0.157 Å except Cl and $N_{out}$, which are separated by 0.14 Å in fit 7.This explains the necessity of restraining their $\sigma^2$ values. Due to the large difference in effective scattering amplitude and phase shift between Cl and N, however, these two shells must be separated to obtain a good fit. It should also be pointed out that the radial distances of O and $N_{out}$, which are separated by 0.26 Å, are only 41.3% correlated in fit 7. Taken together, these data suggest that the structure of **$[(L^{NO})CuCl]_{(DCM)}$** in solution at 10 mM is very similar to that predicted by DFT with conductor-like polarizable continuum (CPCM) solvent corrections using ε = 9.08 (see Table S2- 3 and Figure S2- 18).

Table S2- 3: Fit 7 ($N_{out}$ = 1, O = 1; Cl, $N_B$ $\sigma^2$-restrained).

| R-factor | $\Delta E_0$ (eV) | Path | N | $\sigma^2$ (x$10^{-3}$ Å$^2$) | R (Å) |
|---|---|---|---|---|---|
| 0.009285 | 8989.51 | Cu-$N_{in}$ | 3 | 3.01 | 1.98 |
| | | Cu-Cl | 1 | 6.00 | 2.28 |
| | | Cu-$N_{out}$ | 1 | 6.00 | 2.42 |
| | | Cu-O | 1 | 5.48 | 2.61 |
| | | Cu-C | 4 | 1.95 | 2.91 |

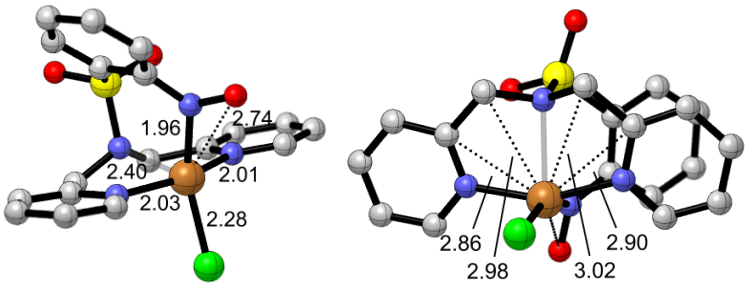


Figure S2- 18: DFT model of $^3$**2** optimized at the CAM-B3LYP/Def2-TZVP level of theory with zero-order regular approximation (ZORA) relativistic corrections and CPCM (ε = 9.08) solvation corrections (*vide infra*), showing bond distances about the inner sphere of coordination.

Table S2- 4: A comparison of the DFT model of $^3$**2** to EXAFS fit 7.

| Path | EXAFS (Fit 7, Å) | DFT model of $^3$**2** (Å) |
|---|---|---|
| Cu-$N_{in}$ | 1.98 | 2.01, 2.03, 1.96 ($\bar{x}$ = 2.00) |
| Cu-Cl | 2.28 | 2.28 |
| Cu-$N_{out}$ | 2.42 | 2.40 |
| Cu-O | 2.61 | 2.74 |
| Cu-C | 2.91 | 2.88, 3.01, 2.98, 2.87 ($\bar{x}$ = 2.94) |

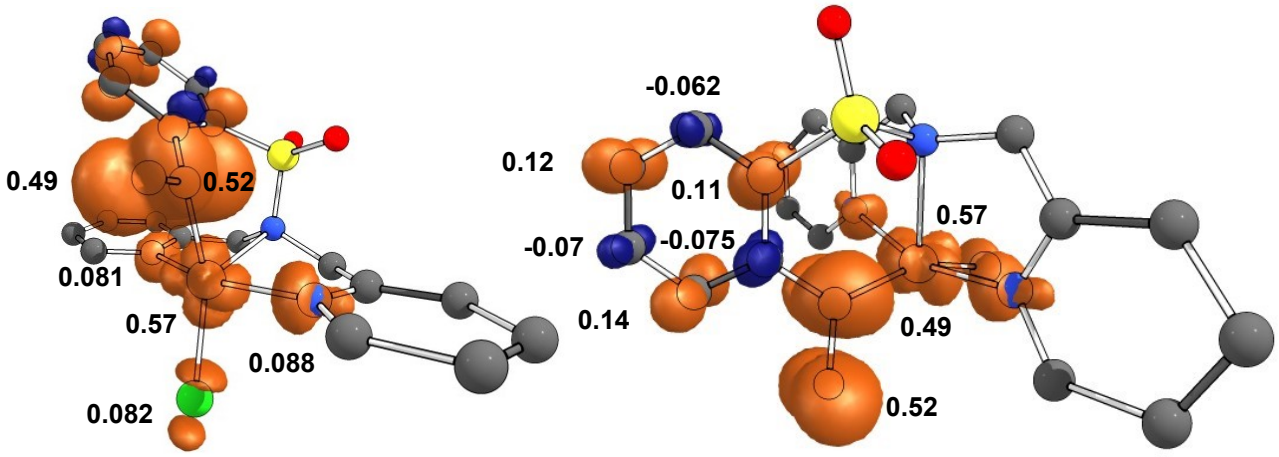


Figure S2- 19: Spin density plot of optimized $^{3}$**2** geometry showing corresponding Mulliken spin populations.

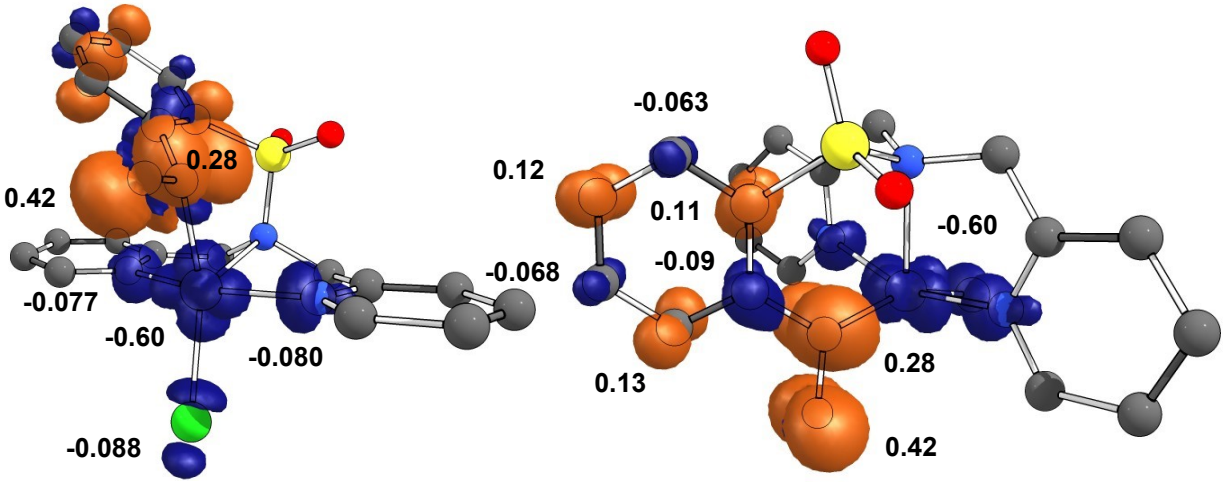


Figure S2- 20: Spin density plot of optimized $^{1}\mathbf{2}_{BS}$ geometry showing corresponding Mulliken spin populations.

## Spectroscopic calculations

All spectroscopic calculations were performed at the same level of theory decided upon in the method validation phase, but the finer Grid7 integration grade was selected both for initial and final integration in order to minimize numerical error. Valence (UV-Vis) TD-DFT calculations were performed using 50 roots, while core (Cu K-edge XAS) TD-DFT calculations were performed using 60 roots. The resulting calculated spectra were plotted using the orca_mapspc utility with a peak width at half-maximum of 1.55 eV for the TD-DFT-calculated 1s excitations, corresponding to the known natural line width for the Cu K-edge[111], and a broadening of 4000 cm-1 for the TD-DFT calculated valence excitations, corresponding to the value obtained from the Gaussian fit of the experimental UV-Vis of 2 shown in Figure S2- 12.

The resulting calculated Cu K-edge XAS spectra are shown in Figure S2- 21-Figure S2- 23, alongside the difference densities associated with the states of interest and the corresponding canonical acceptor orbitals for the excited state configurations with the largest CI expansion coefficients. These spectra show qualitative agreement with the experimental Cu K-edge XAS of **1** and **2**, however the calculations predict no feature that should distinguish $^{1}\mathbf{2}_{\mathbf{AFC}}$ and $^{3}\mathbf{2}$ by Cu K-edge XAS. the calculated spectra are shifted to slightly higher energies than those seen in the experimental spectra, as is often observed with TD-DFT-calculated Cu K-edge XAS. The calculated spectrum of **1** is shifted by 3.6 eV from the experimental value of 8982.4 eV to 8985 eV, while the calculated spectra of $^{1}\mathbf{2}_{\mathbf{AFC}}$ and $^{3}\mathbf{2}$ are shifted by 4.8 eV from the experimental value for **2** of 8985.0 eV to 8989.8 eV. In the TD-DFT calculated XAS, the edge shift from **1** to **2** is 4.8 eV, 2.2 eV greater than the experimental edge shift of 2.6 eV. Although the calculated XAS show qualitative agreement with the experimental XAS, reproducing the shape of the spectra and the overall presence of the edge shift from **1** to **2**, these significant quantitative discrepancies highlight the limitations of single reference TD-DFT calculations for calculation of species such as **2**, which is of a class of compounds known to have particularly strong multireference character[112],[113]. Moreover, this discrepancy suggests that the DFT method used herein overestimates the oxidation of the $Cu^{II}$ in presence of a κ-*N*-$(ArNO)^{\bullet-}$, therefore, despite good agreement with the geometry, experimentally verified by the EXAFS fit shown in section 14, the level of theory used in this study is likely failing to properly represent both the ground state and excited state electronic structures of **2**. These limitations in mind, the TD-DFT spectra and the corresponding density difference plots allow us to tentatively make the assignment of the pre-edge feature seen in the experimental Cu K-edge spectrum of **2** at 8977.6 eV as a 3d←1s transition into the d-hole produced by oxidation of the Cu center to $Cu^{II}$.

Figure S2- 24 shows a comparison of the TD-DFT-calculated UV-Vis spectrum of $^{3}\mathbf{2}$ and **1** to the experimental UV-Vis spectra of **2** and **1** shown in Figure S2- 10. Once again, there is qualitative agreement with the experimental spectra, with states 6 and 7 being assigned to the shoulder and peak seen experimentally at 14900 $cm^{-1}$ and 19700 $cm^{-1}$. Based on the difference density plots, shown in Figure S2- 25, we tentatively assign the shoulder as an inter-ligand charge transfer (ILCT) between the singly occupied $\pi^*$ orbital of the $(ArNO)^{\bullet-}$ moiety and the aromatic $\pi^*$ system, and the peak as a ligand-to-metal charge transfer (LMCT) from the singly occupied $\pi^*$ orbital of the $(ArNO)^{\bullet-}$ moiety to the $Cu^{II}$ d-hole. The agreement between the TD-DFT and the experimental data are reasonable but cannot properly describe the electronic complexity of the multireference ground state that would be most appropriate for such systems.

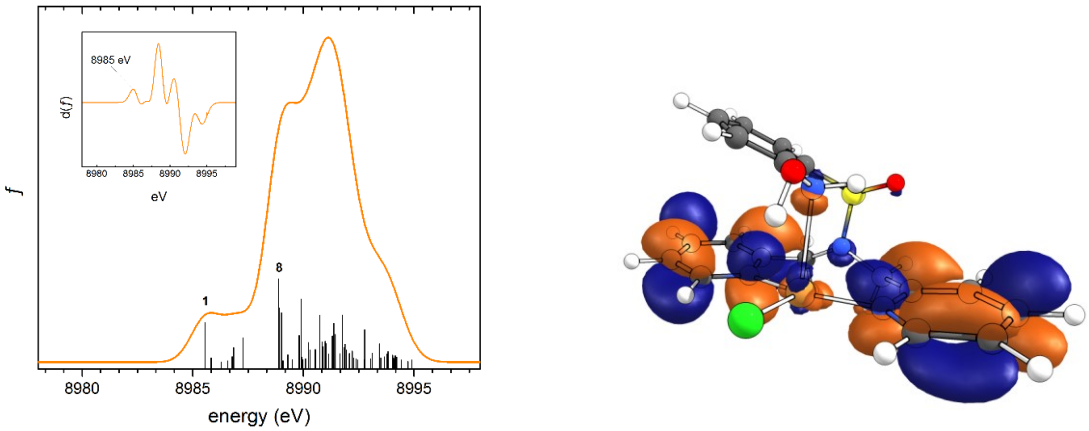


Figure S2- 21: TD-DFT-calculated pre-edge and rising edge of XAS of **1**. Calculation was performed with CPCM ε = 2.5 using geometry from optimization of **1** with CPCM ε = 2.5 (left) and the canonical acceptor orbital of the excited state configuration of state 1 with the largest CI expansion coefficient, plotted with a contour value of 0.03 (right).

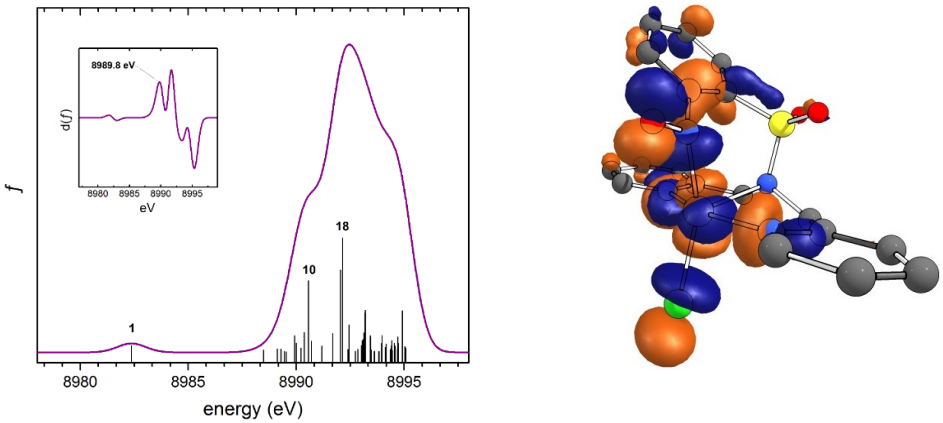


Figure S2- 22: TD-DFT-calculated pre-edge and rising edge of XAS of $^{3}$**2**. Calculation was performed with CPCM ε = 2.5 using geometry from optimization of $^{3}$**2** with CPCM ε = 9.08 (DCM) (left) and the canonical acceptor orbital of the excited state configuration of state 1 with the largest CI expansion coefficient, plotted with a contour value of 0.03 (right).

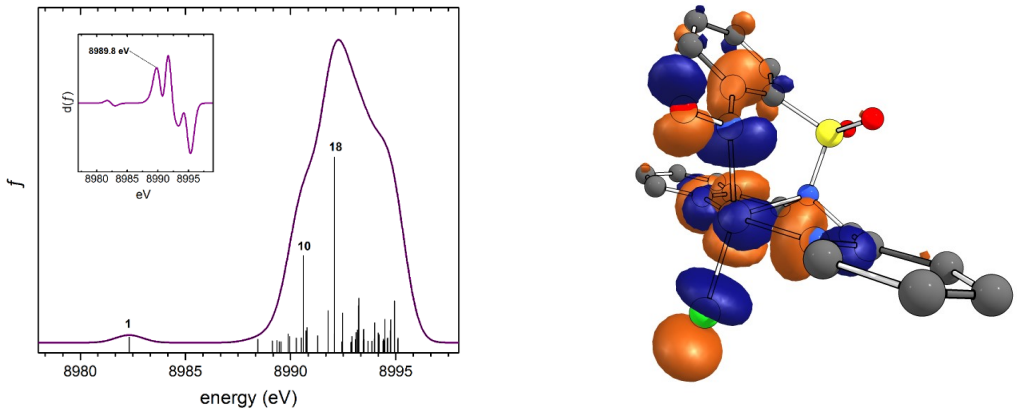


Figure S2- 23: TD-DFT-calculated pre-edge and rising edge of XAS of $^{1}\mathbf{2}_{\mathbf{AFC}}$. Calculation was performed with CPCM ε= 2.5 using geometry from optimization of $^{1}\mathbf{2}_{\mathbf{AFC}}$ with CPCM ε = 9.08 (DCM) (left) and the canonical acceptor orbital of the excited state configuration of state 1 with the largest CI expansion coefficient, plotted with a contour value of 0.03 (right).

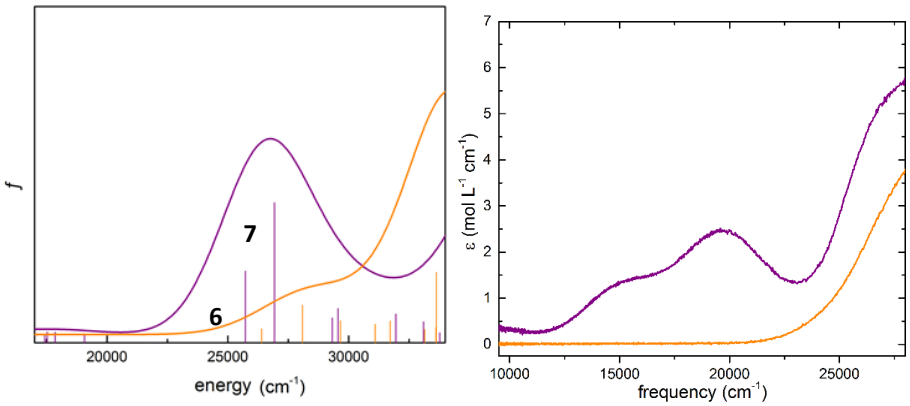


Figure S2- 24: A comparison of the TD-DFT-calculated UV-Vis spectrum of $^{3}\mathbf{2}$ and **1** using both geometries and excited states calculated with CPCM ε = 9.08 (DCM) (left) to the experimental UV-Vis spectra of **2** and **1** (shown earlier in Figure S2- 10). See also the Gaussian deconvolution of the spectrum of **2** shown in Figure S2- 12.

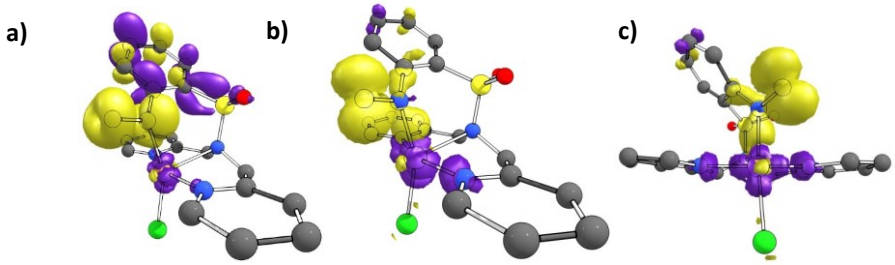


Figure S2- 25: Difference density plots of (a) state 6 and (b) state 7 (c), plotted with contour values of 0.003, showing a different view of the same plot) of the TD-DFT-calculated UV-Vis spectrum of $^{3}\mathbf{2}$ State 6 is assigned as an ILCT and state 7 is assigned as an LMCT.